Type-II Zeeman Slower and Design and Construction of a Cryogenic Buffer Gas Beam Source

---

Von der Fakultät für Mathematik und Physik
der Gottfried Wilhelm Leibniz Universität Hannover

zur Erlangung des Grades
Doktor der Naturwissenschaften
- Dr. rer. nat-
genehmigte Dissertation von
M.Sc. Maurice Petzold

2018

Referent: Prof. Dr. Silke Ospelkaus

Korreferent: apl. Prof. Dr. Carsten Klempt

Korreferent: Prof. Dr. Boerge Hemmerling

Tag der Promotion: 21.11.2018

Abstract

Ultracold molecules promise to leverage the insight into a diverse research field ranging from controlled ultracold chemistry over precision measurements of parity violating effects to strongly correlated dipolar quantum many body systems. However, the additional degrees of freedom associated with vibration and rotation of molecules preventing the direct transfer of atomic cooling techniques. Still, direct laser cooling of molecules has undergone rapid development in recent years and bridged the gap between cryogenic temperatures ($T \approx 1\,\mathrm{K}$) and the deep ultracold regime ($T < 1\,\mathrm{mK}$). The limiting factor in recent experiments is the low number of molecules loaded into the initial magneto-optical traps, inhibiting the application of evaporative cooling as the natural subsequent step. Thus, high flux sources of cold and slow molecules are highly required.

In this thesis a radiative beam slowing method for laser-coolable molecules working on a type-II level structure has been developed inspired by atomic Zeeman slowing. The new type-II Zeeman slowing scheme relies on the decoupling of angular momenta in the Paschen-Back regime and the resulting simplified level structure. The scheme allows the deceleration force to be tailored velocity-selective with the ability to address a large class of velocities as a function of position in an inhomogeneous magnetic field. Three-dimensional Monte Carlo simulations show continuous deceleration and compression of the one dimensional velocity distribution down to velocities which can be captured by molecular magneto-optical traps.

The feasibility of the scheme has been shown in an atomic test experiment implementing type-II Zeeman slowing on the D_1-line of ^{39}K. A flux of $\Phi_{\mathrm{II}} = 3.3 \cdot 10^9\,\mathrm{s^{-1}cm^{-2}}$ under $35\,\mathrm{m\,s^{-1}}$ has been achieved. The longitudinal velocity distribution is compressed into a narrow velocity peak with a longitudinal temperature of $T_{\parallel} = 270\,\mathrm{mK}$. It is thereby the first experimentally shown technique which is continuous and dissipative in molecule-like level structures.

The experimental implementation of white-light slowing in the same setup results in a flux of $\Phi_{\mathrm{w}} = 1.5 \cdot 10^8\,\mathrm{s^{-1}cm^{-2}}$, a factor of 20 lower than the attained flux of the type-II Zeeman slower. The traditional type-I Zeeman slower, whose implementation is inhibited in type-II level structures, has been realized as a benchmark. A flux of $\Phi_{\mathrm{I}} = 5.5 \cdot 10^9\,\mathrm{s^{-1}cm^{-2}}$ has been achieved, which is a factor of only 1.66 higher than the type-II scheme. The differences in the slowing methods have been identified by Monte Carlo simulations reproducing the experimental observations and are explained as a result of the efficiency with which the radiation pressure force is applied.

As a first step towards the implementation of type-II Zeeman slowing with molecules a laser ablation loaded cryogenic buffer gas beam source has been designed and set up. The buffer gas flow field has been carefully simulated and the appearance and circumvention of vortices have been investigated. A first characterization with pulses of ^{39}K has been conducted and a good agreement to a hydrodynamic description by the sudden freeze model complemented with a velocity slip has been found. An explanation for multi-peak structures in the molecular pulses is proposed as a hydrodynamic effect of the high pressure and high temperature expansion of the ablated material into the cold buffer gas and its impact on the overall flow field.

Keywords: laser cooling, ultracold molecules, molecular beam slowing, molecular quantum gases

Zusammenfassung

Ultrakalte Moleküle versprechen neue Einsichten in diversen Forschungsfeldern die von kontrollierter ultrakalter Chemie über Präzisionsmessungen paritätsverletzender Effekte bis hin zu stark korrelierten dipolaren Quantenvielteilchensystemen reichen. Jedoch verbieten die zusätzlichen Freiheitsgrade der Rotation und Vibration von Molekülen, den direkten Transfer atomarer Kühltechniken. Das direkte Laserkühlen von Molekülen hat dennoch eine rasante Entwicklung in den letzten Jahren erlebt und schloss die Lücke zwischen kryogenen Temperaturen und dem ultrakalten Regime. Der limitierende Faktor in derzeitigen Experimenten ist die niedrige Anzahl an Molekülen die in die initiale magneto-optische Falle geladen werden. Daher gibt es eine hohe Nachfrage an Quellen von kalten und langsamen Molekülen mit hohem Fluss.

In der vorliegenden Arbeit wird über eine neue Methode zum Abbremsen laser kühlbarer Moleküle auf einem Typ-II Übergang durch die Spontankraft berichtet, welche vom atomaren Zeeman-Abbremser (Zeeman-Slower) inspiriert ist. Das neue Typ-II Zeeman-Slower Schema beruht auf der Entkopplung der atomaren Drehimpulse im Paschen-Back Regime und der daraus resultierenden vereinfachten Energieniveaustruktur. Das Schema erlaubt die Bremskraft geschwindigkeitsselektiv anzuwenden und eine breite Verteilung an Geschwindigkeitsklassen als Funktion des Ortes in einem inhomogenen Magnetfeld anzusprechen. Dreidimensionale Monte Carlo Simulationen zeigen eine Kompression der eindimensionalen Geschwindigkeitsverteilung und ein kontinuierliches Abbremsen zu Geschwindigkeiten die ein Fangen in molekularen magneto-optischen Fallen erlauben.

Die Durchführbarkeit wurde an einem atomaren Testexperiment gezeigt, welches Typ-II Zeeman-Slowing auf der D_1-Linie von ^{39}K zeigt und einen Fluss von $\Phi_{\mathrm{II}} = 3.3 \cdot 10^9\,\mathrm{s}^{-1}\mathrm{cm}^{-2}$ unter $35\,\mathrm{m\,s}^{-1}$ erreicht. Die longitudinale Geschwindigkeitsverteilung wird dabei in ein schmales Geschwindigkeitsfenster mit einer longitudinalen Temperatur von $T_{\parallel} = 270\,\mathrm{mK}$ kompressiert. Damit ist es die erste experimentell realisierte Technik die kontinuierliches und dissipatives Abbremsen in molekülähnlichen Energieniveaustrukturen erlaubt. Die experimentelle Realisierung von Weisslicht abbremsen im gleichen experimentellen Aufbau resultiert in einem Fluss von $\Phi_{\mathrm{w}} = 1.5 \cdot 10^8\,\mathrm{s}^{-1}\mathrm{cm}^{-2}$ dies ist einen Faktor 20 kleiner als der erreichte Fluss des Typ-II Zeeman-Slowers. Der traditionelle Typ-I Zeeman-Slower, dessen Implementierung in einer Typ-II Energieniveaustruktur unmöglich ist wurde ebenfalls als Vergleichspunkt realisiert. Ein Fluss von $\Phi_{\mathrm{I}} = 5.5 \cdot 10^9\,\mathrm{s}^{-1}\mathrm{cm}^{-2}$ wurde erreicht, was nur einen Faktor 1.66 höher liegt als in dem Typ-II Schema. Die Unterschiede der verschiedenen Bremsmethoden werden mit Hilfe von Monte Carlo Simulationen , welche die experimentellen Beobachtungen reproduzieren, identifiziert und als Resultat der unterschiedlichen Effizienz mit der die Spontankraft angewendet wird beschrieben.

Als erster Schritt hin zu einer Implementierung des Typ-II Zeeman Slowers mit Molekülen wurde eine laserablations geladene kryogene Puffergaszelle konstruiert und aufgebaut. Das Flussfeld des Puffergases wurde simuliert und die Wirbelbildung und ihre Verhinderung im Flussfeld untersucht. Eine erste Charakterisierung mit atomaren Pulsen aus ^{39}K wurde durchgeführt und eine gute Übereinstimmung mit dem hydrodynamischen “Sudden-Freeze” Modell, erweitert mit einer Geschwindigkeitsverschiebung, wurde gefunden. Eine Erklärung von “multi-peak” Strukturen in den atomaren Pulsen wird vorgeschlagen, die diese als hydrodynamischen Effekt der Expansion des abladierten Materials und dem daraus folgenden Einfluss auf das Gesamtflussfeld der Puffergaszelle beschreibt.

Schlagwörter: Laserkühlen, ultrakalte Moleküle, Molekularstrahlabbremsen, molekulare Quantengase

Publications

- M. Petzold, P. Kaebert, P. Gersema, M. Siercke and S. Ospelkaus, *A Zeeman Slower for diatomic molecules*, New J. Phys. **20** 042001 (2018)
- M. Petzold, P. Kaebert, P. Gersema, T. Poll, N. Reinhardt, M. Siercke and S. Ospelkaus, *Type-II Zeeman slowing: Characterization and comparison to conventional radiative beam slowing schemes*, Phys. Rev. A **98** 063408 (2018)

Contents

1

Introduction

Within this thesis, I present work towards the preparation of laser cooled ensembles of ultracold polar $^{40}Ca^{19}F$ molecules. A new radiative beam slowing method for molecules has been developed and results of a test experiment working with atomic ^{39}K are presented. Furthermore, I present the design and construction of a cryogenic buffer gas beam apparatus and revisit the theoretical description of the physical processes at play in these beam sources complemented with numerical simulations and first measurements.

In the following I will give a brief overview on the broad range of applications for ultracold molecules (see section 1.1) and the cooling methods for their production (see section 1.2).

1.1. Applications for Ultracold Molecules

Temperature is an essential parameter in atomic physics and the successful production of ultracold atoms had an immense scientific impact. The workhorse to reach the ultracold regime with atoms is laser cooling, from which a whole research field of ultracold matter emerged. The applications of ultracold atoms nowadays range from metrology over simulation of condensed matter systems to precision measurements and quantum information processes.

In recent years there has been growing interest in the production of ultracold molecules which are considered to open a similarly large research field with a broad range of scientific applications [1].

In comparison to atoms, molecules have more degrees of freedom due to their rovibrational structure and polar molecules exhibit a permanent electric dipole moment. Here, the interparticle interaction can be several times larger than for ultracold atoms due to the large value of the electric dipole moment. Furthermore the associated dipole-dipole interaction is anisotropic and tunable by static external electric fields. Dependent on the orientation of the molecular electric dipole moments and the arrangement of the molecules to each other the interaction can be either repulsive or attractive. There are several exotic states of matter proposed for such quantum many body systems [2] making it a rich research field.

Another broad research field, which can be studied with ultracold molecules, is the physics of collisions at low energy [1, 3] and ultracold chemistry [3, 4, 5], where the reactants can be merged with low collision energies in specific quantum states and maybe even with a specific orientation to each other. Here reaction pathways might be mapped out giving insight into transition states during a chemical reaction and reaction barriers therein. Ultimately the complete knowledge of all quantum numbers of the reactants as well as for the products would constitute a "complete chemical experiment" [3].

Furthermore ultracold molecules are a promising candidate for quantum computing [6].

The quantized orientation of the permanent electric dipole on an external electric field could be used as a qubit, whereas the coupling is mediated through the long range dipole-dipole interaction. A large number of qubits could be produced relatively easily in an optical trap. Here ultracold temperatures would enable the usage of shallow traps, where decoherence times can be long [6]. The states are addressible with microwave radiation, another major advantage in the usage of ultracold molecules.

The internal structure of some molecules gives the possibility for tests of fundamental symmetries. For example the electric field felt by an electron inside a molecule can be magnitudes larger ($10^{10}\,\mathrm{V\,cm^{-1}}$) than what is possible to implement in a laboratory ($10^4 - 10^5\,\mathrm{V\,cm^{-1}}$). Additionally the electron stays inside the molecule while feeling the large inner electric field and is not accelerated away from the experimental observation region like it would be the case of a free electron. This gives experimentalists the opportunity to search for an electric dipole moment of the electron [7, 8, 9] which is predicted by many extensions of the standard model in physics to explain the matter antimatter imbalance in our universe. Up to now no dipole moment has been measured, but the precision reached by the experiments nowadays already cuts deep into the predictions of the theoretical extensions in such a way that many of these seem unlikely to be true. Other parity violating effects can also be enhanced for diatomic molecules [10, 11] and recently there have been first measurements towards nuclear spin dependent parity violating effects in $^{137}\mathrm{Ba}^{19}\mathrm{F}$ [12, 13].

Due to the broad range of applications for ultracold molecules [1] the figure of merit might differ from experiment to experiment. Still a high phase space density and therefore high molecule numbers at low temperatures are generally beneficial for these experiments.

1.2. Production of Ultracold Molecules

To put this work into perspective, we give a short summary of the different approaches towards the preparation of ultracold molecular ensembles. Details about laser cooling of molecules will be given in greater detail in chapter 2.

Assembly from Ultracold Atoms

High phase space density ensembles of ultracold molecules have first been produced through the association of ultracold atoms by coherent techniques, where the phase space density is preserved. One possibility is to use magnetic Feshbach resonances [14, 15], to prepare loosely bound molecules and subsequently transfer them into their rovibrational ground state through a coherent pathway.

The approach is limited to molecules whose constituents are laser coolable atoms. This restriction however is not severe if the goal of the experiment is the investigation of quantum states of matter with long range dipole dipole interactions. Still, the molecules produced are not suitable for the search of an electron electric dipole moment and the chemical diversity is limited to molecules composed out of laser coolable atomic species. The direct detection of the molecules is experimentally challenging and typically they need to be dissociated for a detection of the atomic constituents.

Buffer Gas Cooling and Supersonic Expansion

A very general method to cool molecules is buffer gas cooling. Here, the molecules of interest are injected in an inert gas like He or Ne which is cooled to cryogenic temperatures. With this method molecules can be sympathetically cooled to temperatures limited by the vapor pressure of ^{3}He to $T \approx 300\,\mathrm{mK}$. But the isolation of the molecules from the buffer gas for later experiments can be challenging and residual collisions with remaining buffer gas atoms limit the lifetimes and temperatures achievable in subsequent experimental stages [16].

Cryogenic buffer gas apparatuses also serve as a source of cold and slow molecular beams [17] by ejecting the molecules of interest through a hole in the cooling cell. These pre-cooled molecular beams can be an ideal starting point for other cooling methods. An implementation of a buffer gas cell beam apparatus was part of this thesis as well.

Cold molecular beams can also be produced by the expansion of a room temperature gas at high pressure into a vacuum chamber [18]. Here, thermal energy is converted in kinetic energy in a supersonic isentropic expansion. The temperatures reached can be in the mK-regime but the molecules move at longitudinal forward velocities of $v_{\parallel} = 200 - 600\,\mathrm{m\,s^{-1}}$ in the laboratory frame.

Manipulation through External Fields

If the molecule of interest possess an electric or magnetic dipole moment, the translational motion can be manipulated by external electric or magnetic fields. In 2003 the first Stark decelerator was implemented [19], where dipolar molecules can be decelerated by time varying electric fields from a supersonic expansion to a standstill in the laboratory frame. Here the molecules climb up a potential well produced by high voltage electric fields and thereby loose kinetic energy, just when they reach the top of the potential well the high voltage is shut off and a subsequent electrode provides the next well. The molecules are thereby slowed down in a Sisyphus like manner. Later the same principle was implemented using magnetic fields with the Zeeman decelerator [20]. Due to the time varying fields these slowing methods are not continuous but there are proposals to use static fields and pump the molecules between low field seeking and high field seeking states along the slowing path [21, 22]. An ingenious scheme by Zeppenfeld et al [23] uses an electrode with the form of a rotating spiral. Here the electric field guides the molecules along the spiral, whereas the rotation leads to a centrifugal potential which the molecules need to climb up and are slowed down while doing so. All these methods are rather general and can be implemented for a very broad range of molecules as the only requirement is a sizable electric or magnetic dipole moment. In practice only relatively light molecules are decelerated by this technique. But deceleration of heavier particles is under way [24, 25]. Still most techniques conserve phase space and provide only deceleration rather than cooling[1].

Optoelectrical Cooling

In optoelectrical cooling [26] the molecules are confined in an electrostatic potential in weak field seeking states. On the sides of the potential, at which point the molecule converted most of its kinetic energy to potential energy, it is transferred via a radio frequency to a weaker confined low field seeking state. Therefore it gains less energy traveling back to the trap center than it has lost climbing the potential hill before. The molecule is then pumped back to the stronger confined state in the low potential region of the trap. The result is a Sisyphus type cooling, which is applicable to a large class of molecules, where the only requirement is a sufficiently fast spontaneous decay in the pumping between the strong and weak confined state realized in the low field region between two vibrational states in [27, 26]. A gas of $N = 3 \cdot 10^5$ H_2CO molecules at a temperature of $T = 420\,\mu\mathrm{K}$ has been trapped using this scheme. The temperature in the experiment is limited due to technical issues with surface charges on the trap electrodes [27]. The cooling rate at low temperatures is principally limited due to the time the slow particles need to travel between high potential regions and low potential regions in the trap [26].

[1] There are ideas for longitudinal cooling in a continuous Zeeman Sisyphus decelerator by doppler sensitive pumping between low field and high field seeking states [21]

Laser Cooling of Molecules

Laser cooling of molecules produced the coldest samples within the direct cooling methods of $T = 5\,\mu K$ [28]. There are several proposals for further cooling [29, 30] and thereby quantum degeneracy might be in reach. Due to the optical cycling transitions found in these molecules the detection can be done optically in non destructive ways.

The scheme is limited to a certain class of molecules, where vibrational decay is limited due to a quasi diagonal Franck-Condon matrix. Still a large class of molecules was found for which the different rovibrational decay channels are suppressed enabling laser cooling schemes on these species. These enable the production of ultracold species, where the atomic constituents are not laser-coolable themselves. These include heavy species which are difficult to manipulate by static external fields and molecules which can be used for the search of an electron electric dipole moment or a nuclear anapole moment.

In the long run it maybe that not molecules are assembled from ultracold atoms but ultracold atoms are dissociated from ultracold molecules. This could generate species in the ultracold regime which are not laser-coolable by themselves [31, 32].

This Thesis

Chapter 2 gives a short introduction into laser cooling of molecules. The focus lies here on the discussion of problems arising due to the complex level structure, hindering the experimentalist to copy standard devices from ultracold atom laboratories.

Chapter 3 delineates a short requirement catalog for slowing of cryogenic buffer gas beams and gives a short summary about different radiative beam slowing methods.

Chapter 4 summarizes our radiative beam slowing idea on how a Zeeman slower can be implemented in the level structure of laser coolable molecules.

Chapter 5 presents the experimental implementation of the new Zeeman slower scheme on the D_1-line of ^{39}K and the comparison to other radiative beam slowing techniques implemented during this thesis namely white-light slowing and traditional Zeeman slowing.

Chapter 6 deals with the design and construction of a cryogenic beam source using ^{4}He as a buffer gas. We simulated the ^{4}He flow field with the computational fluid dynamics software OpenFOAM learning which circumstances lead to vortices inside the cell. We then describe how the apparatus is build and which components are used.

In chapter 7 first results of the extraction of a atomic ^{39}K beam from the cryogenic buffer gas beam source are presented and compared to simulations concerning the extraction of the cell on the one side and to simulations of the beam formation process on the other side.

In chapter 8 a short outlook is given.

2

Laser Cooling of Molecules

This chapter outlines the main steps in finding a quasi cycling transition for molecules and the consequences for the application of laser cooling in comparison to atomic laser cooling. Afterwards I give a short overview over a typical experimental apparatus and describe the state of the art and locate the differences to an experiment which successfully achieved quantum degeneracy in an atomic ensemble.

2.1. A Closed Cycling Transition in Diatomic Molecules

Laser cooling relies on the absorption of a large number of photons with a specific directed momentum and the following non directed spontaneous emission of photons resulting in a radiative force on the particle. The change in velocity after the absorption of a photon is called recoil velocity v_{rec} and lies for most atoms and molecules in the $v_{\mathrm{rec}} \approx 1\,\mathrm{cm\,s^{-1}}$ range. For bringing particles with thermal velocities of $v_{\mathrm{th}} \approx 100 - 1000\,\mathrm{m\,s^{-1}}$ to a standstill a large number of photons $n_{\mathrm{ph}} \approx 10^4 - 10^5$ must be scattered. In comparison to atoms, molecules possess additional degrees of freedom. For diatomics, which are being discussed here, there is one rotational and one vibrational mode. This additional level structure complicates the search of a closed cycling transition for cooling purposes. From an excited state the molecule can decay into rovibrational modes not addressed by the cooling laser which are then referred to as dark states for the cooling process. The challenge is to find transitions on which sufficient photons can be scattered before the molecule decays into such a dark state.

2.1.1. Vibrational Leakage

To prohibit the spontaneous decay into higher lying vibrational levels the molecule needs to be chosen wisely. As pointed out in [33] by DiRosa there is a large class of diatomic molecules, which exhibit quasi diagonal Franck-Condon structure limiting the vibrational branching. Later it became clear that this characteristic is not limited to diatomics [34, 35]. Generally one can estimate if a molecule has quasi diagonal Franck-Condon structure by investigating whether the valence electron responsible for the magnitude of the dipole matrix element of the transition is participating in the interatomic bond of the molecule [35]. If it does not, the bond is not perturbed if this electron is excited, thus the potential surfaces for the nuclei are similar in the ground and the excited state of the molecule. In this case the molecule will preferentially decay back to its original ground state. This situation can for example be found in earth alkaline monohalides. Here, the earth alkaline looses one of its valence electrons to the halide. Due to this electrovalence, the now positive earth alkaline

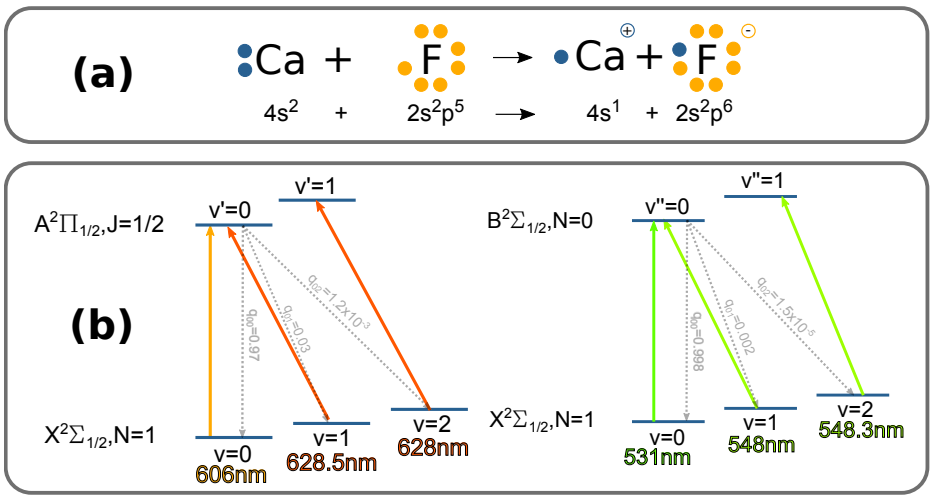

Figure 2.1.: Vibrational branching is mitigated through the choice of a suitable molecule. **(a)** An ionic bond in an earth alkaline monohalide molecule leaves one valence electron free, here for CaF. This radical has quasi diagonal Franck-Condon factors as the valence electron is not participating in the binding of the nuclei. **(b)** Franck-Condon factors for the first two electronically excited state for CaF, with the corresponding laser wavelengths.

cation and the negatively charged halide anion form an ionic bond, see figure 2.1**(a)**. The second valence electron left of the earth alkaline does not participate in the bonding and can be electronically excited without perturbing the potential surface of the nuclei. Figure 2.1 shows the situation for the example of $^{41}Ca^{19}F$. On the $X^2\Sigma_{1/2} \rightarrow A^2\Pi_{1/2}$ electronic transition two vibrational repump lasers are sufficient for beam slowing purposes , whereas on the $X^2\Sigma_{1/2} \rightarrow B^2\Sigma_{1/2}$ the branching ratios are even more favorable, as can be seen in Fig. 2.1 **(b)**.

2.1.2. Rotational Leakage

A rotationally closed transition can also be found as pointed out in [36]. Figure 2.2 shows the rotational structure of the $X^2\Sigma_{1/2}$ described in Hund's case (b)[1] electronic ground state and the first electronically excited state $A^2\Pi_{1/2}$ described in Hund's case (a) of an earth alkaline halide. N refers to the rotational quantum number and couples with the electron spin to form J. The hyperfine structure is not shown for simplicity and as it does not effect the conclusions drawn here. The levels of the rotational ladder in the X-State alternate in parity P subsequently [37], while each level in the excited state splits into two levels of opposite parity due to lambda doubling. Consider the X-state levels with N=1, which both have negative parity $P = -1$, are excited to the $A^2\Pi_{1/2}$ state with positive parity $P' = +1$. This excited state can only decay back to the N=1 levels of the X-state, since N=0,2 are forbidden by the parity selection rule for a dipolar transition $P' \cdot P = -1$ and decay in levels with N>3 is forbidden by the angular momentum selection rules $\Delta J = 0, \pm 1$. Note that this transition always involves so called type-II transitions where the angular momentum of the excited state is less or equal to that of the ground state, in this case $J = 1/2 \rightarrow J' = 1/2$ and $J = 3/2 \rightarrow J' = 1/2$. Every type-I transition with $J \rightarrow J' = J + 1$ is not rotationally closed and needs to be repumped via another type-II transition.

[1] A good description of the different Hund's cases can be found in [37]

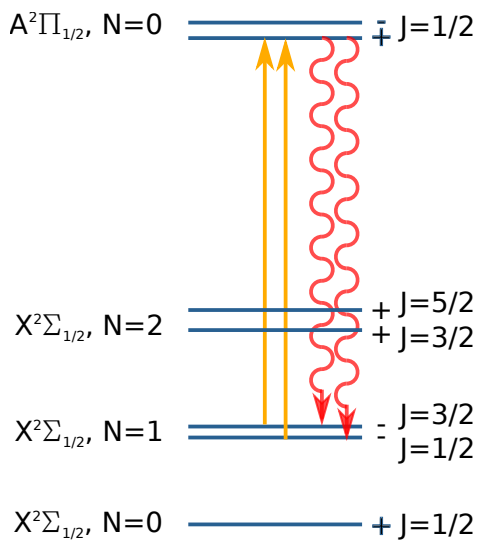

Figure 2.2.: Rotational ladder of CaF for the ground and the first electronically excited state. Due to the angular momentum selection rule $\Delta J = 0, \pm 1$ and the parity selection rule for an electric dipole transition $P' \cdot P = -1$, the transition $X^2\Sigma_{1/2}, N = 1, P = -1 \rightarrow A^2\Pi_{1/2}, N' = 0, P' = 1$ is rotationally closed.

2.1.3. Dark States and Other Problems

Laser cooling of atoms is typically applied on type-I transitions giving several advantages. First of all, there are no dark states in these systems. For every choice of polarization each ground state is coupled efficiently to an excited state. Consider for example the application of circularly polarized light on an atom aligned in a magnetic field in such a way that either σ^+ or σ^- transitions are driven as it is shown in figure 2.3**(a)**. The atom will be pumped to a transition between the stretched states $|J, m_J = \pm J\rangle \rightarrow |J', m_{J'} = J'\rangle$. These have the largest polarizability and are a closed 2-level cycling transition. For type-II level systems as they appear for laser coolable molecules the application of radiation pressure is not as straightforward as can be seen in figure 2.3**(b)**. For each choice of polarization the molecule will quickly be pumped into a dark state and the radiation pressure force will drop to zero.

When multiple polarizations are used each energy level itself can be coupled to an excited state level and there are no classical dark states. Consider for example the application of

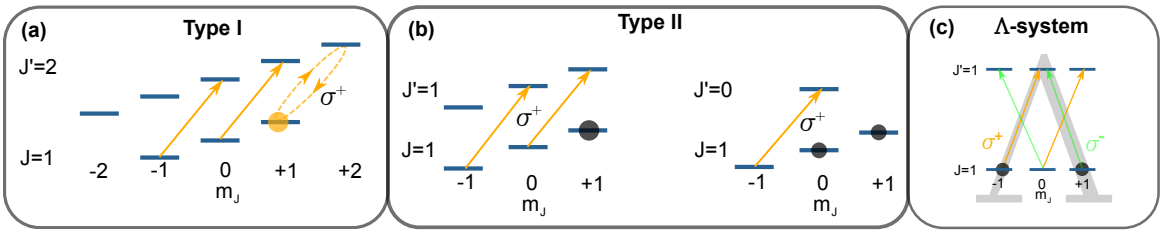

Figure 2.3.: Characteristics of photon cycling in type-I and type-II level systems. **(a)** In type-I level systems cycling is possible on a magnetically tunable two level transition and no dark states are present. **(b)** In type-II level systems there are dark states for every choice of polarization. Destabilization of dark states leads to coupling of every ground state level to an excited state level. The transition frequencies behave differently in a magnetic field, prohibiting the straightforward implementation of magneto optical traps and Zeeman slowers. **(c)** Mixed polarizations lead to Λ-type level structures where coherent dark states can be present.

light driving σ^+ and σ^- at the same time to the above system as in figure 2.3**(c)**. Here, two ground states are coupled to one excited state, leading to a so called Λ-system. The molecules will be pumped into a coherent superposition whose time evolution vanishes and the excited state will not be populated[38]. In this coherent dark state no more photons will be scattered.

But these dark states can be destabilized by either applying a magnetic field, switching the polarization with a frequency comparable to the excited state lifetime or the application of microwaves [38]. With this the efficient application of laser radiation pressure is possible and can be used to decelerate molecular beams [39, 40].

2.1.4. Radiation Pressure Force on a Diatomic Molecule

If each transition is driven with infinite laser intensity the population saturates in such a way that each state is populated with the same probability, the maximum attainable acceleration through radiation pressure is then given by

$$a_{\max} = \frac{N_\mathrm{e}}{N_\mathrm{g} + N_\mathrm{e}} \cdot \frac{\hbar k \Gamma}{m} \tag{2.1}$$

when N_g, N_e are the numbers of sublevels in the ground and excited state respectively. For a two level system found in atoms this saturates to $a_{\max} = \frac{1}{2} \cdot \frac{\hbar k \Gamma}{m}$.

This can be different in multilevel systems. Figure 2.4 shows the full level scheme on the example of earth alkaline halide with nuclear spin $I = 1/2$. There are $N_e = 4$ hyperfine levels in the excited state and $N_g = 12$ hyperfine levels in each vibrational ground state. When the vibrational repumper $\mathcal{L}_{01}$ for $\nu = 1$ is coupled to the same excited state as the main cooling laser $\mathcal{L}_{00}$ as it is shown in 2.4**(b)** the number of ground state doubles to $N_g = 24$ giving a maximum acceleration of $a_{\max} = \frac{1}{7} \cdot \frac{\hbar k \Gamma}{m}$. The repumping transition driven by $\mathcal{L}_{12}$ is independent and only a small fraction of photons will be scattered here, so that $a_{\max}$ is determined in the system driven by $\mathcal{L}_{00}$ and $\mathcal{L}_{01}$.

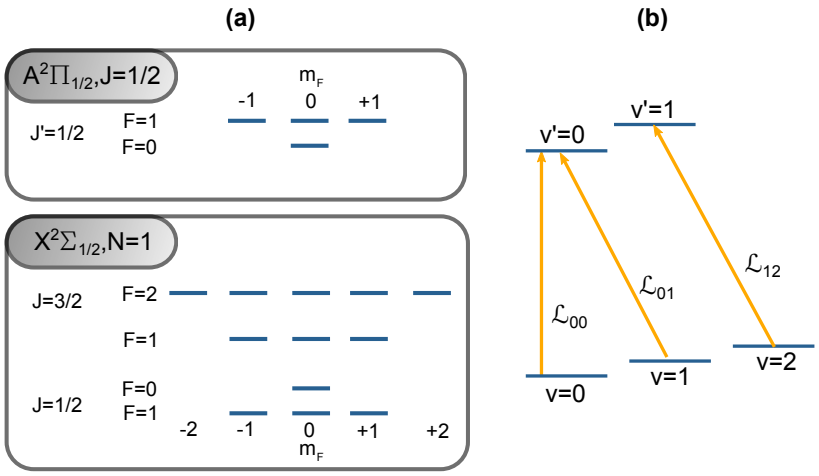

Figure 2.4.: **(a)**Full level system on the example of an earth alkaline halide with nuclear spin $I = 1/2$, which is the case for example in SrF and CaF. **(b)** For deceleration and cooling to the Doppler limit typically 2 vibrational repump lasers $\mathcal{L}_{01}$ and $\mathcal{L}_{12}$ are necessary. Here, $\mathcal{L}_{00}$ and $\mathcal{L}_{01}$ couple to the same excited states. The decays are not shown for clarity.

Still, it turns out that for many laser coolable molecules there are multiple electronic states with quasi diagonal Franck-Condon structure. In figure 2.1 the second electronically excited state $B^2\Sigma_{1/2}$ was mentioned with its corresponding Franck-Condon structure and this state can be included in the vibrational repumping. Thereby the number of excited

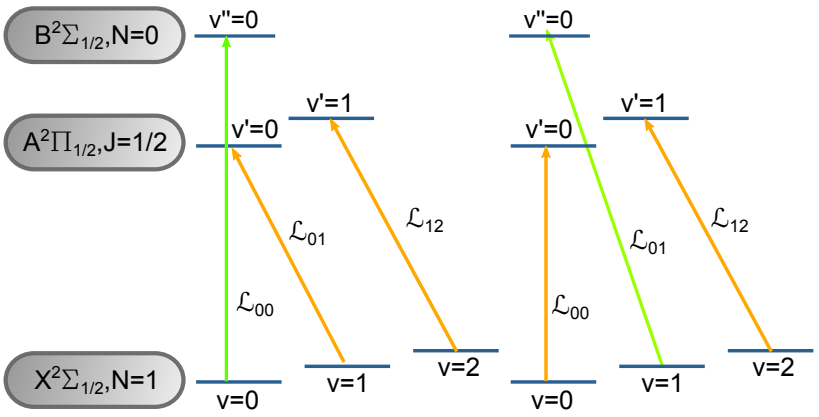

Figure 2.5.: Two alternative vibrational repumping scheme leading to higher maximum achievable scattering rates due to the involvement of an increased number of excited states.

states can be enhanced to $N_e = 8$ in the repumping schemes shown in figure 2.5 bringing the maximum attainable acceleration to $a_{\max} = \frac{1}{4} \cdot \frac{\hbar k \Gamma}{m}$[2]. The only requirement here is that the second electronic excited state does not decay in a cascade over the first excited state, this would mean a change of parity in the ground state for a molecule experiencing such a 3-photon cycle and they would be lost for a further experiment. The intensities needed to achieve $a_{\max}$ can be different for the two schemes shown in 2.5 and depend on the Franck Condon factors of both excited states.

2.1.5. Benefits in a Type-II Level Structure

While the type-II level structure increases the complexity at the early stages of the experiment in steps such as beam slowing and trapping, it also comprises true benefits for the subsequent cooling stages. The Λ-like structure found in the type-II level scheme is similar to the D_1-line found in alkali atoms and is therefore suitable for sub-Doppler cooling in blue detuned light, like gray molasses cooling. This robust molasses technique leads to temperatures for the molecular ensembles of $T_{subD} \approx 50\,\mu\text{K}$ [41, 42]. Recently Λ-enhanced velocity selective coherent population trapping has also been shown yielding a free space temperature of $5\,\mu\text{K}$ [28]. Furthermore it has been seen that the gray molasses cooling is effective in optical dipole traps [43] and still works although the dipole trap leads to different stark shifts of the sublevels due to varying coupling strengths to the excited state. This can have great potential since phase space density might be subsequently increased by compressing the molecular ensemble in an increasing gradient dipole trap and the consequential heating can be eliminated by in-trap cooling.

2.2. Typical Experiment

Experiments towards the goal of producing ultracold molecules by the means of direct laser cooling follow a common route to each other and in a sense resemble the experimental structure used in ultracold atom laboratories.

First, a pre-cooled molecular beam is formed where the molecules predominantly populate the lowest lying rotational and vibrational states. The internal temperature after the pre-cooling stage typically lies around $T_{int} \approx 1\,\text{K}$ [17, 44]. Most often cryogenic buffer gas beam sources are used where the longitudinal velocity distribution is centered at $v_{\parallel cen} \approx$

[2] Most photons will be scattered from $\mathcal{L}_{00}$ so it is a good approximation to use k and Γ from this transition to calculate $a_{\max}$

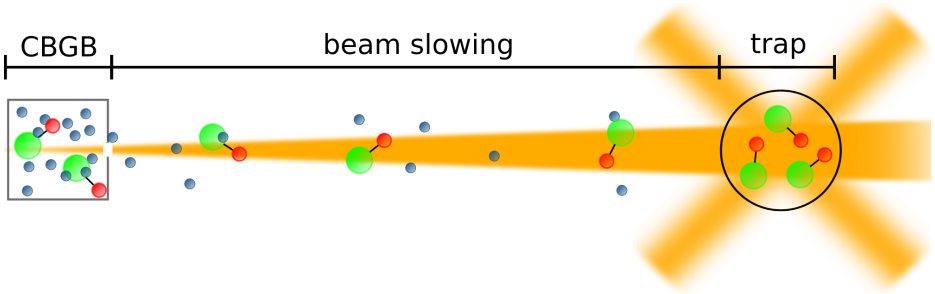

Figure 2.6.: Sketch of a typical experimental apparatus for direct laser cooling of molecules. The cryogenic buffer gas beam source (CBGB) pre-cools the molecules to a few Kelvin through collisions with cold Helium gas. A beam is formed through a hole in the CBGB and is then slowed down by radiation pressure from a counter-propagating laser beam. Behind the beam slowing region a magneto optical trap captures the molecules and cools them further.

$120 - 160\,\mathrm{m\,s^{-1}}$ for one stage buffer gas beam sources or between $v_{\parallel cen} \approx 35 - 90\,\mathrm{m\,s^{-1}}$ for two stage buffer gas beam sources [17]. These beams are then slowed down via radiation pressure from counter-propagating laser beams to a velocity around $v_{end} \approx 10\,\mathrm{m\,s^{-1}}$ along a slowing distance between $50 - 150\,\mathrm{cm}$ [39, 40, 45, 46]. To cover the resonance condition of the slowing laser with the molecules over the whole Doppler range from capture velocity to final velocity of the slowing process, the frequency of the laser is either chirped [40, 45] in time or it is frequency broadened [39, 46]. The slow molecules can then be trapped in a molecular magneto optical trap. This procedure has been successfully implemented for three types of molecules $^{40}Ca^{19}F$ [41, 42],$^{88}Sr^{19}F$[47] and $^{89}Y^{16}O$[48]. A sketch of a typical experiment is shown in figure 2.6.

2.3. State of the Art

Experiments involving direct laser cooling of molecules are developing at a fast pace. Since the first realization of a three dimensional magneto optical trap in 2014 [47] which reached a temperature of $T = 2.5\,\mathrm{mK}$ at a molecule number of $N = 300$ for $^{88}Sr^{19}F$ there has been subsequent improvements. The most recent results we are aware of are $T = 340\,\mu\mathrm{K}$ and $N = 1.1 \cdot 10^5$ for $^{40}Ca^{19}F$ in 2017 [42] showing the rapid progress in the field.

Important steps for improvement have been the involvement of different electronically excited states for the vibrational repumping during the beam slowing as shown in 2.5 [40]. A second ingredient for raising the molecule number has been the work in [52, 53, 54] which gave the theoretical background of the capture and cooling processes at work in type-II magneto-optical traps. This led to capture schemes such as the two color MOT and the radio frequency MOT[3] which outperform the methods used before [56, 42, 41].

After the initial trapping the molecules can be cooled further with blue detuned optical molasses [41] and can afterwards be loaded into conservative traps, such as magnetic [57, 58] or optical traps [43]. Table 2.1 shows results obtained at different stages in current experiments.

The fifth column of table 2.1 shows the results of a typical atomic experiment which produced a Bose Einstein condensate of $1.1 \cdot 10^6$ ^{23}Na-atoms in our neighboring laboratory [59, 60, 61]. Compared to the molecular experiments the temperatures reached at the different stages show similar results. This is different for the number of molecules which is 4-5 orders of magnitude lower than compared to the atomic case. If the experiments aim for high phase

[3] the RF-MOT was already shown before to have an advantage in two dimensions and the processes have been explained qualitatively [55]

	Harvard $^{40}Ca^{19}F$ [43]	Imperial $^{40}Ca^{19}F$ [49, 50]	Yale $^{88}Sr^{19}F$ [51]	Boulder $^{89}Y^{16}O$	Hannover ^{23}Na
N_{MOT}	10^5	$2 \cdot 10^4$	10^4	$1.5 \cdot 10^4$	$3 \cdot 10^9$
T_{MOT}	350 µK	730 µK	250 µK	7 mK	(235 µK)
T_{subD}	40 µK	55 µK	50 µK	–	50 µK
N_{mag}	–	$5 \cdot 10^3$	10^3	–	$1 \cdot 10^9$
T_{mag}	–	70 µK	240 µK	–	100 µK
N_{opt}	150	–	–	–	10^7
T_{opt}	60 µK	–	–	–	10 µK
ρ_{ps}	$2 \cdot 10^{-9}$	$2.6 \cdot 10^{-12}$	$6 \cdot 10^{-14}$	–	> 2.6
N_{con}	–	–	–	–	$1.1 \cdot 10^6$
(T_{con})	–	–	–	–	(80 nK)

Table 2.1.: State of the art of current experiments involving direct laser cooling and trapping of molecules. The phase space density ρ_{ps} given corresponds to the highest achieved in the given experiment. The temperatures in the MOT's T_{MOT} is after the ramp down of the laser intensity which is done after an initial capture sequence.

space densities to reach quantum degeneracy, increasing the molecule number is a must. The striking molecule number difference has its origin in the loading phase of the MOT, where the combination of slowing method and buffer gas beam source leads to relatively low fluxes at trappable velocities. The losses in the subsequent stages are comparatively moderate.

Possible pathways for the future would be to overlay the trapped molecules with laser-cooled atoms for the purpose of collisional studies or sympathetic cooling. If the captured number of molecules is high enough evaporative cooling can be studied to reach even lower temperatures. This step has not been shown for the molecules of interest up to now but there are promising proposals [62, 29] that evaporative cooling could be highly efficient by shielding inelastic processes with the application of blue detuned microwaves or a combination of static electric and magnetic fields. Still, with the low molecule numbers achieved in the experiments up to now evaporative cooling might be challenging.

3

Slowing of a Molecular Beam

Parts of this chapter have also been published elsewhere [63, 64]. The following chapter is to some extent identical to these publications.

3.1. Requirement Catalog of Molecular Beam Slowing

The brightest beams of laser coolable molecules are produced by laser ablation loaded buffer gas beam sources. These produce beams with forward velocities of $v_{\parallel} \approx 120 - 150\,\mathrm{m\,s^{-1}}$ with a longitudinal velocity spread characterized by a full width at half maximum of $\Delta v_{\parallel} \approx 40 - 70\,\mathrm{m\,s^{-1}}$. The produced molecular pulses have a temporal shape with a characteristic timescale Δt of several ms. In order to be trapped in magneto-optical traps the particles coming from such a source need to be slowed from their initial velocities down to velocities v_{cap} trappable by the magneto-optical trap of about $v_{\mathrm{cap}} \approx 5 - 11\,\mathrm{m\,s^{-1}}$ [42, 50]. For an exemplary cell with $v_{\parallel} = 140\,\mathrm{m\,s^{-1}}$ and a temporal pulse width of $\Delta t = 3\mathrm{ms}$ the molecular pulse has a spatial extent along the center beam line of at least $\Delta z \approx 0.4\,\mathrm{m}$. Along to the spatial extension of the molecular pulse comes the aforementioned longitudinal velocity spread showing that a following slowing device needs a large phase space acceptance.

The best slowing method would ensure that all molecules traverse the trapping region downstream of the source with a velocity equal to or lower than the trapping velocity of the molecular magneto-optical trap. To ensure that, the method would ideally be continuous in comparison to the pulse width of the buffer gas source and it would be dissipative to compress the whole longitudinal velocity distribution into the narrow trappable velocity window. While a variety of slowing methods for rovibrationally cold molecular beams exist, including two stage buffer gas cooling [65], Stark and Zeeman deceleration [66, 20], centrifuge deceleration [23], white-light slowing [39, 46] and chirped light slowing [40, 45], all shown techniques are either not continuous, have only poor control on the final velocity or do not compress the 1-dimensional velocity distribution of the molecules. This limits the number of molecules loaded into magnetic or magneto-optical traps to a fraction of the numbers in atomic experiments [42, 41, 56, 67].

3.1.1. Stark and Zeeman Deceleration

The most investigated slowing technique for molecules is the Stark decelerator. In practice this can only be used if the electric dipole to mass ratio is comparably large such that the stopping distance is not extensively long. The same is the case for a Zeeman decelerator, where the magnetic moment to mass ratio needs to be relatively large. Both circumstances

are not given for most laser coolable molecules. Additionally these devices work with pulsed fields and therefore they are not well suited to slow down molecular beams coming from cryogenic buffer gas beam sources due to their low phase space acceptance. Instead they are typically seeded with supersonic expansion beam sources which lead to considerably faster beams [17]. Therefore nearly all experiments work with radiative beam slowing techniques rather than using external electric or magnetic fields to slow down the molecular beam. Recently a buffer gas cell emitting pulses with a duration of $t = 240\,\mu s$ has been realized, how a cell of the same design can be coupled to a Stark decelerator is currently investigated [68].

3.1.2. Slowing with stimulated light forces

There are several proposals suggesting to slow a molecular beam with stimulated light forces. Either in a standing wave leading to the bichromatic force [69] or with co- and counter-propagating chirped laser pulses driving the population of the molecule back and forth between the ground and the excited state [70]. The bichromatic force has recently been used to deflect a molecular beam [71, 72]. These schemes can work continuously and are principally suitable to slow down molecules from cryogenic buffer gas beam sources. The big advantage of these slowing methods is the high deceleration force which is not limited by the lifetime of the excited state. Another benefit is that spontaneous emission can be efficiently reduced during the slowing process. Therefore the schemes can be used for molecules where the Franck-Condon Matrix is not as diagonal as it is needed for radiative slowing. Despite these advantages, the big technical challenge is their demand of very high laser intensities $I > \mathrm{kW\,cm^{-2}}$, for the force to be large compared to the radiative force. With available laser systems this leads to very small slowing beam diameters $w < 1\,\mathrm{mm}$, such that only a very small portion of the beam can be slowed. Still, these techniques are considered and may be used for efficient beam slowing in the future.

3.2. Radiative Beam Slowing Methods

Due to the aforementioned drawbacks of the other methods most experiments use radiative beam slowing methods on which we want to focus from here on. Slowing of a molecular beam can be achieved by shining in a resonant counter-propagating laser beam. By directed absorption and undirected emission of photons the particles are slowed down by the radiation pressure. The frequency of the slowing laser dictates the velocity classes being slowed down due to the corresponding Doppler shifts. For efficient deceleration the resonance condition has to be met by the slowing laser over the whole velocity range. In principle, there are three different methods to accomplish this. Firstly, the slowing laser can be frequency broadened so that all velocity classes are resonant (white-light slowing). Secondly, the frequency of the slowing laser can be chirped in time, so that the resonance condition is fulfilled while the particles are slowed down (chirped light slowing). Lastly, the resonance frequency of the particles is altered in a spatially inhomogeneous magnetic field (Zeeman slowing). Figure 3.1 **(a)** shows the force profiles of these three different slowing methods along with corresponding time **(b)** and space **(c)** trajectories of particles with different velocities during the slowing process. The bottom row shows the corresponding graphs for Zeeman slowing, where the force profile is altered along the slowing path. It is the only method where all particles reach their final velocity at the same point in space. Whereas for white-light slowing and chirped light slowing the particles reach the target velocity at different points in space and the width of the velocity distribution is thereby projected on the slowing path. Zeeman slowing and white-light slowing are continuous methods while chirped light slowing, due to its nature will lead to pulses of slow particles.

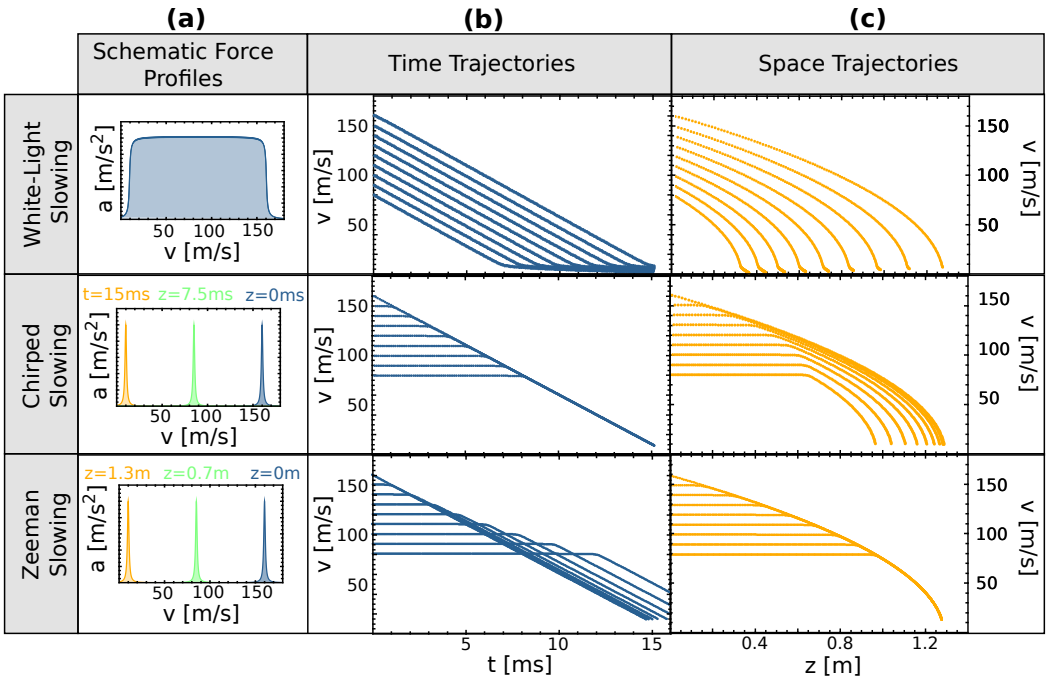

Figure 3.1.: **(a)** Application of the deceleration force when $a_{\max} = 10^5\,\mathrm{m\,s^{-2}}$ of different radiation pressure slowing methods while decelerating particles from $160\,\mathrm{m\,s^{-1}}$ down to $10\,\mathrm{m\,s^{-1}}$. **(b)** One dimensional velocity trajectory simulations over time t during the slowing process. **(c)** One dimensional velocity trajectory simulations over slowing distance z during the slowing process. Note that Zeeman slowing is the only method where all particles reach the target velocity at the same point in space

When it comes to trap loading the most often used technique in atomic experiments is Zeeman slowing. The reason lies in the fact, that for trap loading the particles have to traverse a specific trap volume with a velocity equal to or lower than the corresponding capture velocity of the trap. So far we have only talked about one dimension. Any additional transverse velocity can lead to a loss of particles due to transverse spreading. This effect is minimized if the time the particles need to reach the trap volume is reduced. This is another benefit of the Zeeman slowing technique as all particles first fly with their initial velocity and are only slowed down when it is needed, therefore losses due to transverse spreading are efficiently lessened. Furthermore, it combines the advantageous characteristics of the other slowing methods, being continuous as in white-light slowing and having a well defined final velocity as chirped light slowing. All these effects add up and make Zeeman slowing the most effective radiative slowing method for the purpose of trap loading.

4

A Zeeman Slower for Diatomic Molecules

During the time of this thesis a Zeeman slower scheme for laser-coolable molecules has been developed, capable of continuous deceleration and compression of the molecular velocity distribution down to velocities in the $10\,\mathrm{m\,s^{-1}}$ range. Zeeman slowing was considered to be impossible to implement for laser-coolable molecules working on a $X^2\Sigma_{1/2}, N=1, \nu=0 \rightarrow A^2\Pi_{1/2}, J'=1/2, \nu'=0$ transition before [39, 45].

Here I shortly review the traditional atomic Zeeman slower concept, discuss problems arising from the complex molecular level structure and show how these problems can be overcome with our molecular Zeeman slowing concept. Parts of this chapter have also been published elsewhere [63]. The following chapter is to some extent identical to this publication.

4.1. Type-I and Type-II Zeeman Slowing

A traditional atomic Zeeman slower [73] works on a type-I level structure, where the angular momentum of the excited state $J' = J+1$ is larger than that of the ground state J. Here the atoms get pumped into a bright, stretched state at which point they cycle in an effective 2-level system [73], whose transition frequency is tunable by a magnetic field. The atomic beam is then radiatively slowed down by a counter-propagating laser beam while an inhomogeneous magnetic field compensates the changing Doppler shift during the slowing process down to a well defined final velocity. In analogy to magneto-optical traps (MOTs) working on a type-I level structure (typically referred to as type-I MOTs) we will refer to this as type-I Zeeman slowing.

In contrast, laser cooling of molecules always involves a type-II level transition ($J \rightarrow J' = J$ or $J \rightarrow J' = J-1$) [36]. As a natural consequence, molecules are optically pumped into dark magnetic sublevels rather than bright ones and a 2-level cycling transition does not exist. Nevertheless, slowing and cooling of molecules using laser light has been realized by destabilizing these dark states [38]. As a result, all magnetic sublevels of the ground state need to be coupled to the excited state, each of which will exhibit a different shift in energy in a magnetic field, thus preventing the implementation of a traditional Zeeman slower in these type-II systems.

We propose a solution to this problem for laser-coolable molecular radicals working on the $X^2\Sigma_{1/2}, N=1, \nu=0$ (ground state described in Hund's case b) to $A^2\Pi_{1/2}, J'=1/2, \nu'=0$ (excited state described in Hund's case a) transition, where ν, ν' are the respective vibrational quantum numbers, N is the rotational angular momentum in the ground state and J' is

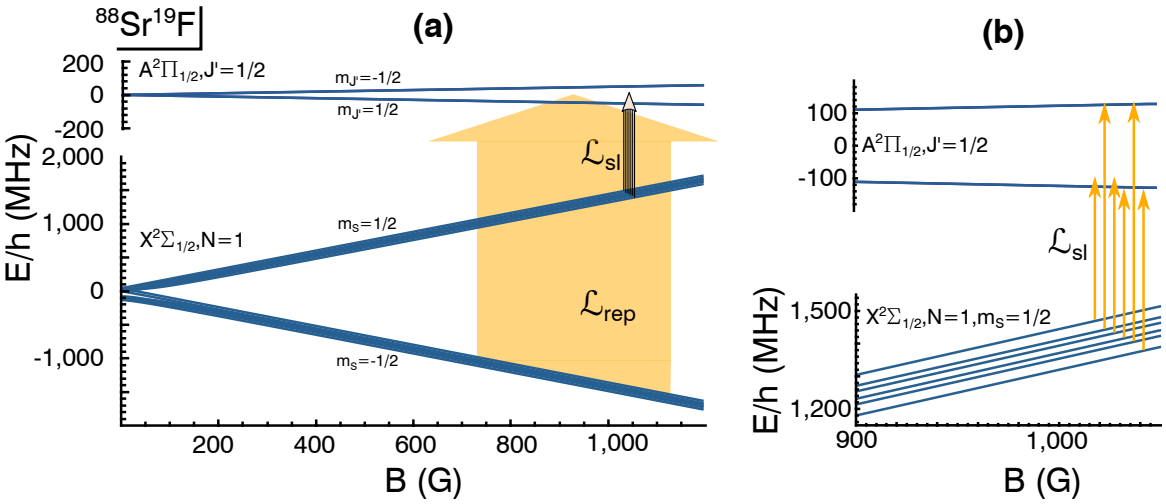

Figure 4.1.: **(a)** Type II Zeeman slower scheme on the $X^2\Sigma_{1/2}, N = 1, \nu = 0 \rightarrow A^2\Pi_{1/2}, J' = 1/2, \nu' = 0$ transition. As long as $g_\Pi \ll g_\Sigma$ the level structure in high magnetic fields resembles an effective 3-level system. The graph is shown for the prototype molecule $^{88}Sr^{19}F$. Note that the widths of the arrows are symbolizing the spectral widths of the involved lasers. **(b)** Necessary sidebands on the slowing laser $\mathcal{L}_{\text{sl}}$.

the total angular momentum in the excited state. By adding a large magnetic offset field B_0 to the traditional Zeeman slower design, the electron spin decouples from the nuclear and rotational angular momenta in the ground state, splitting it into two manifolds with $m_S = \pm 1/2$ (see Fig. 4.1 a). The sublevels inside these respective manifolds are shifted equally in energy with increasing or decreasing magnetic field strength. The excited state splits into $m'_J = \pm 1/2$ manifolds with a much smaller splitting due to a smaller g-factor $g_\Pi \ll g_\Sigma$. In the limit of negligible hyperfine structure and vanishing g_Π, this reduces to an effective 3-level system (see Fig. 4.1 a).

To implement a type-II Zeeman slower in this 3-level system, the $m_S = 1/2$ manifold of the ground state is coupled to the excited state via a narrow linewidth (on the order of the transition linewidth), counter-propagating laser beam at saturation intensity. This transition is magnetically tunable and therefore can be used to compensate for a changing Doppler shift during the slowing process, as it is done in traditional type-I Zeeman slowing. In the following, we will refer to this laser beam as the "slowing laser" $\mathcal{L}_{\text{sl}}$. Due to the large spin orbit coupling in the excited state, molecules can decay back to either $m_S = 1/2$ or to $m_S = -1/2$. A frequency broadened laser (in the following referred to as the "repumping laser" $\mathcal{L}_{\text{rep}}$) pumps molecules at all relevant velocities and magnetic fields from $m_S = -1/2$ back to the slowing transition. Molecules traveling fast enough to see $\mathcal{L}_{\text{sl}}$ on resonance due to the Doppler shift, get pumped between the $m_S = \pm 1/2$ manifolds by scattering photons from $\mathcal{L}_{\text{sl}}$ and $\mathcal{L}_{\text{rep}}$ until they are shifted out of resonance with $\mathcal{L}_{\text{sl}}$. Further slowing of the molecules occurs with changing magnetic field, bringing the molecules back into resonance with $\mathcal{L}_{\text{sl}}$. Since slower molecules feel no force while faster ones are being slowed down, we achieve both compression of the velocity distribution and reduction of the mean molecular velocity by spatially varying the magnetic field.

In a realistic system, including finite hyperfine structure of the ground state as well as a small upper state g-factor g_Π, the slowing laser $\mathcal{L}_{\text{sl}}$ needs to couple every hyperfine state in the $m_S = +1/2$ ground state manifold to the excited state as shown in Fig. 4.1 **(b)**. This can be realized by a suitable choice of sideband frequencies. The sublevels in the $X^2\Sigma_{1/2}, N = 1, m_S = 1/2$ manifold have a parallel slope in a magnetic field as was argued before. This is not the case for the sublevels in $A^2\Pi_{1/2}, J' = 1/2$. For a high radiation pressure force the ground state needs to be coupled to both excited state manifolds $m_J = \pm 1/2$. A high deceleration force is achieved when the sidebands are detuned by

$\delta = \pm\Gamma/2$ to destabilize coherent dark states effectively, while still being as resonant as possible. The choice of sideband frequencies however can not be perfectly $\pm\Gamma/2$ over the whole magnetic field range for all sublevels coupled due to the finite g_Π. But the smaller the g-factor of the excited state, the better a choice of sideband frequencies of $\mathcal{L}_{\mathrm{sl}}$ can be given.

Therefore our scheme is applicable to all laser-coolable molecules, where $g_\Pi \ll g_\Sigma$, so that the simplified 3-level picture holds in the Paschen-Back regime including for example SrF,$g_\Pi \approx -0.08$, CaF,$g_\Pi \approx -0.02$ and YO,$g_\Pi \approx -0.06$.

4.2. Force Profiles for $^{88}Sr^{19}F$ and $^{40}Ca^{19}F$

To go beyond the qualitative discussion of a three-level system and demonstrate the feasibility of the scheme in a realistic system including hyperfine structure, we now focus on two prototype molecules $^{88}Sr^{19}F$ and $^{40}Ca^{19}F$, both with nuclear spin $I = 1/2$. The text details the situation for $^{88}Sr^{19}F$, but all conclusions drawn here can be directly applied to $^{40}Ca^{19}F$ as well.

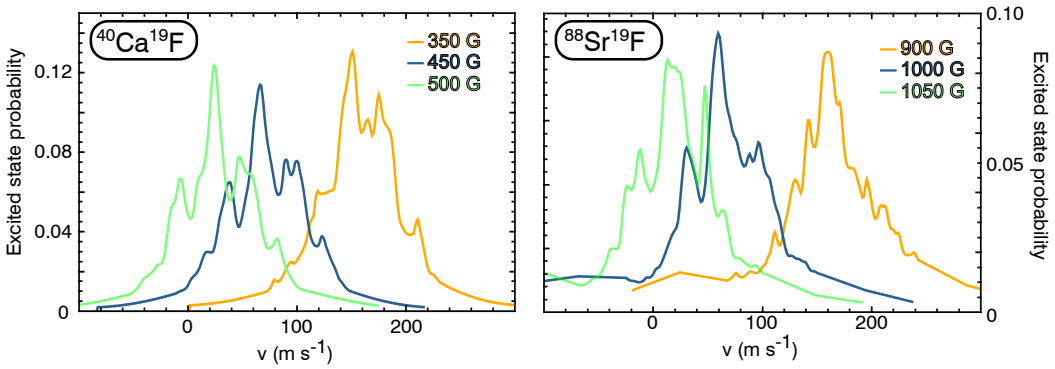

Figure 4.2.: Velocity dependent Zeeman slower force profiles and corresponding excited state probabilities at different magnetic fields for the example molecules $^{40}Ca^{19}F$ and $^{88}Sr^{19}F$ (for details see text). The substructure in the profiles emerges due to the hyperfine structure of the ground state and the finite excited state g_Π.

Fig. 4.1 **(a)** shows a plot of the $X^2\Sigma_{1/2}, N = 1, \nu = 0 \rightarrow A^2\Pi_{1/2}, J' = 1/2, \nu' = 0$ level structure as a function of magnetic field for the example molecule $^{88}Sr^{19}F$. The ground state manifolds $m_S = \pm 1/2$ each split into 6 sublevels ($m_N = -1,0,+1; m_I = \pm 1/2$), due to rotational and hyperfine structure, which have to be coupled to the 4 sublevels of the $A^2\Pi_{1/2}, J' = 1/2, \nu' = 0$ state ($m_J = \pm 1/2; m_I = \pm 1/2$) via the slowing laser $\mathcal{L}_{\mathrm{sl}}$ as shown in Fig. 4.1 b). This specific system thus requires a slowing laser $\mathcal{L}_{\mathrm{sl}}$ with 6 sidebands. Pairs of frequencies of $\mathcal{L}_{\mathrm{sl}}$ that couple to the same excited state are detuned by $\delta = \pm\Gamma/2$ from resonance to avoid pumping into coherent dark states.Furthermore, a broad repumper $\mathcal{L}_{\mathrm{rep}}$ with a width of $\Delta f \approx 1.1\,\mathrm{GHz}$ is required to pump $m_S = -1/2$ molecules back into the cooling cycle. To calculate the velocity dependent force profile along the slowing path, we solve the 16-level optical Bloch equations [74] at magnetic offset fields of $B = 900\,\mathrm{G}, B = 1000\,\mathrm{G}$ and $B = 1050\,\mathrm{G}$ respectively ($B = 350\,\mathrm{G}, B = 450\,\mathrm{G}$ and $B = 500\,\mathrm{G}$ for $^{40}Ca^{19}F$).[1] Each frequency in the slowing laser $\mathcal{L}_{\mathrm{sl}}$ is assumed to have an intensity corresponding to a Rabi frequency of $\Omega_{ij} = 2\Gamma d_{ij}$ where d_{ij} is the normalized dipole matrix element of the respective

[1] The energies and transition rates between the levels are calculated by diagonalizing the molecular Hamiltonian including interactions with external magnetic fields in the Hund's case a) basis, and calculating the matrix elements of the dipole operator between the resulting eigenstates [75]. Decay in the simulation is taken into account by writing the problem in form of the Liouville equation [38]. Decays of excited state coherences into ground state coherences are not taken into account, as these decays are not expected to result in additional dark states.

transition. Coupling from the $m_S = -1/2$ states with the repump laser $\mathcal{L}_{\text{rep}}$ is modeled by an electric field, frequency modulated at ω_{mod} corresponding to $\Omega_{ij} = 12\Gamma d_{ij}$. Table 4.1 lists the intensities and modulation frequencies used for the optical Bloch equation. Due to the modulation, no additional dark states arise from $\mathcal{L}_{\text{rep}}$. The calculation results in a narrow velocity-dependent force profile, which can be tuned over the whole relevant velocity range by a spatially varying magnetic field, consistent with the idea of Zeeman slowing (see Fig. 4.2).

	^{40}Ca^{19}F	^{88}Sr^{19}F
Γ [MHz]	$2\pi \times 8.3$	$2\pi \times 6.6$
I_{sl} [mW cm^{-2}]	12	24
I_{rep} [mW cm^{-2}]	1.4	0.86
ω_{mod}	$\pi\Gamma$	$\pi\Gamma$
M	25.4	27
Δf_{rep} [GHz]	1.1	1.1

Table 4.1.: Parameters used to calculate the velocity dependent force profiles for ^{40}Ca^{19}F and ^{88}Sr^{19}F. Here, Γ is the transition linewidth, I_{sl} is the intensity per sideband of $\mathcal{L}_{\text{sl}}$ and I_{rep} is the total intensity of $\mathcal{L}_{\text{rep}}$. ω_{mod} and M is the frequency and modulation index with which $\mathcal{L}_{\text{rep}}$ is modulated. Δf_{rep} is the approximate frequency width resulting from the modulation.

4.3. Monte Carlo Simulation of the Slowing Process

We now use the force profile from Fig. 4.2 in a 3D Monte Carlo simulation to calculate the velocity profile of Zeeman slowed ^{88}Sr^{19}F molecules originating from a typical cryogenic buffer gas cell. Table 4.2 lists the parameters of the initial velocity distributions fed into the simulations and the obtained slowed velocities.

Effects due to vibrational repumping are taken into account by dividing the force profiles in Fig. 4.2 by a safety factor of 2 resulting in a deceleration parameter[2] of $\eta = 0.19$. We take heating effects during the slowing process due to spontaneous emission into account. The detection region is chosen to be located at z_{det} behind the magnetic field maximum of the Zeeman slower field and is chosen to be a square with sides of length 1 cm. Note that the width of the slowed peak is much smaller than the width of the slowing force from Fig. 4.2, since the width after slowing is given by the steep slope of the force profiles around the central peak and the fact, that the slowing force quickly vanishes at the end of the Zeeman slower in the rapidly falling magnetic field [77, 78]. Due to the combination of slowing and compression characteristic for a Zeeman slower, a significant fraction of molecules exits the Zeeman slower with velocities low enough to be efficiently captured with existing trapping schemes.

[2] We define $\eta = \frac{a}{a_{\text{max}}}$ where $a_{\text{max}} = \frac{N_{\text{e}}}{N_{\text{g}}+N_{\text{e}}} \cdot \frac{\hbar k}{\gamma m}$ is the maximum achievable deceleration achieved at infinite laser power on a transition where N_{e},N_{g} are the number of excited states and ground states respectively [76].

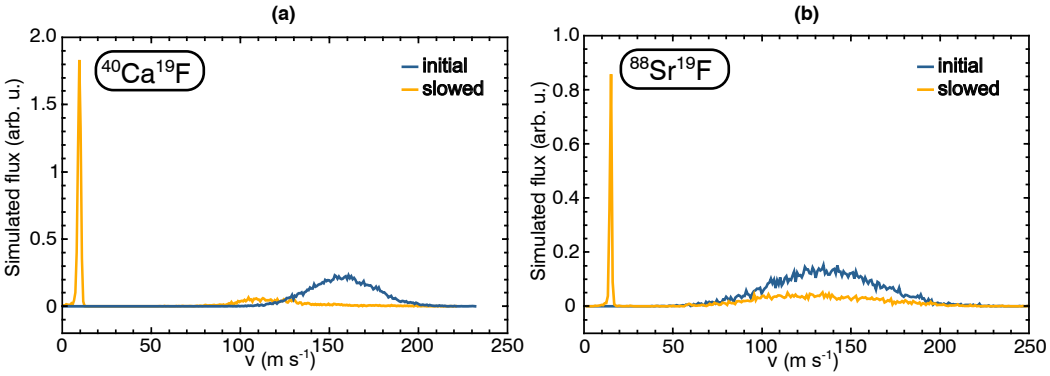

Figure 4.3.: 3D Monte Carlo simulation of Zeeman slowing for a $^{88}Sr^{19}F$ molecular beam originating from a buffer gas cell. Blue: Initial velocity distribution detected at $z_{det} = 1.58\,\mathrm{m}$ behind the buffer gas cell. Orange: Slowed distribution based on the force profile from Fig. 4.2. 15 % of the molecules are within the peak centered around $v_p = 15\,\mathrm{m\,s^{-1}}$. Further details about the simulation can be found in the text.

	$^{40}Ca^{19}F$	$^{88}Sr^{19}F$
$v_{\parallel}\,[\mathrm{m\,s^{-1}}]$	158	120
$\Delta v_{\parallel}\,[\mathrm{m\,s^{-1}}]$	45	75
$\Delta v_{\perp}\,[\mathrm{m\,s^{-1}}]$	50	80
Coil length [m]	0.4	1.2
$B_{\mathrm{min}}\,[\mathrm{G}]$	350	900
$B_{\mathrm{max}}\,[\mathrm{G}]$	480	1030
$v_{\mathrm{p}}\,[\mathrm{m\,s^{-1}}]$	9	15
$\Delta v_{\mathrm{p}}\,[\mathrm{m\,s^{-1}}]$	2.5	2.5

Table 4.2.: Parameters used for the shown Monte Carlo simulation. The simulation of $^{88}Sr^{19}F$ is identical to the one described in [63] and was based on the geometry of our demonstration experiment described in chapter 5. The parameters given for $^{40}Ca^{19}F$ are an optimized geometry, which we plan to use in a later molecular experiment. Here $v_{\parallel}$,$\Delta v_{\parallel}$ are the longitudinal center velocity and the FWHM velocity spread of the initial distribution. $\Delta v_{\perp}$ is the FWHM of the transverse velocity distribution. The coil length gives the length of the solenoid producing the magnetic field. v_p is the peak velocity of the slowed distribution and Δv_p the corresponding width.

4.4. Choice of the Molecule

While in the publication [63] we introduced the type-II Zeeman slowing scheme and decided to use $^{88}Sr^{19}F$ as an example, we finally decided to use a different molecule, namely $^{40}Ca^{19}F$, for the experiment in our institute. Here we just want to give a short overview, which circumstances have driven us to this decision.

Figure 4.2 shows the force profiles obtained from the optical Bloch equations described before. CaF has a smaller upper state g-factor $g_\Pi = 0.02$, in comparison to SrF $g_\Pi = 0.08$, therefore the sidebands of $\mathcal{L}_{\mathrm{sl}}$ can be chosen nearer to resonance than for SrF. This leads to the fact that the power needed for the slowing laser $\mathcal{L}_{\mathrm{sl}}$ is less here. Additionally the excited state populations and therefore the deceleration force calculated are higher for CaF due to this fact.

The main advantage is the lower mass of CaF. We expect the molecular beam of CaF to be only slightly faster than a beam of SrF out of a buffer gas cell, so one really benefits of the lower mass when it comes to deceleration. The distance between source and trapping region is smaller and therefore the captured solid angle is larger. Another advantage is the smaller hyperfine structure of CaF, therefore the magnetic fields needed to reach the Paschen-Back regime are smaller.

A main advantage of SrF is that the needed laser wavelengths are available as diode laser systems with powers out of a tapered amplifier of up to 250 mW, where we expect to get 100 mW to the experimental apparatus after mode cleaning through a fiber and several optical elements. To have efficient deceleration we estimate that we need a power of approximately 400 mW for the frequency broadened lasers $\mathcal{L}_{\mathrm{rep}}$ in the experiment. Thus the solid state laser systems for SrF are not suitable for our experiment and therefore this advantage does not count in our case.

More power at the needed wavelengths is attainable through dye lasers (6W), fiber Raman amplifiers (2W) or through sum frequency generation. Since the physical arguments (mass, hyperfine structure) are in favor of CaF and the laser systems for the powers needed are of same complexity for CaF and SrF we finally decided for CaF in our future experiment.

4.5. Vibrational Repumping

While the main slowing is on the $X^2\Sigma_{1/2}, N = 1, \nu = 0 \rightarrow A^2\Pi_{1/2}, J' = 1/2, \nu' = 0$ transition, the vibrational repumping scheme can principally involve a different electronically excited state, if a decay through the first electronically excited state is forbidden. Figure 4.4 shows two possible vibrational repumping schemes. There are several arguments which favor scheme II, where $v = 1$ is repumped over the $B^2\Sigma_{1/2}$ state. The first is the higher number of excited states in such a repumping scheme therefore $a_{\max}$ is higher and the likelihood of decaying into coherent dark states is less probable. Another benefit of the $X^2\Sigma_{1/2} \rightarrow B^2\Sigma_{1/2}$ transition is that it is magnetically insensitive to the first order. Therefore one needs only one frequency broadened laser to repump over the whole Doppler range, which has to be broadened less than $\mathcal{L}_{\mathrm{rep}}$ on the $X^2\Sigma_{1/2}, N = 1, \nu = 0 \rightarrow A^2\Pi_{1/2}, J' = 1/2, \nu' = 0$ transition due to its magnetic insensitivity. Therefore the intensity per sideband can be higher in an experiment where only limited laser power is available.

There are also flaws in using the $B^2\Sigma$ state. First the transition needs π polarization to be driven effectively. This is not given in most Zeeman Slower designs, but a transverse magnetic field can be added and therefore this circumstance can be tackled relatively easily. The dipole matrix element d_{ij} is approximately the same for the $B^2\Sigma$ and the $A^2\Pi_{1/2}$ states when Franck-Condon factors are neglected. Still, the final transition element will be proportional to the Franck-Condon factor q_{ij}. Therefore the leakage into the first vibrational level given by $A^2\Pi_{1/2}, \nu' = 1 \rightarrow X^2\Sigma_{1/2}, N = 1, \nu = 0$ scales with the Franck-Condon factor

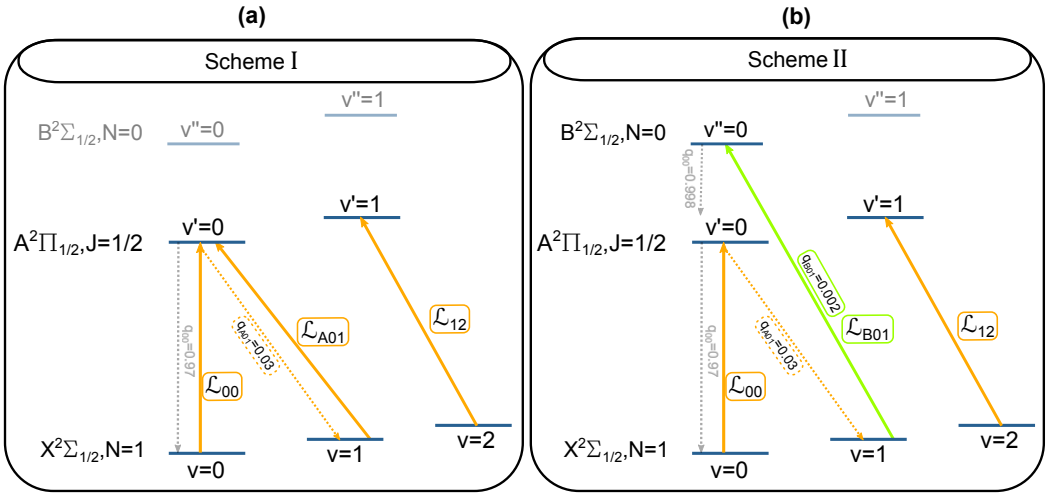

Figure 4.4.: Different vibrational repumping schemes on the example of CaF. For clarity only the Franck-Condon factors from $\nu = 0$ to $\nu = 1$ are shown.**(a)** Repumping over the A-state **(b)** Repumping over the B-state.

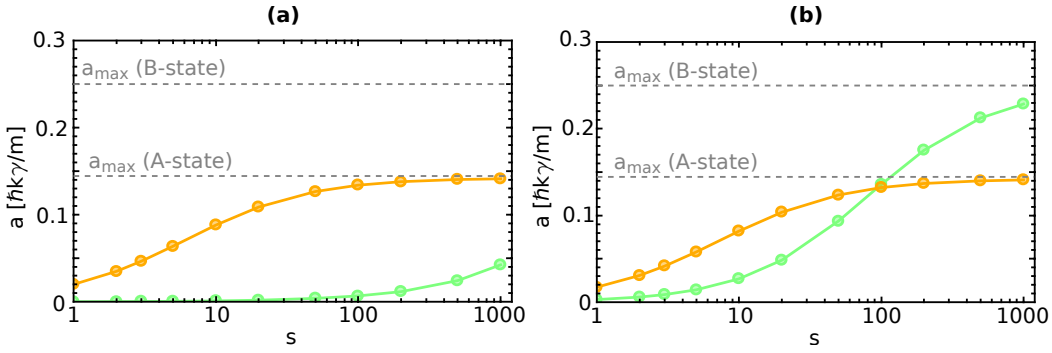

Figure 4.5.: Achieved deceleration a as a function of the saturation parameter s for repumping scheme I in orange and repumping scheme II in green.**(a)** In a longituidinal magnetic field where the lasers only drive $\sigma^{\pm}$ transitions. **(b)** In a transverse magnetic field where the lasers are orthogonally polarized to the magnetic field axis, such that they drive $\sigma^{\pm}$ and π transitions.

of $q_{A01} = 0.03$ for this transition. Whereas the dipole matrix element for the repumping transition scales with $q_{B01} = 0.002$, therefore the leakage rate into ν' is larger than the repumping rate by approximately $q_{A01}/q_{B01} = 10$ when both lasers are driven with the same saturation parameter. In this sense it is unfavorable for our Zeeman slowing scheme, that the Franck-Condon matrix of the $B^2\Sigma$ state is even more diagonal than the $A^2\Pi_{1/2}$ Franck-Condon matrix[3].

We simulate the vibrational repumping by applying rate equations to the whole level system up to $\nu = 2$ in the X-state at a magnetic field of $B = 400\,\mathrm{G}$. This leads to a (36+8) or (36+12) level system for the cases shown in Fig. 4.4**(a)** and **(b)** respectively. We define a saturation parameter $s = I/I_{\mathrm{sat}}$, where the saturation intensity is defined in a two level system as $I_{\mathrm{sat}} = \Gamma\hbar\omega^3/(12\pi c^2)$ this means that if the transition driven by laser $\mathcal{L}$ would be a closed two level cycling transition the excited state population would be $\rho_{ee} = 0.25$ at a saturation parameter of $s = 1$. The saturation intensity is $I_A \approx 4.9\,\mathrm{mW\,cm^{-2}}$ for the $A^2\Pi_{1/2}$ and $I_B \approx 5.5\,\mathrm{mW\,cm^{-2}}$ for the $B^2\Sigma_{1/2}$ state.

Figure 4.5 shows the achieved acceleration a in units of $\frac{\hbar k\Gamma}{m}$ which saturate at infinite laser power to $a_{\max}(\text{A-state}) = 1/7$ for repumping scheme I and to $a_{\max}(\text{B-state}) = 1/4$ for repumping scheme II. For the simulation shown here we hold the saturation parameter of the transition driven by $\mathcal{L}_{12}$ at $s_{12} = 10$ and plot the maximum of the achieved acceleration

[3]We thank Louis Baum and John Doyle for making us aware of this circumstance.

as a function of $s = s_{00} = s_{01}$. In **(a)** the situation is shown when the magnetic field lines are parallel to the propagation direction of the slowing laser light, leading to the circumstance that only $\sigma^{\pm}$-transitions are driven. Here repumping scheme II leads to nearly no acceleration since the $X^2\Sigma_{1/2}, N = 1, m_N = 0, \nu = 1 \rightarrow B^2\Sigma_{1/2}, N = 0, m_N = 0, \nu'' = 0$ transitions need π polarization to be driven. Therefore vibrational repumping scheme I is favorable here.

In **(b)** the situation is shown for a magnetic field which has an angle of 45 degree to the polarization vector of the slowing light. Therefore π transitions are effectively driven in this situation. Here scheme I leads to higher acceleration for low saturation due to the higher Franck-Condon factor, whereas for high saturation ($s > 100$) repumping scheme II would be favorable due to the higher number of excited states.

For the realizability in an experiment we assume 400 mW of total laser power and a Gaussian beam waist of 3 mm. When the laser is modulated to a width of $\Delta f = 1.1\,\mathrm{GHz}$ with a modulation frequency of $f_{\mathrm{mod}} = 6.6\,\mathrm{MHz}$, as it was assumed in the optical Bloch equation, the saturation parameter calculates to $s \approx 3.8$. So with experimental realizable parameters the repumping over the $A^2\Pi_{1/2}$ state leads to a higher deceleration and is therefore preferable for CaF.

4.6. Conclusions

In this chapter we proposed a novel Zeeman slowing scheme (type-II) capable of continuous deceleration and compression of the one dimensional velocity distribution of diatomic molecules. We simulated our scheme for $^{88}\mathrm{Sr}^{19}\mathrm{F}$ and $^{40}\mathrm{Ca}^{19}\mathrm{F}$ by numerically solving the optical Bloch equations and obtained force profiles which can be tuned to decelerate a desired velocity class by an external magnetic field. We thereby showed that the main feature of Zeeman slowing can be obtained in type-II level structures despite the lack of a magnetically tunable 2-level cycling transition.

The width of the calculated force profiles can be characterized by a FWHM of $\approx 80\,\mathrm{m\,s^{-1}}$. Although this is not as narrow as a typical force profile obtained in a traditional Zeeman slower of about $\approx 5 - 10\,\mathrm{m\,s^{-1}}$ we confirmed through Monte Carlo simulations that the obtained width of the slowed peaks can be as narrow as $2.5\,\mathrm{m\,s^{-1}}$ due to the fact that the slowing force quickly vanishes at the end of the Zeeman slower in the rapidly falling magnetic field [77, 78] ensuring a sharp cutoff of the slowing force.

Type II Zeeman slowing should be applicable to most of today's laser-coolable molecules with realistic experimental requirements, as long as $g_{\Pi} \ll g_{\Sigma}$. As $\mathcal{L}_{\mathrm{sl}}$ and $\mathcal{L}_{\mathrm{rep}}$ are both far detuned from resonance in low magnetic fields, the slowing scheme is ideally suited to be continuously coupled to already existing trapping schemes without disturbing already trapped molecules [79]. Because of the continuous nature of Zeeman slowing, it can ideally be combined with current pulsed molecular buffer gas sources for the realization of a quasi-continuous loading scheme by loading a whole sequence of pulses or with continuous sources of rovibrationally cold molecules instead of pulsed ones in future experiments. This will increase the flux of molecules even further, opening the possibility to realize large magneto-optical traps as an efficient starting point for work towards molecular Bose-Einstein condensates and quantum degenerate Fermi gases with exciting prospects for applications including precision measurements, ultracold chemistry and dipolar quantum many-body systems.

5

Demonstration Experiment on ^{39}K

In the following I will present a demonstration experiment of type-II Zeeman slowing on the D_1-line of atomic ^{39}K. To compare the scheme to conventional methods white-light slowing and a traditional type-I Zeeman slower have additionally been implemented in the same setup. I will first describe the scheme on the D_1-line in section 5.1 before I discuss the experimental apparatus which was set up during this thesis in section 5.2. The obtained results are then presented in section 5.3. Parts of this chapter have also been published elsewhere [63, 64]. The following chapter is to some extent identical to these publications.

5.1. Type-II Zeeman Slowing on the D_1-Line of ^{39}K

Figure 5.1 shows the level structure of the D_1-line in an external magnetic field. For magnetic fields leading to Zeeman shifts larger than the hyperfine splitting the system enters the Paschen-Back regime and the level structure is largely simplified. The ground and excited states each split into two manifolds with $m_J = \pm 1/2$. Neglecting hyperfine structure this can be seen as an effective 4-level system (see Fig. 5.1 **(a)**). One of the ground state manifolds is then coupled to an excited state manifold $|m_J = \pm 1/2\rangle \rightarrow |m_{J'} = \mp 1/2\rangle$ by a laser $\mathcal{L}_{\text{sl}}$ with $\sigma^{\mp}$ polarization. The corresponding transition frequency can be tuned by a magnetic field and can therefore be used to compensate a changing Doppler shift during the deceleration process in either an increasing (σ^-) or an decreasing (σ^+) field Zeeman slower configuration over the relation:

$$\delta_{\text{eff}} + (g_J \cdot m_J - g_{J'} \cdot m_{J'}) \cdot \mu_B \cdot B + k \cdot v = 0 \tag{5.1}$$

$$\delta_{\text{eff}} + \mu_{\text{eff}} \cdot B + k \cdot v = 0 \tag{5.2}$$

Here g_J and $g_{J'}$ are the g_J-factors in the Paschen-Back regime of the ground state $4^2S_{1/2}$ and the excited state $4^2P_{1/2}$ respectively. As the transition between these manifolds is not closed the atom will quickly fall into the ground state manifold, which is not adressed by $\mathcal{L}_{\text{sl}}$. Additionally this non coupled manifold exhibits a different Zeeman shift and therefore cannot be pumped back by the application of a simple sideband. Still a frequency broadened laser $\mathcal{L}_{\text{rep}}$ (see Fig. 5.1**(a)** and **(c)**) can be applied covering all relevant velocity classes for the applied magnetic fields to pump the atoms from the dark manifold back to the one addressed by $\mathcal{L}_{\text{sl}}$. The scheme is therefore equivalent to the molecular scheme described in the previous chapter 4. The difference is that $\mathcal{L}_{\text{sl}}$ and $\mathcal{L}_{\text{rep}}$ couple to different excited states

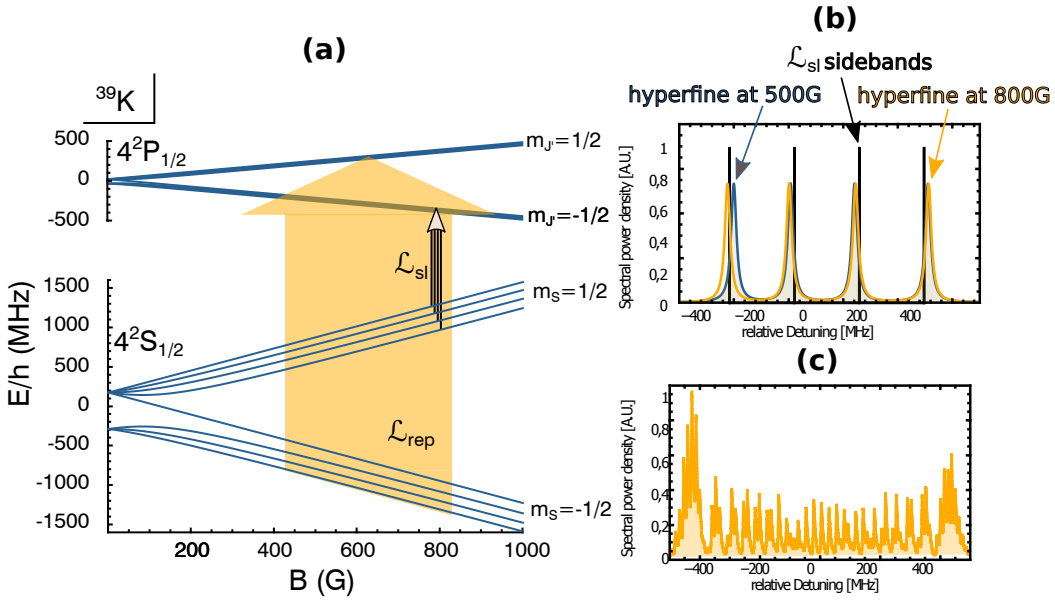

Figure 5.1.: **(a)** Type-II Zeeman Slower scheme for ^{39}K. The effective detuning δ_{eff} of $\mathcal{L}_{\text{sl}}$ together with the applied magnetic field B dictates which velocity class is addressed (see relation 5.2). **(b)** Sideband spectrum of the slowing Laser (black) to address the transition frequencies for the different hyperfine levels in high magnetic fields.**(c)** Spectrum of the frequency broadened repumping laser realized with a current modulated DFB Diode. Sinusoidal modulation with $f_{\text{mod}} = 12\,\text{MHz}$ modulated to a width of approximately 900 MHz.

in the case of ^{39}K whereas they couple to the same electronic states in the molecular case. Therefore the scheme on ^{39}K is less vulnerable to coherent dark states.

At the beginning of the slowing process all atoms are quickly pumped into the ground state manifold addressed by $\mathcal{L}_{\text{sl}}$. They stay in this state until the magnetic field reaches a magnitude that shifts the level, at a given velocity of the atom, into resonance with $\mathcal{L}_{\text{sl}}$. The slowing force itself is then exerted by subsequent scattering of photons by $\mathcal{L}_{\text{sl}}$ and $\mathcal{L}_{\text{rep}}$ with equal amount. Note however, that the resonance condition for the whole system is still governed by $\mathcal{L}_{\text{sl}}$ so that the system acts similar to a traditional type-I Zeeman slower. At the end of the slowing process the atoms are again pumped by $\mathcal{L}_{\text{rep}}$ into the manifold formerly addressed by $\mathcal{L}_{\text{sl}}$.

To take the finite hyperfine structure of ^{39}K in the ground and the excited state into account, $\mathcal{L}_{\text{sl}}$ needs 4 sidebands to couple each hyperfine state m_I to the corresponding hyperfine level in the excited state (see Fig. 5.1 **(b)**). Note that for every specific hyperfine state m_I on its own, there are 4 velocity classes resonant with $\mathcal{L}_{\text{sl}}$ due to its 4 sideband structure. However, mixing between different m_I states is still significant at the magnetic fields we work at, so that the 4 sidebands do not result in four distinct slowing peaks in our velocity distribution.

5.2. Experimental Apparatus

In our experiments, we realize a type-II Zeeman slower for atomic potassium based on the apparatus sketched in Fig. 5.2. The atomic beam is created in an oven which is heated to 190°C, Fig. 5.2**(a)**. The atoms leave the oven through a 3 mm skimmer and enter the 130 cm long Zeeman slowing region. Here the atoms interact with the counter-propagating slowing light generated by a self-built diode laser system. The spatially varying Zeeman

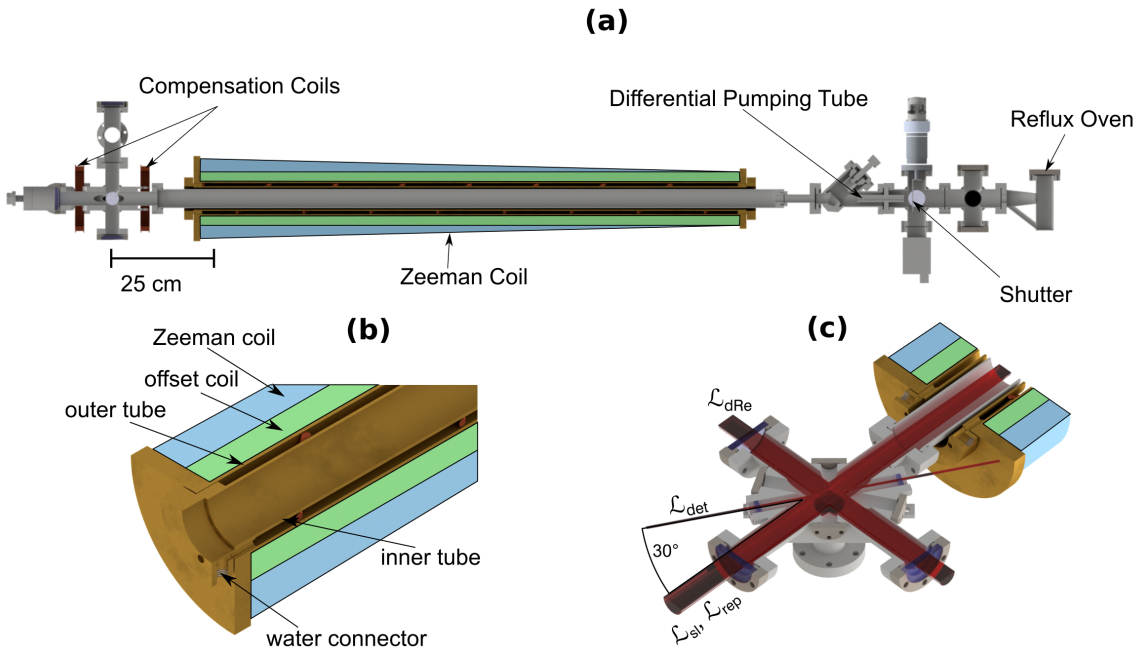

Figure 5.2.: **(a)** Half section view of the vacuum chamber showing the overall geometry of the apparatus. **(b)** Quarter section view of the magnetic field coil. Between the inner and the outer tube of the brass holder cooling water is flushed, which holds the coil at a temperature of $T < 70°\mathrm{C}$. **(c)** Detection chamber showing the slowing and detection lasers. For the fluorescence measurement the lens and curved mirror are additionally installed in this chamber (not shown here).

field is produced by two independent coils with winding patterns optimized by a search algorithm. Finally, the slowed atoms reach the detection region 25 cm behind the end of the slowing region. Here, the longitudinal atomic velocity after the slowing process is analyzed via Doppler spectroscopy.

5.2.1. Magnetic Field

In our experiment we decided for an increasing field Zeeman slower for which the ideal magnetic field is given by

$$B(z) = B_0 + \Delta B \cdot (1 - \sqrt{1 - z/L_0}) \text{ for } 0 < z < z_{\text{fin}} \tag{5.3}$$

Here B_0 denotes the offset field, which in the case for type-II Zeeman slowing is large enough to bring the particles in the Paschen-Back regime. L_0 is the length of the slowing field needed to slow down the atoms from the capture velocity v_{cap} to a standstill given by

$$L_0 = m\frac{v_{\text{cap}}^2}{\eta\hbar k\Gamma} \tag{5.4}$$

where m is the mass of the particle, Γ is the spontaneous decay rate of the excited state and $\eta = \frac{a}{a_{\max}}$ is the so called design parameter, which dictates with how much of the maximum attainable deceleration $a_{\max} = \frac{\hbar k\Gamma}{2m}$ the slower is operated. The ideal field for a deceleration to a specific final velocity v_{fin} stops at

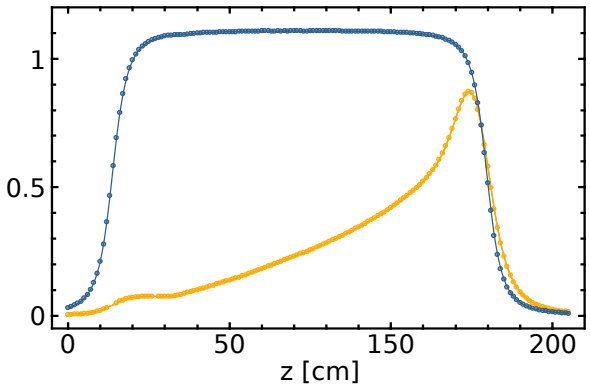

Figure 5.3.: Measured magnetic field values (points) together with the calculated magnetic field (lines) for the offset coil in blue and for the tapered Zeeman coil in orange. The current applied to the coils of 10 mA for this measurement comes from a laser diode current driver. With such a low current we can use the available hall probe measuring magnetic fields up to $B_{\max} = 2\,\mathrm{G}$.

$$z_{\mathrm{fin}} = m\frac{v_{\mathrm{cap}}^2 - v_{\mathrm{fin}}^2}{\eta\hbar k\Gamma} \tag{5.5}$$

Together with the effective detuning of the slowing laser sidebands δ_{eff} it dictates the capture velocity of the Zeeman slower due to the relation $\mu_{\mathrm{eff}} \cdot B_0 + k \cdot v_{\mathrm{cap}} = -\delta_{\mathrm{eff}}$. The final velocity is given by the magnetic field at the end of the slowing region $B(z_{\mathrm{fin}})$, through $\mu_{\mathrm{eff}} \cdot B(z_{\mathrm{fin}}) + k \cdot v_{\mathrm{fin}} = -\delta_{\mathrm{eff}}$.

In our experiments the solenoid producing the Zeeman field consists of two independent coils. The inner offset coil in Fig. 5.2**(b)** (green) produces a homogeneous magnetic field over the entire slower length serving as an offset field to access the Paschen-Back regime. The second coil produces a typical increasing field Zeeman slower field (blue). We measure the magnetic field produced by the Zeeman slower coils with a hall probe. Since the hall probe is only able to measure magnetic fields up to $B_{max} = 2\,\mathrm{G}$ we use a laser diode driver from Thorlabs to apply a constant current of $I = 10\,\mathrm{mA}$ to the coil. The hall probe measures the magnetic field along the symmetry axis of the solenoid. The measured data can be seen in Fig. 5.3 along with the calculated profile. The sum of the two fields gives a good approximation of the ideal magnetic field and the separation of coils gives us the capability to tune the capture velocity v_{cap} and the final velocity v_{fin} independently.

During the experiment the solenoid dissipates a power of approximately 850 W and therefore needs to be water-cooled over its entire length. Thus it consists of two coaxial brass tubes, which are stacked into each other and are sealed to each other on both sides, see also Fig. 5.2**(b)**). Through a water connector we flush cooling water through the whole brass holder. During the experiment the coil reaches a temperature of 60°C on the surface and 70°C on the estimated hottest point in between the windings, where a temperature sensor was placed during the construction. The wire is rated up to a temperature of 200°C, so even higher fields are possible with this design.

5.2.2. Laser Systems

During this thesis a few laser systems have been built to realize the experiment for different beam slowing techniques. In this section a short overview is given. We work with external cavity diode laser systems. The external cavity is built in a so called cat-eye configuration and we use a interference filter as a wavelength selective element. The design is adopted from

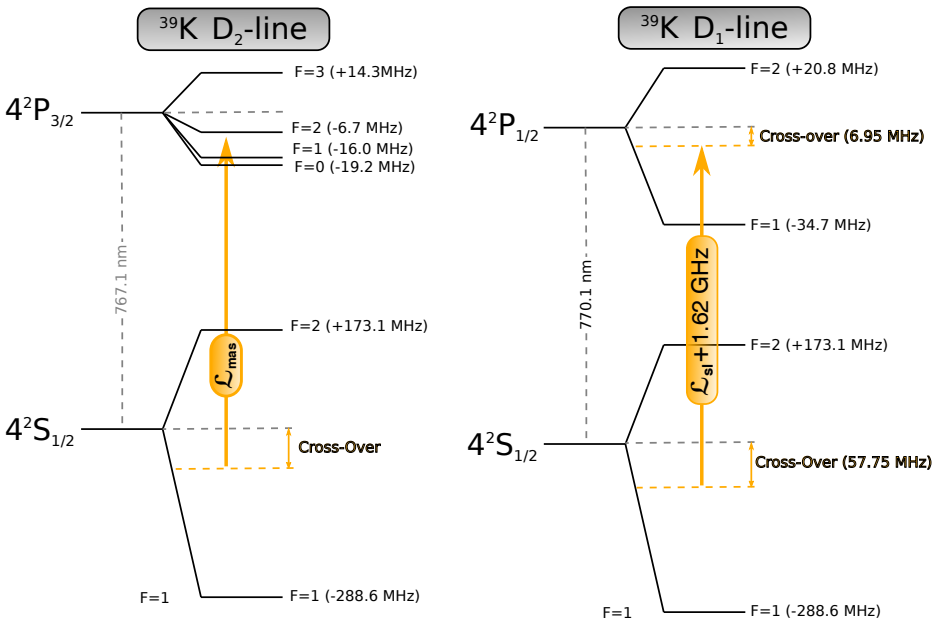

Figure 5.4.: Level structure of the D_1- and D_2-line of ^{39}K. The hyperfine structure of the $4^2P_{3/2}$ excited state on the D_2-line is not resolved. Therefore the locking point of $\mathcal{L}_{\text{mas}}$ is not exactly known. This is different for the hyperfine structure of the $4^2P_{1/2}$ state, which is resolved and here we can give the exact position of our locking point.

[80]. The lasers typically have output powers of $P_{laser} \approx 60\,\text{mW}$. Wavelength adjustment can be accomplished by fine tuning of the temperature, the angle of the interference filter, the external cavity length and the current applied to the laser diode, details can be found in [80]. For most of our experiments we have two laser systems addressing the D_2-line of ^{39}K for detection purposes and two laser systems addressing the D_1-line for slowing purposes. Figure 5.4 shows the level structure of the D_1- and D_2-line of ^{39}K together with the locking points of $\mathcal{L}_{\text{sl}}$ and $\mathcal{L}_{\text{mas}}$.

D_1-Line Laser Systems

An external cavity diode laser system (ECDL) is used as $\mathcal{L}_{\text{sl}}$ (see Fig. 5.5**(a)**) to couple the $4^2S_{1/2}|m_J = 1/2\rangle$ ground state sublevels to the $4^2P_{1/2}|m_J = -1/2\rangle$ excited state sublevels with light polarized to drive σ^--transitions. The system was built during a masters thesis [82] and subsequently upgraded. $\mathcal{L}_{\text{sl}}$ is locked via modulation-transfer-spectroscopy 1618 MHz to the red of the D_1-line-crossover in a ^{39}K spectroscopy cell. The light is amplified by a tapered amplifier and afterwards passes through a double-pass acousto-optic modulator system (AOM) to create the 4 sidebands needed to address the 4 hyperfine levels $m_I = -3/2, ..., +3/2$. The AOM is driven at a frequency of 118.6 MHz and we combine the m=+2,+1,0,-1 orders with a 50:50 beam splitter, as we need all frequencies with the same polarization for the later combination with $\mathcal{L}_{\text{rep}}$. $\mathcal{L}_{\text{sl}}$ is coupled into a polarization-maintaining single-mode fiber to clean the beam profile.

The setup for $\mathcal{L}_{\text{rep}}$ was implemented during a master thesis [83] and consists of a tapered amplifier, seeded with a current modulated DFB diode to frequency broaden the light (see Fig. 5.5**(b)**). For the shown measurements the diode is modulated sinusoidally with a modulation frequency $f_{mod} = 12\,\text{MHz}$ to a width of $\Delta f \approx 1.6\,\text{GHz}$. In Fig. 5.1**(c)** the frequency spectrum of $\mathcal{L}_{\text{rep}}$ is shown recorded by a cavity with a free spectral range of 1 GHz when modulated to a width of $\Delta f \approx 900\,\text{MHz}$. The spatial transverse beam profile is cleaned by coupling through a polarization-maintaining single-mode fiber.

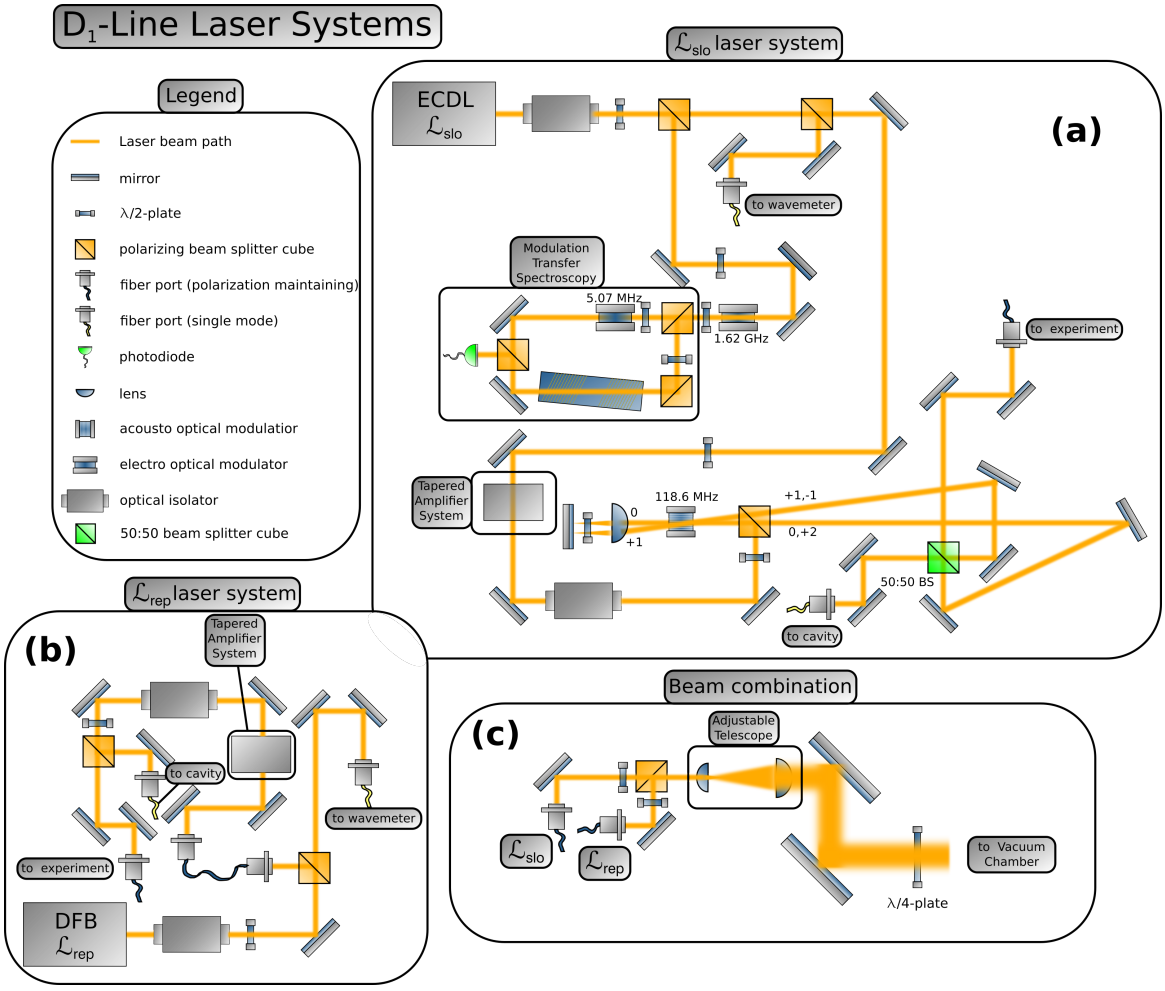

Figure 5.5.: **(a)**Slowing laser $\mathcal{L}_{slo}$ setup locked via modulation transfer spectroscopy on a potassium spectroscopy cell. For the type-II Zeeman slower the laser is locked 1618 MHz red of the D_1-line crossover transition, whereas for the type-I Zeeman slower it is locked 809 MHz red of the D_2-line crossover transition. The light is amplified through a tapered amplifier setup before being supplied to the experiment through a polarization maintaining single mode fiber. **(b)** Repump $\mathcal{L}_{rep}$ setup used for type-II Zeeman slowing and for white-light slowing. A frequency modulated free running DFB diode is seeded into a tapered amplifier setup and then supplied to the experiment through a polarization maintaining single mode fiber. The graphical representation of the laser systems is inspired by [81].

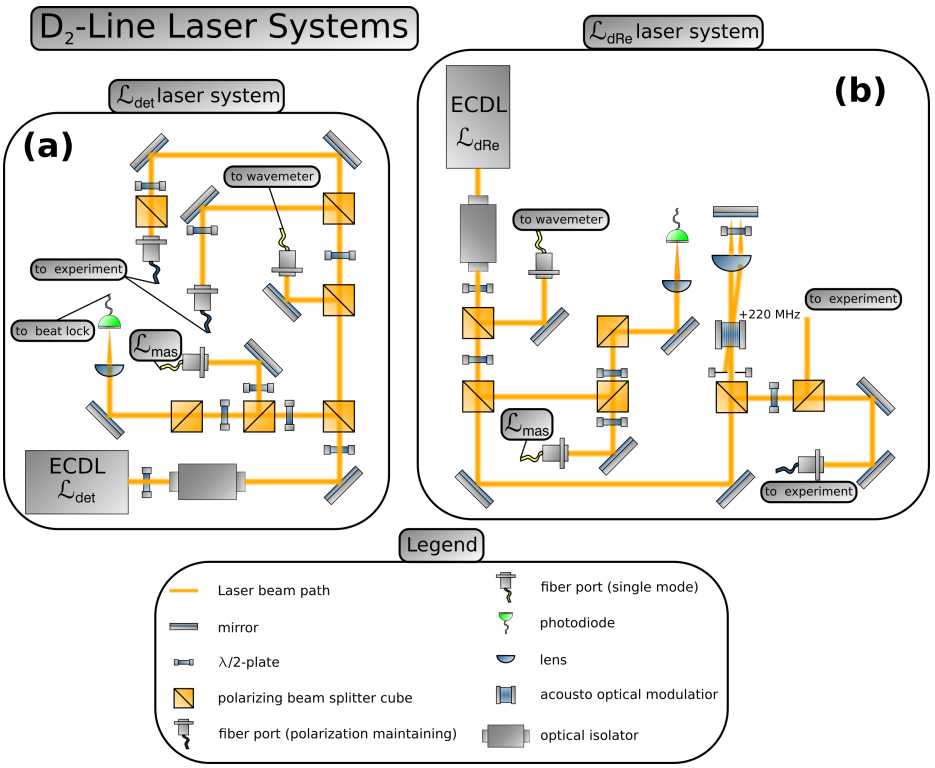

Figure 5.6.: **(a)** Diagram of the detection laser setup on the D_2-line. The laser is frequency locked by a beat measurement to a master laser. Two polarization maintaining optical fibers are used to bring the light to the experiment. One for the transverse and one for the longitudinal velocity detection. **(b)** Repump laser setup for the detection on the D_2-line. The laser is frequency locked to a master laser and an optical fiber brings the light to the detection region. Another beam path is used to supply light to the oven region where the atomic beam can optionally be pumped into a specific hyperfine state.

After combining $\mathcal{L}_{\text{sl}}$ and $\mathcal{L}_{\text{rep}}$ with a polarizing beam splitter we use a quarter-wave plate to circularly polarize the lasers (see Fig. 5.5**(c)**). We end up with a power of $P_{\text{rep}} = 400\,\text{mW}$ in total and $P_{\text{sl}} \approx 20\,\text{mW}$ in each order. The beams have a Gaussian beam waist of $w_0 = 1\,\text{cm}$ at the vacuum viewport and are slightly focused by an adjustable telescope towards the oven region.

D_2-Line Laser Systems

For our D_2-line laser systems we had the opportunity to use a master laser $\mathcal{L}_{\text{mas}}$ from the neighboring laboratory [80] locked via frequency modulation spectroscopy onto the crossover of the D_2-line. Due to the linewidth of the D_2-line of $\approx 6\,\text{MHz}$ the hyperfine structure of the excited $4^2P_{3/2}$-state is not resolved. The detection laser $\mathcal{L}_{det}$ is overlayed with $\mathcal{L}_{\text{mas}}$ and the beat note on a photodiode is measured, such that $\mathcal{L}_{det}$ is offset locked to $\mathcal{L}_{mas}$. The beat frequency can be scanned between 70 MHz and 1 4 GHz. We scan the laser in a triangular shape with a frequency of 10 Hz. The system is depicted in Fig. 5.6**(a)**. A second laser system $\mathcal{L}_{dRe}$ on the D_2-line was built, which is also offset locked on $\mathcal{L}_{\text{mas}}$ (see Fig. 5.6**(b)**). A double pass AOM driven at $f_{\text{AOM}} = 220\,\text{MHz}$ is used to create a sideband such that both hyperfine ground states can be addressed.

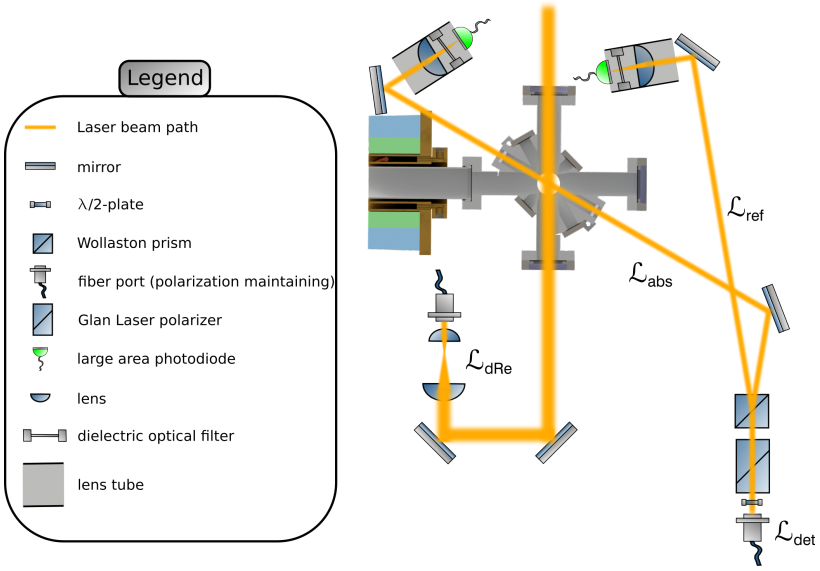

Figure 5.7.: Detection beam path.

5.2.3. Velocity Measurement

We detect the velocity distribution of the atoms via Doppler-spectroscopy. The detection laser intersects the atomic beam with an angle of 30° and we measure the absorption. Since $\mathcal{L}_{\text{det}}$ has a relative intensity noise of 10^{-2} and the absorption signal is in the 10^{-4} range we use a differential absorption scheme.

Figure 5.7 shows the detection chamber together with the beam lines of the detection system, for simplicity the slowing lasers are not shown. For the differential measurement $\mathcal{L}_{\text{det}}$ is split into two beams $\mathcal{L}_{\text{abs}}$, which crosses the atomic beam and records the signal, and $\mathcal{L}_{\text{ref}}$, which does not interact with the atomic beam and is used for noise cancellation. We undertook some effort to optimize the noise cancellation through the differential measurement, where common noise is effectively canceled, but differential noise will be amplified afterwards together with the atomic signal.

The biggest contribution of differential noise in the first measurements was polarization rotation in front of the polarization dependent beam splitter, therefore we clean the polarization directly in front of the beam splitting by a Glan-Laser polarizer with extinction ratio of 100000:1. The beam is then split by a Wollaston prism, which has nearly no etalon effects, which results in a differential signal when the laser is scanned in frequency. In comparison conventional polarizing beam splitters or 50:50 beam splitters lead to much higher levels of differential noise due to larger etalon effects when the laser is scanned. After the splitting , there are three contributions to the differential noise, namely, vibration, room light and etalon effects due to different optical devices in the respective beam paths. During implementation it was taken care that the beam paths of $\mathcal{L}_{\text{abs}}$ and $\mathcal{L}_{\text{ref}}$ have the same length, this reduces vibration noise on the photodiodes. The photodiodes have large area detectors, on which we focus the beams to further reduce vibration noise. The photodiodes are enclosed in lens tubes, blocking room light and stray light from other laser sources. Between the focusing lenses and the photodiodes an optical dielectric filter with center frequency of $\lambda_{\text{center}} = 770\,\text{nm}$ is installed to further reduce noise from room light sources.

The largest etalon effects were determined to result from the vacuum viewports and the dielectric filters. We tried to mount the filters at an angle in the beam path by using angled

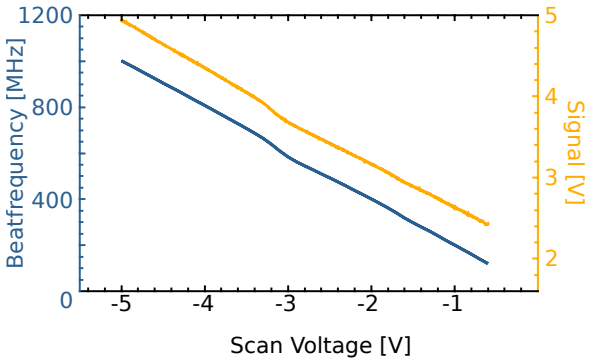

Figure 5.8.: In orange the differential signal is shown when the laser is scanned and the atomic beam is blocked by the in vacuum shutter. The residual signal results from etalon effects of the vacuum viewports leading to a frequency dependent transmission. In blue the beat frequency used for the locking circuit is shown. We always record this background signal before taking a velocity measurement and subtract it afterwards.

lens tube mounts[1]. But we ended up to install the filters between the lens and the photodiode with which we found to have the least signals from etalon effects.

Figure 5.8 shows the signal with the atomic beam blocked by the vacuum shutter when the laser is scanned from a beat frequency of about 70 MHz to 1 GHz by applying a linear voltage ramp to the locking circuit. The signal (orange) is governed by etalon effects in this regime and the curve shows the same behavior as the frequency-to-voltage curve we recorded with a spectrum analyzer (blue). The amplitude of the etalon signal is on the same order of magnitude as the absorption signal of the atomic beam. Still we find the etalon signal to be highly repeatable if $\mathcal{L}_{\text{det}}$ stays single mode along the whole scanning range. If $\mathcal{L}_{\text{det}}$ has regions in this frequency space where it gets slightly multi-mode these different frequency components are transmitted differently through the optical beam paths and heavily disturb the signal in a non repeatable way.

$\mathcal{L}_{\text{det}}$ is an ECDL, which is scanned by adjusting the cavity length with a mirror glued on a piezo crystal. Whereas the current of the photodiode and the interference filter, which acts as a wavelength selective element, are not scanned. Therefore the mode hop free tuning range is only in the few GHz range, not much larger than our typical scanning range. To increase the mode hop free tuning range we installed a current feed forward into the locking circuit of $\mathcal{L}_{\text{det}}$ and thereby increased the mode hop free tuning range from a few GHz to over 10 GHz. Afterwards we were able to record consistent data by first measuring the background signal, when the atomic beam is blocked by the in vacuum shutter, and subtracting it afterwards from the recorded signal where the atomic beam is present.

As we measure the atoms from the ground state level $4^2S_{1/2}|F=2\rangle$ to the excited state $4P_{3/2}$, where we do not resolve the hyperfine structure, we add a repumper $\mathcal{L}_{\text{dRe}}$ addressing the $4^2S_{1/2}|F=1\rangle \rightarrow 4P_{3/2}$ transition perpendicular to the atomic beam to pump the atoms into the detection state. In the first measurements we pumped the atoms into the detection state by adding a sideband blue detuned by 440 MHz with an acousto-optic modulator system to $\mathcal{L}_{\text{det}}$. However for ^{39}K the hyperfine structure in the ground state of 461 MHz corresponds to a Doppler shifted velocity of $v_{dopp}(461\,\text{MHz}) \approx 354\,\text{m}\,\text{s}^{-1}$. This is of the same magnitude as the width and peak position of the longitudinal velocity distribution of our oven. When slowing is applied this leads to multiple peak structures separated by this $354\,\text{m}\,\text{s}^{-1}$ complicating the interpretation of the measurements. Additionally the height of the peaks is dependent on the position of $\mathcal{L}_{\text{rep}}$ used for slowing. Here $\mathcal{L}_{\text{rep}}$ pumps atoms at certain velocity classes into the $4^2S_{1/2}|F=2\rangle$ state where the blue sideband of $\mathcal{L}_{\text{det}}$ can be absorbed driving again the the $4^2S_{1/2}|F=2\rangle \rightarrow 4P_{3/2}$ transition. This leads to further

[1] Thorlabs SM1L03T

artifacts in the measured absorption signal complicating the interpretations even more. The repumping with the non Doppler sensitive $\mathcal{L}_{\mathrm{dRe}}$ perpendicular to the atomic beam effectively circumvents these complications.

We determine the velocity axis by first measuring the absorption signal at an angle of 90° to the atomic beam, the peak position f_0 gives us the beat frequency which corresponds to $0\,\mathrm{m\,s^{-1}}$. The scaling of the axis is then given by the measured beat frequency f the detection angle α_{det} of $\mathcal{L}_{\mathrm{det}}$ and the corresponding Doppler shift $\delta_{\mathrm{dopp}} = \lambda^{-1} \approx 1.3\,\frac{\mathrm{MHz}}{\mathrm{m\,s^{-1}}}$.

$$v = \frac{f - f_0}{\cos(\alpha_{\mathrm{det}})\delta_{\mathrm{dopp}}} \tag{5.6}$$

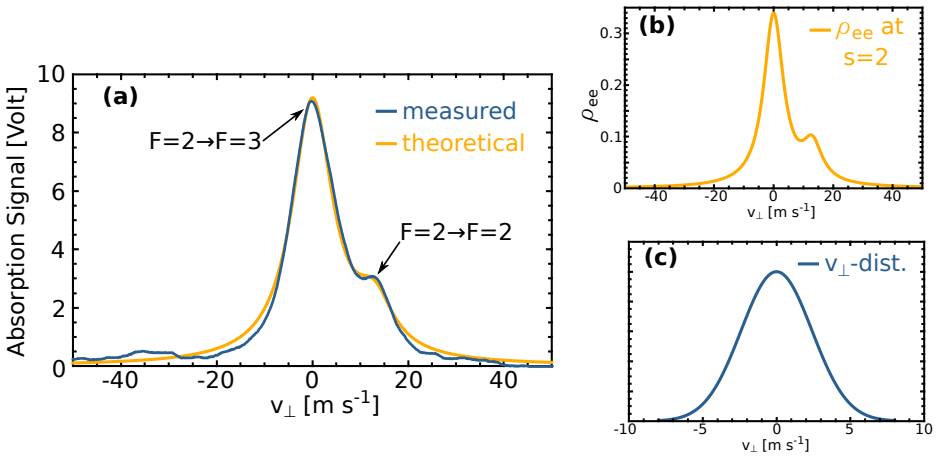

Figure 5.9.: **(a)** Measured transverse absorption of a scanning $\mathcal{L}_{\mathrm{det}}$ used to determine the origin of the velocity axis for the longitudinal measurement. The horizontal axis shows the transverse velocity corresponding to the measured beat frequency. The shoulder on the right flank is due to the hyperfine structure of the excited state. **(b)** Expected spectrum of the observed transitions for a saturation parameter of $s = 2$. The plot shows the excited state population ρ_{ee}. **(c)** Transverse velocity distribution $v_\perp$ of the atomic beam at the detection position resulting from a three dimensional Monte Carlo simulation taking into account the geometry of our apparatus. A convolution of **(b)** with **(c)** results in the theoretical curve in **(a)** in orange.

5.2.4. Velocity Resolution

The most fundamental limitation of our velocity resolution is the natural linewidth of the D_2-line of $\Gamma \approx 6\,\mathrm{MHz}$ corresponding to $\delta v \approx 4\,\mathrm{m\,s^{-1}}$. Figure 5.9**(a)** show the measured transverse absorption spectrum of the atomic beam in blue. As it can be seen the hyperfine structure of the excited state is not well resolved leading to a double peak structure corresponding to the $4S_{1/2}\,|F = 2\rangle \to 4P_{3/2}\,|F = 3\rangle$ and $4S_{1/2}\,|F = 2\rangle \to 4P_{3/2}\,|F = 2\rangle$ transition separated by 21 MHz corresponding to $16.1\,\mathrm{m\,s^{-1}}$ in the transverse measurement. For the differential absorption measurement the detection laser has a power of $P_{\mathrm{det}} = 230\,\mu\mathrm{W}$ and a top-hat transverse intensity profile with $d = 3\,\mathrm{mm}$ corresponding to a saturation parameter of $s = 2$. Figure 5.9**(a)** shows the expected velocity resolution function at the given saturation parameter.

Another factor leading to a decreased velocity resolution is the transverse velocity distribution of the beam. Figure 5.9**(b)** shows the simulated transverse velocity distribution at the detection position resulting from a Monte Carlo simulation taking into account the geometry of our apparatus. The standard deviation of this distribution is $2.4\mathrm{m\,s^{-1}}$ and limits our resolution further. We can calculate the expected resolution for a transverse beam measurement

if we convolute the resolution function resulting from the natural linewidth and the upper hyperfine structure 5.9**(a)** with the transverse velocity distribution 5.9**(b)**. In Fig. 5.9**(c)** the obtained result is shown in orange together with the transverse absorption measurement in blue. The predictions fit very well to the measurement and we therefore conclude that we understood the contributions from the different broadening mechanisms. Therefore we can deduce the resolution in a longitudinal velocity measurement with a detection angle $\alpha_{\mathrm{det}} = 30°$, which broadens the resolution function resulting from the linewidth and the upper hyperfine structure by the factor $1/\cos(\alpha_{\mathrm{det}})$. The contribution of the transverse velocity becomes narrower by the factor $\sin(\alpha_{\mathrm{det}})$, since the projection of the transverse velocity distribution on the axis of the detection laser becomes smaller by that factor. Note that the distance between the two peaks stays the same regardless of the angle and only the widths are multiplied by the given factors. We use this calculated resolution to convolute our Monte Carlo simulations for a comparison with the experimental data.

5.2.5. Compensation Coils

The outer diameter of the Zeeman slower coil at the end of the slowing region is about 130 mm and therefore the magnetic field is falling off relatively slowly. At the highest Zeeman fields used we expect a field of $B_{det} = 18.6\,\mathrm{G}$ with $\frac{\partial B_{det}}{\partial z} = 1.97\,\mathrm{G\,cm^{-1}}$ at the detection region. Figure 5.10 shows the transverse absorption spectrum without (blue) and with (orange) the solenoid on. We use two compensation coils installed around the detection region and calculate the currents needed to pull the magnetic field to $B = 0\,\mathrm{G}$ and the magnetic field gradient to $\frac{dB}{dz} = 0\,\mathrm{G\,cm^{-1}}$. The result is shown in Fig. 5.10 in green, showing efficient cancellation of the residual magnetic fields.

For a longitudinal measurement $\mathcal{L}_{\mathrm{det}}$ crosses the chamber at an angle and therefore traverses regions where the magnetic field compensation might not be perfect. Still, from our code we used to calculate the magnetic field coils for our Zeeman slower we estimate that the magnetic field does not change by more than 1 G throughout the detection region and conclude that the velocity resolution of our detection is not additionally broadened by residual magnetic fields.

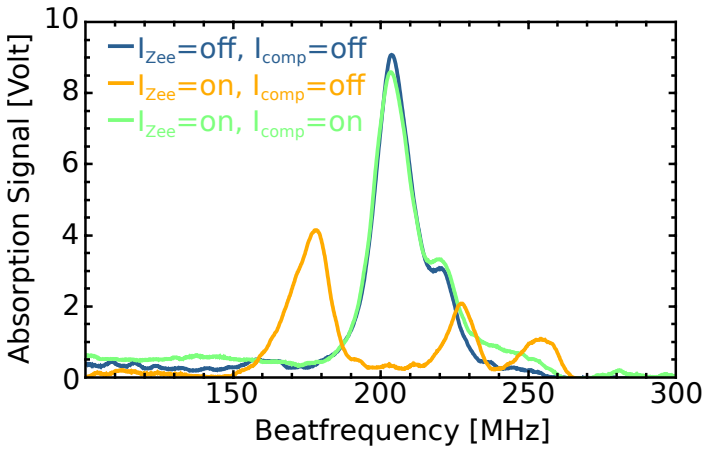

Figure 5.10.: In blue the transverse absorption as a function of beat frequency is shown when no magnetic fields are applied. The orange curve shows the result, when the magnetic field used for Zeeman deceleration is applied, leading to residual magnetic fields in the detection region, which splits the line due to the Zeeman effect. In green the signal can be seen, when the compensation coils around the detection region are additionally applied, showing that residual magnetic fields are efficiently canceled.

5.3. Results

Figure 5.11 shows the measured velocity distributions after Zeeman slowing for different magnetic field profiles. First, we measured the initial velocity distribution (black curve) with no slowing lasers applied. We use the height of the initial distribution peaking at approximately $514\,\mathrm{m\,s^{-1}}$ to normalize our signals. We then switch on the slowing lasers to allow for radiative slowing. The orange graph was recorded with only the offset field on (see the inset in Fig. 5.11**(a)** for the corresponding magnetic fields). Here the atoms are slowed down from $400\,\mathrm{m\,s^{-1}}$ to approximately $350\,\mathrm{m\,s^{-1}}$ at which point the atoms are slowed down so far that $\mathcal{L}_{\mathrm{sl}}$ is not resonant anymore. The subsequent graphs show, that by adding a Zeeman field ΔB this peak can be shifted downwards to lower velocities. The blue graph shows the distribution when slowed to a final peak velocity of $v_{\mathrm{p}} = 35\,\mathrm{m\,s^{-1}}$. In **(b)** the corresponding Monte-Carlo simulations are shown, which resemble the measurement to a high degree, concerning the position of the slowed peaks as well as their magnitude.

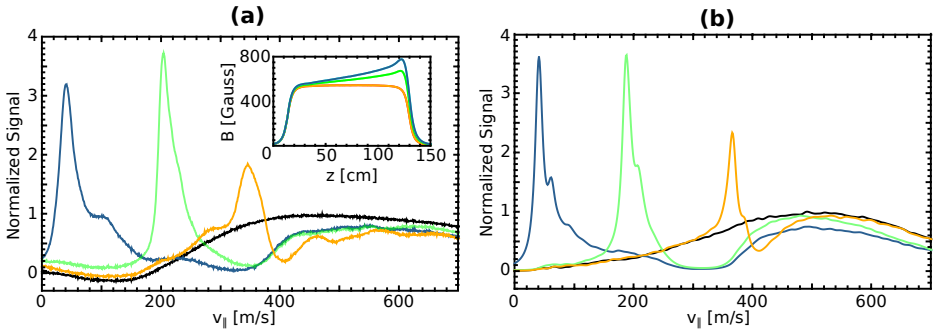

Figure 5.11.: **(a)** Differential absorption signals for type-II Zeeman slowing for several final velocities. The inset shows the corresponding configurations of the applied magnetic field.**(b)** Three dimensional Monte Carlo simulations, see methods for details.

In a next step, we optimize the performance of the Zeeman slower by tuning the capture velocity. In Fig. 5.12 **(a)** we keep the maximum magnetic field constant and alter the magnetic field magnitude at the entrance of the slower. For a small capture velocity only a few atoms are swept from higher velocities down to $v_{\mathrm{p}} = 40\,\mathrm{m\,s^{-1}}$. If we decrease the magnitude at the entrance of the slower further, we can increase the flux at low velocities by capturing more atoms.

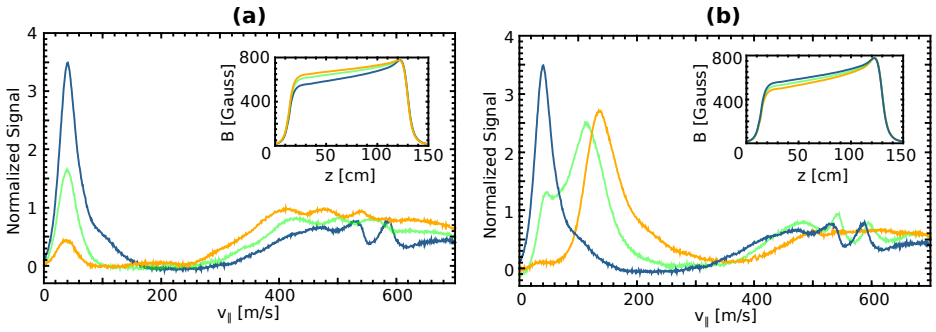

Figure 5.12.: **(a)** Type ll Zeeman slowing with different capture velocities. By addressing higher velocity classes while keeping the final velocity constant the slowing performance can be optimized. **(b)** In blue the optimized signal is shown alongside with the corresponding magnetic field for our Type ll Zeeman slower. The green and orange lines show the results, when the capture velocity is increased even further with capture velocities too high to be slowed over the finite slowing path. The atoms fall out of resonance with $\mathcal{L}_{\mathrm{sl}}$ before reaching their final velocity.

Our slowing performance is limited by the deceleration $a = \eta a_{\max}$ we achieve with the limited repump power in our experiment. This can be seen when increasing the capture velocity even further. The system then reaches a point where the atoms cannot follow the changing resonance condition dictated by the magnetic field gradient anymore (see Fig. 5.12**(b)**). Then they fall out of resonance with $\mathcal{L}_{\text{sl}}$ before reaching v_{fin}. The green measurement shows a double peak structure, resulting from the fact that the achieved deceleration that $\mathcal{L}_{\text{rep}}$ can provide is different for particles on-axis versus off-axis due to its gaussian beam profile. On axis, where the intensity is highest, the slowing still takes place and the atoms are slowed down to $v_{\text{fin}} = 40\,\text{m}\,\text{s}^{-1}$ but in the wings of the profile the intensity is not sufficient and they fall out of resonance with $\mathcal{L}_{\text{sl}}$ at higher velocities. We checked this interpretation by placing an iris in front of the entrance vacuum view port of the slowing and repumping laser. By cutting the wings of $\mathcal{L}_{\text{sl}}$ and $\mathcal{L}_{\text{rep}}$ the peak at higher velocities disappears and only the peak at $v_{\text{fin}} = 40\,\text{m}\,\text{s}^{-1}$ was left. We see the same behaviour in our Monte-Carlo simulations (not shown here).

In our measurements, we find the type-II Zeeman slower system to work reliably with results easily reproduced on a daily basis. When optimizing the system we found some parameters to be of importance, especially the beam overlap between $\mathcal{L}_{\text{rep}}$ and $\mathcal{L}_{\text{sl}}$ is crucial. Slightly focusing the lasers throughout the slowing region on the oven nozzle is beneficial due to a small transverse confinement force, but the gain is quite moderate. While the power of $\mathcal{L}_{\text{rep}}$ is the limiting factor in our experiment the exact modulation frequency seems to be quite unimportant. We get our best slowing performance for sinusoidal modulation with $f_{\text{mod}} = 12\,\text{MHz}$. We additionally tested modulation frequencies ranging from $f_{\text{mod}} = 6 - 24\,\text{MHz}$ as well as other modulation schemes like sawtooth and triangular modulation, which altered the frequency spectrum significantly but changed the slowing result by only 20 to 30 %.

Overall we attained a flux of $\Phi_{\text{II}} = 3.3 \cdot 10^9\,\text{cm}^{-2}\text{s}^{-1}$ under $35\,\text{m}\,\text{s}^{-1}$ for an oven temperature of $T_{\text{oven}} = 190°C$. Due to the available repump power limiting our slowing performance, we reach a fraction of $\eta = \frac{a}{a_{\max}} = 0.38$ of the maximum attainable deceleration $a_{\max}$.

5.4. Comparison to Conventional Slowing Methods

5.4.1. Type-I Zeeman Slower

First, we compare to the slowing result of a traditional type-I Zeeman slower working on the D_2-line of ^{39}K. These are a standard beam slowing method used to load magneto-optical traps for alkali or alkaline earth atoms and can therefore be seen as a benchmark for our type-II Zeeman slower. The maximum achievable radiation pressure on the D_2-line ($\lambda = 766.7\,\text{nm}, \tau = 26.37\,\text{ns}$) is approximately the same as on the D_1-line ($\lambda = 770.1\,\text{nm}, \tau = 26.72\,\text{ns}$) and the comparison gives a good hint, if the velocity selectivity and the distribution of the force along the slowing path for our type-II Zeeman slower is as favorable as in the type-I case. To our best knowledge this is the first time a Zeeman slower is implemented on the D_2-line of ^{39}K.

To realize a type-I Zeeman slower in our setup, we lock $\mathcal{L}_{\text{sl}}$ 809 MHz red of the D_2-line crossover. The light is polarized to drive σ^--transitions so that the slowing takes place on the closed $4^2S_{1/2}, |F = 2, m_F = -2\rangle \rightarrow 4^2P_{3/2}, |F = 3, m_F = -3\rangle$ transition as shown in the inset of Fig. 5.13. No sidebands for $\mathcal{L}_{\text{sl}}$ and no repumper is needed in type-I Zeeman slowing. We get the best slowing result for the type-I Zeeman slower, when no offset field $B_{\text{offset}} = 0\,\text{G}$ is applied, as shown in the inset of Fig. 5.13. The magnetic field is generated by the shaped magnetic field coil resulting in an increasing field Zeeman slower starting with $B = 0\,\text{G}$ and ending at about $B = 375\,\text{G}$ at the end of the slowing region.

Figure 5.13 **(a)** shows the slowing result we achieved in our experiment. The capture velocity lies at $v_{\text{cap}} \approx 500\,\text{m}\,\text{s}^{-1}$ and the final peak velocity at $v_p \approx 35\,\text{m}\,\text{s}^{-1}$. Between these

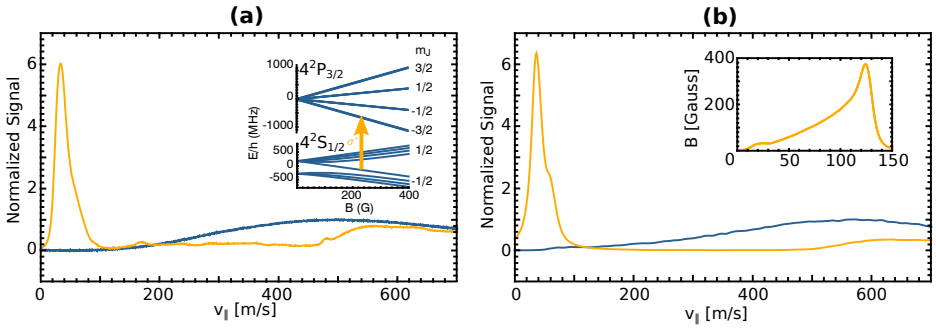

Figure 5.13.: **(a)** Differential absorption signal of type-I Zeeman Slowing in a σ^--configuration (see inset). **(b)** Corresponding Monte Carlo simulation. The inset shows the applied magnetic field. We do not use an offset field for the type-I slower.

two velocities there is nearly no atom signal showing the efficient deceleration over the whole velocity range. In Fig. 5.13 **(b)** the corresponding Monte Carlo simulation is shown, again exhibiting a good agreement with the experimental results.

We find that the type-I slower is more dependent on exact beam alignment and focusing conditions of the slowing beams than in the type-II case. A focus near the nozzle of the oven leads to high intensities, where the resulting power broadening of the transition is large enough to cover the whole Doppler range of the longitudinal velocity distribution [84]. As a result all atoms are pumped into the stretched slowing state. In contrast to this, in type-II Zeeman slowing all ground state sublevels are coupled, so that there is no need for optical pumping into a desired state.

Although it has been noted elsewhere [85, 86] that the small hyperfine splitting in the excited state could lead to loss from the slowing process, we do not find this to be a problem.

We also tried out a different configuration where an offset field of about $B_{\text{offset}} \approx 675\,\text{G}$ is applied and the Zeeman field magnitude ΔB is kept the same. We locked the laser 1618 MHz red to the D_2-line crossover. Here the slowing result is about a factor of 1.5 worse than without an offset field although ΔB and the corresponding v_{cap} and v_{fin} are kept the same. This can be explained by the fact, that for the configuration with $B_{\text{offset}} = 0\,\text{G}$ the slowing laser $\mathcal{L}_{\text{sl}}$ is already resonant for atoms traveling near v_{cap} in the 50 cm long oven region and therefore cuts deeper in the longitudinal velocity distribution sweeping more velocity classes in the slowing process. This is also seen in the Monte Carlo simulations, which predict the same differences in achieved flux below $v_{\parallel} = 35\,\text{m}\,\text{s}^{-1}$ for the different configurations.

We measure a flux of atoms with velocities slower than $35\,\text{m}\,\text{s}^{-1}$ of $\Phi_{\text{I}} = 5.5 \cdot 10^9\,\text{cm}^{-2}\text{s}^{-1}$. This is a factor of 1.66 larger than the flux measured in the type-II Zeeman slower scheme. The better performance arises from the higher capture velocity of about $500\,\text{m}\,\text{s}^{-1}$ instead of $350\,\text{m}\,\text{s}^{-1}$ in the type-II case, the latter being limited by more demanding laser power requirements.Furthermore, the type-I slower effectively starts slowing in the oven region, where for the case of the type-II slower the actual slowing starts not until the field reaches B_0 inside the solenoid similar to the type-I slower where a magnetic offset field is applied.

5.4.2. White-Light Slowing

In a next step, we compare type-II Zeeman slowing to white-light slowing, which is an established method for radiative slowing of a molecular beam [39, 46]. In our setup, frequency broadened laser light is provided by $\mathcal{L}_{\text{rep}}$, this time detuned to the red side of the potassium resonance. We modulate with a sinusoidal frequency of $f_{\text{mod}} = 12\,\text{MHz}$ to an approximate width of $\Delta\omega \approx 900\,\text{MHz}$ corresponding to a velocity range of $\Delta v \approx 400\,\text{m}\,\text{s}^{-1}$.

The laser is linearly polarized and we find the best slowing result, when a magnetic field of $B_0 = 11\,\text{G}$ is applied throughout the slowing region. We suppose this to be due to enhanced destabilization of coherent dark states on the D_1-line in a magnetic field [38]. The final

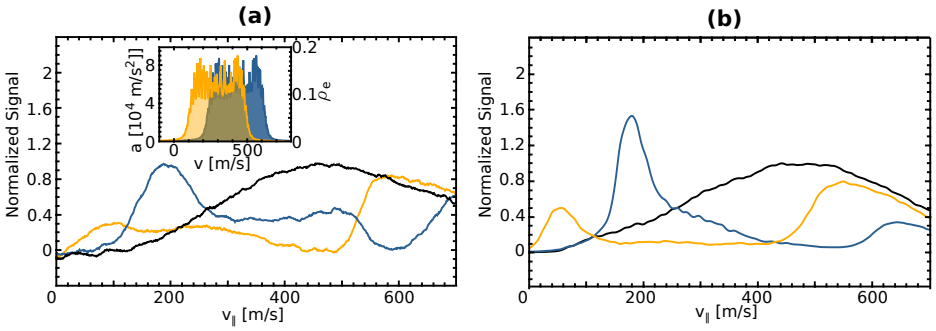

Figure 5.14.: **(a)** Achieved white-light slowing signals for different v_{fin}. The inset shows the corresponding force profiles calculated with multilevel rate equations. **(b)** Corresponding Monte Carlo simulation.

velocity distribution of the atoms after slowing is measured by detecting the fluorescence induced by $\mathcal{L}_{\mathrm{det}}$. Although the resulting signals are usually noisier and need more time to average than the differential absorption it was used here because of two reasons. First, the white-light slowing lasers are close to resonance in the detection region and pump the atoms into the $4^2S_{1/2}, |F = 1\rangle$ state. We therefore would need a high power repumper $\mathcal{L}_{\mathrm{dRe}}$ to pump the atoms back into the $4^2S_{1/2}, |F = 2\rangle$ detection state over the whole region where $\mathcal{L}_{\mathrm{det}}$ crosses the atomic beam. Because the fluorescence optics only collects light from a small volume in the middle of the chamber, the power of $\mathcal{L}_{\mathrm{dRe}} \approx 20\,\mathrm{mW}$ is sufficient to pump the atoms back here. The second reason is background potassium gas, which we see more in the absorption pictures than in the fluorescence pictures, as the absorption laser crosses the whole chamber. This effect is of no importance for the Zeeman slowing data as the slowing peaks are much higher, but for the small signals at low velocities in white-light slowing it heavily disturbs the slowing result.

Figure 5.14**(a)** shows the measured velocity distributions. For the different measurements we kept the modulation of the slowing laser constant and altered the offset detuning resulting in different final velocities. The initial velocity distribution is shown as the black curve. For the blue graph we see a deceleration from approximately $600\,\mathrm{m\,s^{-1}}$ down to $200\,\mathrm{m\,s^{-1}}$. The slowing laser cuts a deep hole into the velocity distribution and increases the density at $200\,\mathrm{m\,s^{-1}}$ significantly. If we detune the slowing laser to be resonant with lower velocity classes, the capture velocity and the final velocity shift accordingly (orange curve). The density at lower velocities still increases in comparison to the unslowed distribution but the efficiency is rapidly decreasing. This behavior is seen in many publications regarding white-light slowing for atoms [87] and molecules [39, 40, 46].

In Fig. 5.14**(b)** the corresponding Monte Carlo simulations are shown and the inset of Fig. 5.14**(a)** shows the calculated deceleration force used for the simulation. The force is calculated by multilevel rate equations, taking into account the frequency spectrum of the slowing laser and the hyperfine structure of the D_1-line. The simulations show good agreement with the measured distributions concerning the capture and the final velocity. Also the peak at very slow velocities is small compared to the Zeeman slowing cases as the efficiency of the slowing to low velocity classes rapidly decreases. Still the results from the simulation suggest a slightly better slowing result as was measured. In the simulation nearly no atoms are lost between the capture and the final velocity (see the orange curve in Fig. 5.14**(b)**). Presumably due to a smaller force in the experiment than the rate equation model suggests. In fact we measure the best slowing result with a small magnetic offset field applied supposedly due to remixing of coherent dark states. This effect is not taken into account in the rate equation model and could explain the lower force and therefore the loss at higher velocities in the experiment. A more realistic force profile could be obtained by solving the optical Bloch equations for the whole system.

In white-light slowing all atoms reach their final velocity at a different point in space. Therefore the time the atoms spend in the slowing region is not minimized as in type-I

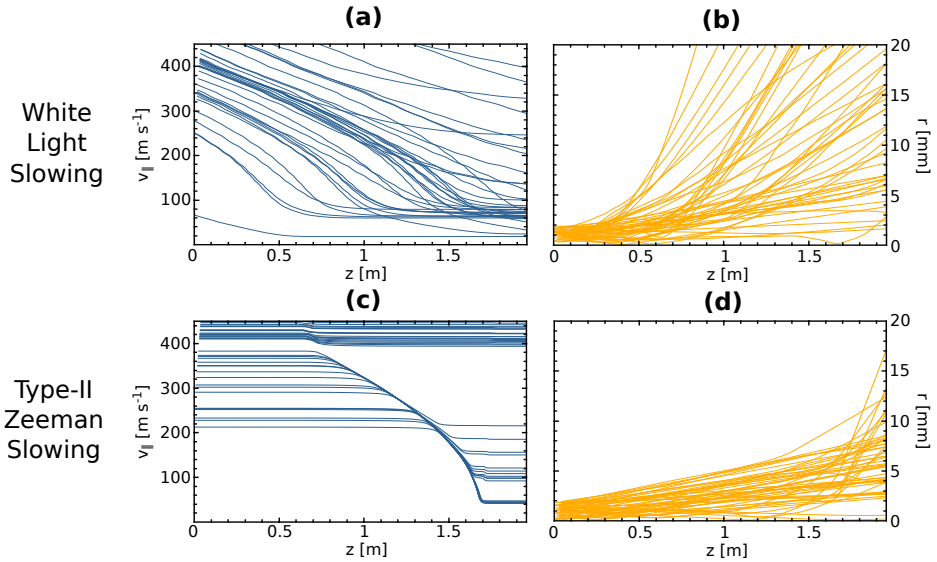

Figure 5.15.: Trajectories obtained from three dimensional Monte Carlo simulations of the slowing process. Each graph shows trajectories of 50 ^{39}K atoms randomly chosen from the initial velocity distribution. The first row show the results of the white-light slowing simulation. In **(a)** the velocity as a function of slowing distance is plotted, whereas in **(b)** the distance r to the slowing axis z is plotted. In **(c)** and **(d)** the corresponding graphs for type-II Zeeman slowing are shown.

or type-II Zeeman slowing and the transverse spread leads to high losses until the slowed velocity class finally reaches the detection region. Figure 5.15 shows the trajectories of slowed particles obtained from the Monte Carlo simulations of the slowing process. 5.15**(a)** shows the velocity as a function of slowing distance. It can be seen that a significant number of atoms is slowed to velocities under $100\,\mathrm{m\,s^{-1}}$. But as the atoms reach their final velocities at different points in space the divergence of the beam increases considerably, as can be seen in Fig. 5.15**(b)**. For a comparison the results of the simulation for type-II Zeeman slowing are shown in Fig. 5.15**(c)** and **(d)**, where the transverse spread is efficiently minimized as the atoms travel at their initial velocities up to the point where $\mathcal{L}_{\mathrm{sl}}$ is shifted into resonance.

The second effect is, that the slowing force has no sharp cutoff at low velocities. The relatively broad cutoff results from the finite hyperfine structure of the excited state and the power broadening of the slowing transition. Additionally the frequency spectrum of the slowing laser as seen in Fig. 5.1**(c)** has no sharp cutoff at high frequencies. Atoms which have already reached the desired end velocity will still be decelerated while flying to the detection region, leading to spreading of the slowed velocity peak. This effect gets stronger the slower the atoms are. For very low velocities this can even lead to deceleration under $0\,\mathrm{m\,s^{-1}}$ where the atoms obviously never reach the detection region. Our white-light slowing result is limited by the power of the frequency broadened slowing laser of 400 mW.

In the white-light slowing case the laser does not have to be as broad in frequency ($\Delta f \approx 900\,\mathrm{MHz}$) as the repump laser for the type-II Zeeman slowing case ($\Delta f \approx 1.6\,\mathrm{GHz}$). This is because the laser only has to cover the lower hyperfine structure of 460 MHz and additionally the changing Doppler shift. Therefore the spectral power density is higher and the slowing cuts deeper inside the longitudinal velocity distribution as the type-II Zeeman slower, having a higher capture velocity of about $v_{\mathrm{cap}} = 500\,\mathrm{m\,s^{-1}}$. Still this benefit does not result in higher fluxes at low velocities.

The flux of atoms below $35\,\mathrm{m\,s^{-1}}$ achieved is $\Phi_{\mathrm{w}} = 1.5 \cdot 10^8\,\mathrm{cm^{-2}s^{-1}}$ about a factor of 20 less than for the type-II Zeeman slower and correspondingly a factor of 33 lower than for the type-I slower. Another disadvantage is the near resonant light of the slowing laser in the detection region, which can disturb a following magneto-optical trap [51].

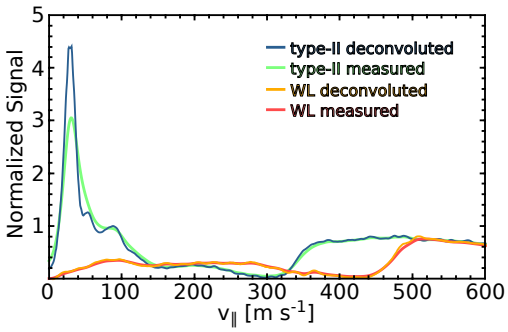

Figure 5.16.: Measured velocity distribution for type-II Zeeman slowing and white-light slowing when deconvoluted with the expected velocity resolution.

5.5. Longitudinal Temperature of the Slowed Particles

The measured peaks at slow velocities in type-II and type-I Zeeman slowing have a full width at half maximum of $\sigma_{\mathrm{II}} = 36\,\mathrm{m\,s^{-1}}$ and $\sigma_{\mathrm{I}} = 32\,\mathrm{m\,s^{-1}}$ respectively, whereas the Monte-Carlo simulations predict somewhat narrower peaks.

In principle we can deconvolute our measured data by the expected velocity resolution derived in 5.2.4. By doing so we get the data shown in figure 5.16. From this we conclude that the FWHM of the slowed peak is $\sigma_{\mathrm{II}} = 18\,\mathrm{m\,s^{-1}}$ for the type-II Zeeman slower corresponding to a longitudinal temperature of $T_{\parallel} \approx 270\,\mathrm{mK}$. The same procedure yields for the type-I Zeeman slower $T_{\parallel} \approx 200\,\mathrm{mK}$. Whereas for the white-light-slowing no temperature can be given as there is no distinct slowed peak.

Concerning the flux the measured signal at velocities $v_{\parallel} < 35\,\mathrm{m\,s^{-1}}$ in white-light slowing might to some part be only due to the finite velocity resolution. Comparing the deconvoluted data we expect the factor in flux between white-light slowing and type-II Zeeman slowing to be $\Phi_{\mathrm{II}}/\Phi_{\mathrm{w}} = 25$ This is slightly larger than deduced directly from the measurement. The same procedure yields for the comparison between type-II and type-I Zeeman slowing a factor of $\Phi_{\mathrm{I}}/\Phi_{\mathrm{II}} = 1.7$.

Summing up the deconvolution of our data gives us a better hint on the achieved longitudinal temperature in type-II and type-I Zeeman slowing. Concerning the comparison of the fluxes between the different methods the deconvolution does not alter the results considerably.

5.6. Discussion

We have demonstrated and compared three different beam slowing techniques. Two of these, white-light slowing and type-II Zeeman slowing, are implementable for laser coolable molecules. As the magnitude of the slowing force for all three cases is on the same order we understood the observed differences to be the result of the efficiency with which this force is applied. Comparison of the experimental data with Monte Carlo simulations supported this idea.

We found type-II Zeeman slowing to have the same continuous velocity compression characteristics as type-I Zeeman slowing. In both schemes we achieve a well defined final velocity with a width corresponding to a longitudinal temperature of $T_{\parallel} \approx 270\,\mathrm{mK}$ for the type-II and $T_{\parallel} \approx 200\,\mathrm{mK}$ for the type-I slower. The performance of the type-II Zeeman slower is experimentally limited by the laser power of the frequency broadened repumper $\mathcal{L}_{\mathrm{rep}}$. For the white-light slowing case the losses through transverse spreading are larger due to the unfavorable application of the slowing force. Furthermore the slowing force has no sharp

cutoff and the slowed atoms are spread out over a broad velocity range. Compared to chirped light slowing, which was not implemented during this work and which is also applicable for laser coolable molecules, we expect the type-II Zeeman slowing to be advantageous due to its continuous nature. The phase space acceptance of chirped light slowing is rather small and only parts of the comparatively long temporal pulse widths out of buffer gas sources can be slowed down. Furthermore, particles reaching their final velocity determined by the end frequency of the chirp are spread out in space. Those disadvantages are partly compensated for by more relaxed power requirements allowing for larger slowing beam diameters in the experiment. The full potential of type-II Zeeman slowing in comparison to chirped light might be unfolded in future molecular experiments by continuous cold beam sources.

6

Design and Construction of a Buffer Gas Beam Source

The starting point of experiments aiming at direct laser cooling of molecules is typically a buffer gas beam source. In such a device the molecules of interest are pre-cooled translationally and rotationally by a buffer gas at cryogenic temperatures and a molecular beam is formed.

Cryogenic buffer gas beam sources (CBGB) are commonly used in laboratories nowadays and produce high fluxes of slow and cold molecules. The technique was pioneered in the Harvard group of John Doyle [88] and later adopted by the Tarbutt group in London [89] and the Rempe group in Munich [90, 91]. The technique has seen a rapid development in the last years and there are several methods to introduce the species of interest into the buffer gas, all of them having their own experimental challenges. Here we focus on ablation loaded CBGB's which are used to produce beams of molecular radicals, especially earth alkaline halides.

Figure 6.1 **(a)** depicts a sketch of a laser ablation loaded CBGB. The cell is cooled to cryogenic temperatures around 4 K and cold helium is added through a fill line. A pulsed laser is focused on a solid precursor target that is mounted inside of the cell and comprises the molecules of interest. The rapid deposition of heat into a small region on the target by the laser pulse leads to laser ablation and a pulse of evaporated particles is injected into the helium flow. The molecules of interest are cooled by the buffer gas internally and translationally and then leave the cell through an aperture in the front facet.

The produced molecular beams have forward velocities ranging from $v_{\parallel} \approx 100 - 200\,\mathrm{m\,s^{-1}}$ for one stage buffer gas sources and $v_{\parallel} \approx 35 - 100\,\mathrm{m\,s^{-1}}$ for two stage buffer gas sources [17]. Furthermore, they produce cold molecules with macroscopic population in the low lying rotational states. Figure 6.1 **(b)** shows the population in the lowest rotational states for $^{40}Ca^{19}F$ for several temperatures in the cryogenic regime. The emitted molecular pulse will serve as the starting point for radiation pressure slowing which will be applied from the electronic ground state with rotational quantum number $N = 1$ as it was explained in chapter 2. This illustrates that not only the moderate forward velocities are beneficial as a source for experiments aiming for cooling and trapping of molecules but also the macroscopic population in the rotational state with $N = 1$ for these pre-cooled molecules.

Our Approach

To acquire knowledge about laser ablation loaded buffer gas beam sources in our group we used an approach outlined as follows. We first build a buffer gas cell whose design is inspired by previously published work [87]. We try to understand the behavior and simulate the system to validate our interpretations. We then want to use the knowledge we gained to design an improved geometry.

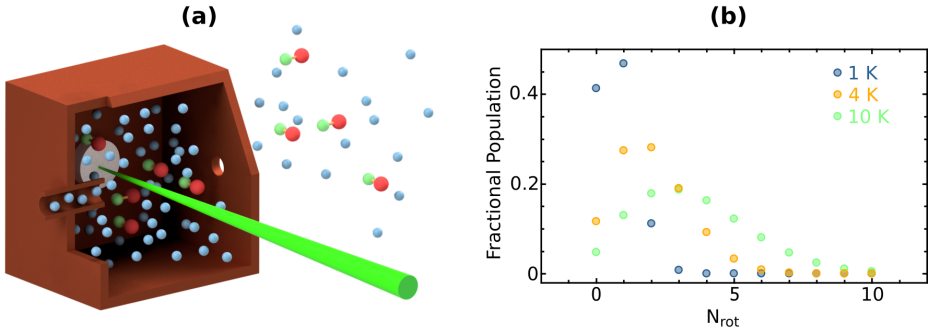

Figure 6.1.: **(a)** Injection of the molecules of interest into the cold ^{4}He via laser ablation. The molecules have an initial temperature of $T \approx 10^4\,\mathrm{K}$ and thermalize in the first several $\mu\mathrm{s} - \mathrm{ms}$ to the temperature of the buffer gas. The beam is formed by drilling a hole in one of the walls of the chamber, through which the particles exit the cell. **(b)** Rotational state population of $^{40}\mathrm{Ca}^{19}\mathrm{F}$ at different temperatures. The distributions show the importance of pre-cooling to cryogenic temperatures to produce internally cold molecules as only molecules with $N_{\mathrm{rot}} = 1$ are addressed by the cooling lasers.

This Thesis

In the first section I will summarize the basic principle and the main physical processes at play in a laser ablation loaded CBGB leading to the production of a cold molecular beam.

In the following section I revisit the theoretical framework behind the helium flow in a CBGB by introducing the one-dimensional fluid flow model [18] and motivate the choice in favor of this hydrodynamic description.

The third section describes the simulations which I carried out using the computational fluid dynamics (CFD) software OpenFOAM [92] giving further inside in the ^{4}He flow field.

Lastly I describe the design and construction of the experimental apparatus containing the CBGB.

6.1. Basic Properties of CBGB's

The main physical processes apparent in a CBGB are first the ablation of molecules into the cold ^{4}He flow, second the thermalization of the initially hot ablated material, third the extraction of the molecules through the aperture of the cell and finally the remaining beam formation process after the molecules have passed the aperture. These different processes are detailed in the following subsections.

6.1.1. Molecule Production via Laser Ablation

Laser coolable molecules are typically radicals with an unpaired valence electron not participating in the binding of the molecule. Due to this free electron these molecules are highly chemically reactive and have a short lifetime if not well isolated from the environment. Hence they are not readily available in a gas bottle.

Depending on the particle of interest, simple sublimation of the solid is sufficient, for example in the ablation of atoms from their solid counterparts. This is different when during the ablation molecular bounds have to be broken , as it is the case in the ablation of $^{88}\mathrm{Sr}^{19}\mathrm{F}_2$, $^{40}\mathrm{Ca}^{19}\mathrm{F}_2$ and $^{89}\mathrm{Y}_2^{16}\mathrm{O}_3$ targets to produce $^{88}\mathrm{Sr}^{19}\mathrm{F}$, $^{40}\mathrm{Ca}^{19}\mathrm{F}$ and $^{89}\mathrm{Y}^{16}\mathrm{O}$ respectively. Here higher ablation energies are needed to generate a plasma on the target surface where the molecular bonds can be broken to produce the radicals of interest. The ejected particles are typically at a temperature of about $T_{\mathrm{abl}} = 10^4\,\mathrm{K}$.

6.1.2. Thermalization and Mean Free Path

The first cooling of the initial hot particles with temperature T_0 takes place through collisions with the cold ^{4}He gas present in the cell volume at temperature T_{He}. Neglecting all internal energy contributions the translational temperature T_N of particles with mass m_{a} after a certain number of collisions N with ^{4}He is given by [93]

$$T_N = (T_0 - T_{\mathrm{He}})\mathrm{exp}(-\frac{N}{\kappa}) + T_{\mathrm{He}}, \tag{6.1}$$

where $\kappa = \frac{(m_{\mathrm{a}}+m_{\mathrm{He}})^2}{2m_{\mathrm{a}}m_{\mathrm{He}}}$ is the number of collisions needed to diminish the temperature difference by 1/e, for ^{39}K this characteristic number is $\kappa_{\mathrm{K}} \approx 6$. To get a feeling for the order of magnitude, we want to mention that in our later experiments T_0 of the ablated ^{39}K is estimated to be $6 \cdot 10^4$ K. This means that here about $N \approx 80$ collisions are needed to arrive at a temperature within a few percentage of the buffer gas temperature. The numbers are similar for the ablation of other species.

The mean free path λ of a particle of species a inside ^{4}He buffer gas is given by [94]:

$$\lambda_{\mathrm{a}} = \frac{1}{n_{\mathrm{a}}\sigma_{\text{a-He}}\frac{\sqrt{\overline{v}_{\mathrm{a}}^2+\overline{v}_{\mathrm{He}}^2}}{v_{\mathrm{a}}}}, \tag{6.2}$$

where $\overline{v}_{\mathrm{a}}$ and $\overline{v}_{\mathrm{He}}$ are the mean velocities of species a and He respectively. For a thermalized mixture where $\frac{1}{2}m_{\mathrm{He}}\overline{v}_{\mathrm{He}}^2 = \frac{1}{2}m_{\mathrm{a}}\overline{v}_{\mathrm{a}}^2$ this can be rewritten in

$$\lambda_{\mathrm{a}} = \frac{1}{n_{\mathrm{a}}\sigma_{\text{a-He}}\sqrt{1+\frac{m_{\mathrm{a}}}{m_{\mathrm{He}}}}}. \tag{6.3}$$

When discussing the mean free path of a pure mixture, as in the buffer gas for ^{4}He, we get the well known formula:

$$\lambda_{\mathrm{He}} = \frac{1}{n_{\mathrm{He}}\sigma_{\text{He-He}}\sqrt{2}} \tag{6.4}$$

Note that therefore the mean free path of the particles a changes during the thermalization process. At typical buffer gas densities of $n_{\mathrm{He}} \approx 10^{15} - 10^{17}\,\mathrm{cm}^{-3}$ and a collision cross section of $\sigma_{\text{a-He}} \approx 10^{-14}\,\mathrm{cm}^{-2}$ the mean free path is about $\lambda \approx 7 - 700\,\mu\mathrm{m}$ leading to thermalization lengths with an upper limit $d < N\lambda$ ranging from $1 - 100\,\mathrm{mm}$. Thus cell dimensions of a few cm are sufficient to thermalize the particles.

6.1.3. Extraction from the CBGB

The process leading to extraction of the thermalized particles is advection in the bulk motion of the ^{4}He buffer gas. The particles will be entrained into the ^{4}He flow field and eventually leave the cell through the aperture together with ^{4}He. The other main process is diffusion. If diffusion is the dominant process, most particles will diffuse to the cold cell walls were they will condense and will be lost for the later experiments. If advective entrainment is the governing process a large fraction of the particles can leave the cell and form the molecular beam. This advective process is often called hydrodynamic enhancement. Section 7.1.2 and 7.1.4 go into more detail about the entrainment process.

6.1.4. Beam Formation: Effusive vs. Hydrodynamic

Considering a volume filled with a gas at thermal equilibrium, the particles inside the cell volume obey the velocity distribution:

$$p(\vec{v}) = \left(\frac{m}{2\pi k_\mathrm{B} T}\right)^{\frac{3}{2}} e^{\frac{-m|\vec{v}|^2}{2k_\mathrm{B}T}}. \tag{6.5}$$

If the pressure outside of the cell volume is considerably lower, a molecular beam can be formed by drilling a hole with diameter d_ap into one of the walls as shown in Fig. 6.1 **(a)**. When the mean free path of the particles λ is larger than d_ap the particles will leave the cell without experiencing collisions upon exit. The longitudinal velocity distribution f from the beam is then an image of the thermalized velocity distribution in the cell volume and follows the relation

$$f_\mathrm{den}(v) = \frac{4}{\pi}\left(\frac{m}{2k_\mathrm{B}T}\right)^{\frac{3}{2}} v^2 e^{\frac{-mv^2}{2k_\mathrm{B}T}} \tag{6.6}$$

for a density measurement or by

$$f_\mathrm{fl}(v) = C\frac{4}{\pi}\left(\frac{m}{2k_\mathrm{B}T}\right)^{\frac{3}{2}} v^3 e^{\frac{-mv^2}{2k_\mathrm{B}T}} \tag{6.7}$$

for a flux measurement, where C is a normalization factor. Note that the measured velocity distribution of particles with mass m is only given by the temperature.

This changes when λ becomes comparable to the diameter of the aperture d_ap. The ratio of the mean free path and the typical length scale of the flow field is called the Knudsen number $\mathcal{K}_n = \frac{\lambda}{d_\mathrm{ap}}$. When $\mathcal{K}_n \ll 1$ particles will experience many collisions in the aperture region and the speed of the particles will be boosted to higher velocity classes. When expanding into a vacuum region, the particles will undergo further collisions during the expansion until the density has fallen to a point where collisions can be neglected (free molecular flow). The number of collisions a particle experiences and the associated boost in velocity w is dependent on the initial density in the cell and therefore the flow rate. The longitudinal velocity distribution measured in an experiment can then be described by a drifting Maxwell Boltzmann distribution

$$P(v) = C\left(\frac{m}{2\pi k_\mathrm{B}T}\right)^{3/2} v^3 e^{\frac{-m}{2k_\mathrm{B}T}(v-w)^2}. \tag{6.8}$$

w is a function of the distance to the aperture and can be calculated as it will be described later in 6.2.1 and 7.2.2. Note that w is not the most probable velocity. The peak of a measured distribution will lie at higher velocities:

$$v_\mathrm{p} = \frac{mw + \sqrt{m}\sqrt{12k_\mathrm{B}T + mw^2}}{2m} \tag{6.9}$$

Figure 6.2 shows the longitudinal velocity distribution for an effusive source of ^{39}K at $T = 4\,\mathrm{K}$ in blue and the final velocity distribution of ^{39}K for an expansion with 9 sccm[1] through an aperture with $d_\mathrm{ap} = 5\,\mathrm{mm}$ calculated by the sudden freeze model described later in 7.2.2 and assuming full entrainment in the ^{4}He flow field.

[1] standard cubic centimeters per minute

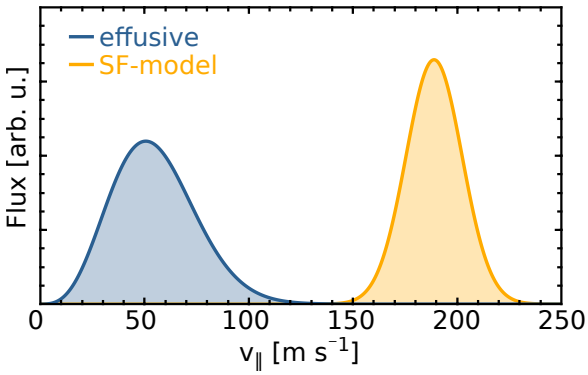

Figure 6.2.: Velocity distributions of ^{39}K at $T_{\mathrm{Cell}} = 4\,\mathrm{K}$. In blue the effusive velocity distribution is shown. The orange curve shows a hydrodynamically boosted distribution following equation 6.8, where w and T have been calculated by the sudden freeze model, which will be outlined in 7.2.2.

In the intermediate regime where most CBGB's are operated the final velocity will lie in between the limits of pure effusive flow and the full hydrodynamic entrainment.

We will come back to the beam formation process and the corresponding velocity boost in 7.2.3, for our measurements of ^{39}K, where we also go into more detail about the entrainment of ^{39}K in the ^{4}He flow.

6.2. Model of the ^{4}He Flow Field

In this section we describe our model of the ^{4}He flow field inside of the buffer gas apparatus. The ^{4}He is responsible for the hydrodynamic entrainment of the molecules, and the flow field will have an impact on the extraction characteristics of the cell. The introduced model yields a qualitative picture and quantitative results in terms of the density and pressure inside the CBGB as a function of mass flow rate and it predicts a longitudinal velocity distribution coming near to the ones observed in experiments.

6.2.1. ^{4}He as a Compressible, Inviscid Fluid

A simplification useful for estimating the properties of the buffer gas cell is the model of one-dimensional fluid flow. The equations stated in this section are taken from [18] and can be found in any other textbook dealing with compressible fluid flow and super sonic flow. As far as we know this is the first time this model is used to describe the behavior of a CBGB.

Neglecting the ablation process and assuming that the ^{4}He entering the CBGB has the same temperature as the cell walls, there is no entropy exchange in the system. Hence the flow of the ^{4}He buffer gas can be described by an isentropic flow. The one-dimensional fluid flow model assumes that the properties of the flow field are constant over every individual cross-section perpendicular to the fluid velocity. If the flow direction is the x-axis then the properties of the fluid flow are only dependent on x. This simplification does not account for the viscosity of the fluid flow but the main properties of buffer gas cells, such as the pressure P and density ρ inside the cell as well as the velocity of the fluid w at the aperture, can be derived from that model. The Navier-Stokes equations in the one-dimensional fluid flow model are simplified to:

$$\textbf{Continuity Equation:} \quad \frac{\mathrm{d}w}{w} + \frac{\mathrm{d}\rho}{\rho} + \frac{\mathrm{d}A}{A} = 0$$

$$\textbf{Momentum Equation:} \quad w\mathrm{d}w = -\frac{\mathrm{d}P}{\rho}$$

$$\textbf{Energy Equation:} \quad w\mathrm{d}w + \mathrm{d}h = 0$$

$$\textbf{Equation of State:} \quad P = \frac{\rho k_\mathrm{B} T}{m}$$

here A is the cross-sectional area perpendicular to the flow direction and h is the specific enthalpy. We describe ^{4}He as an ideal gas. A characteristic velocity in the flow field is the speed of sound

$$c = \sqrt{\kappa \frac{k_\mathrm{B} T}{m}} \tag{6.10}$$

which is the speed at which a pressure disturbance propagates through the flowing medium. Here κ is the adiabatic index which is $\kappa = \frac{5}{3}$ for monatomic gases like ^{4}He.

Assuming an isentropic flow of an ideal gas through a channel with changing cross-sectional area A we can write:

$$\frac{\mathrm{d}A}{A} + \frac{\mathrm{d}w}{w} \cdot \left(1 - \frac{w^2}{c^2}\right) = 0 \tag{6.11}$$

$$\frac{\mathrm{d}A}{A} + \frac{\mathrm{d}w}{w} \cdot \left(1 - \mathcal{M}_a^2\right) = 0 \tag{6.12}$$

where $\mathcal{M}_a$ is the Mach number which is defined as the ratio $\mathcal{M}_a = \frac{w}{c}$. Depending on whether the flow field moves at supersonic speed with $\mathcal{M}_a > 1$ or at subsonic speed $\mathcal{M}_a < 1$ greatly influences the behavior of the flow field. Note, that for a compressible fluid flowing at velocities well below the sonic velocity $\mathcal{M}_a \ll 1$, the fluid behaves similar to an incompressible fluid. When the cross-sectional area is decreasing ($\frac{\mathrm{d}A}{A} < 0$) the fluid flow w is increasing ($\frac{\mathrm{d}w}{w} > 0$) vice versa to fulfill the continuity equation. This is due to the fact that at subsonic speed all pressure disturbances can travel fast enough through the flow field such that the change in density $\frac{\mathrm{d}\rho}{\rho} \approx 0$.

If the fluid moves at $\mathcal{M}_a > 1$ an increase in cross-sectional area $\frac{\mathrm{d}A}{A} > 0$ leads to an increase in the fluid flow velocity $\frac{\mathrm{d}w}{w} > 0$. To fulfill the continuity equation the density will fall $\frac{\mathrm{d}\rho}{\rho} < 0$ correspondingly.

Assuming a volume filled with a gas at pressure p_0 which is coupled through a channel to a volume with pressure $p < p_0$ the gas will flow in the direction of the volume with lower pressure and the flow will reach sonic velocity $\mathcal{M}_a > 1$ if

$$\frac{p}{p_0} \leq \left(\frac{2}{\kappa+1}\right)^{\frac{\kappa}{\kappa-1}} \underbrace{\approx}_{\kappa=5/3} 0.487 \tag{6.13}$$

is fulfilled. This is the case for the comparably high buffer gas densities needed for thermalization and the high vacuum region outside of the cell. From formula 6.11 we can also deduce that $\mathcal{M}_a = 1$ will be reached at the smallest cross-sectional area A, which is located at the aperture of the CBGB.

Now we can already build a qualitative picture of the flow field in a buffer gas beam source. The cross-sectional area of the cell is typically large compared to the diameter of the aperture. If the smallest cross-sectional area is indeed the aperture, ^{4}He will behave as an

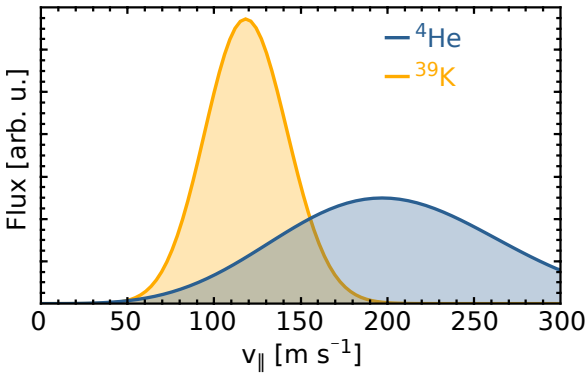

Figure 6.3.: Longitudinal velocity distribution at the aperture calculated by the equation 6.8 using the one-dimensional fluid flow model. The assumed stagnation temperature $T_0 = 4\,\mathrm{K}$ leads to $T_{\mathrm{ap}} \approx 3\,\mathrm{K}$ and $w_{\mathrm{ap}} \approx 102\,\mathrm{m\,s^{-1}}$ for ^{4}He and ^{39}K.

incompressible fluid inside the cell volume and the density, pressure and temperature will be mostly homogeneous. Sonic velocity will be reached at the aperture ($\mathcal{M}_a = 1$). Further downstream, due to the increasing cross-sectional area A, the flow velocity w is increasing and the density ρ and temperature T will decrease. Note that no pressure information downstream of the aperture can travel upstream into the cell if sonic velocity is reached inside the aperture. This means that the inner cell dynamics are independent of the changes in cross-sectional area downstream.

More quantitative statements can also be made, as all fluid properties can be calculated as a function of $\mathcal{M}_a$ and the stagnation conditions T_0 and p_0, which are the pressure and temperature of the gas at $w = 0$:

$$w = \mathcal{M}_a \cdot \sqrt{\kappa \frac{k_{\mathrm{B}} T_0}{m} / (1 + \frac{\kappa - 1}{2} \mathcal{M}_a^2)} \tag{6.14}$$

$$\frac{p}{p_0} = (1 + \frac{\kappa - 1}{2} \mathcal{M}_a^2)^{\frac{-\kappa}{\kappa - 1}} \tag{6.15}$$

$$\frac{T}{T_0} = (1 + \frac{\kappa - 1}{2} \mathcal{M}_a^2)^{-1} \tag{6.16}$$

$$\frac{\rho}{\rho_0} = (1 + \frac{\kappa - 1}{2} \mathcal{M}_a^2)^{\frac{-1}{\kappa - 1}} \tag{6.17}$$

If we assume a stagnation temperature of $T_0 = 4\,\mathrm{K}$ we calculate the flow velocity and temperature of ^{4}He at the aperture to be $w_{\mathrm{ap}} \approx 102\,\mathrm{m\,s^{-1}}$ and $T_{\mathrm{ap}} \approx 3\,\mathrm{K}$. Additionally we can calculate the longitudinal velocity distributions at the aperture, which this model predicts for ^{4}He or for a particle of interest fully entrained and thermalized with the ^{4}He flow field after the formula 6.8. Figure 6.3 shows the corresponding distributions at the aperture for ^{4}He and ^{39}K as an example particle entrained in the flow field.

The calculated velocity distributions at the aperture would be observed in an experiment, if downstream from the aperture the fluid properties freeze out and free molecular flow comes into play. The distributions already come quite near to the ones observed in the experiments. Still, for most sources the experimentally observed distributions are shifted towards higher velocities, since further collisions in the expansion have to be accounted for. In fact, for our

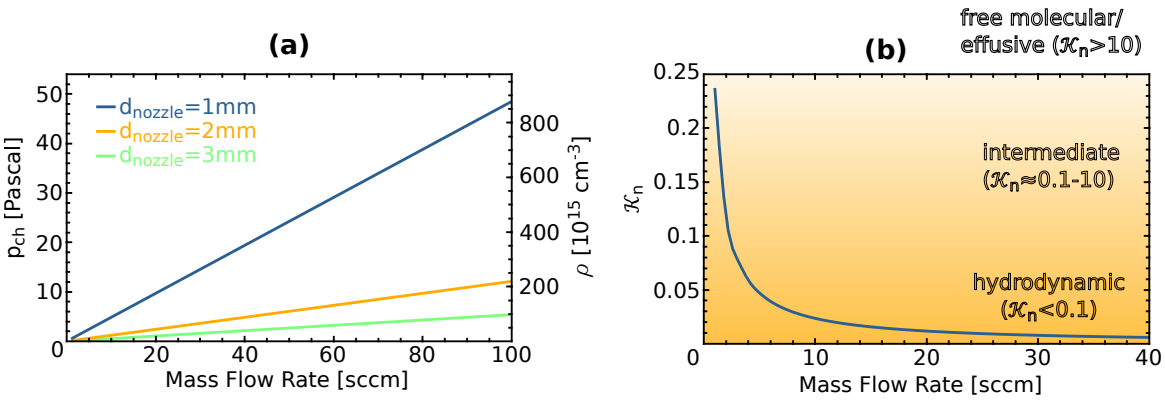

Figure 6.4.: **(a)** The number density and pressure for a 4 K ^{4}He buffer gas cell calculated by the hydrodynamic one-dimensional fluid flow model as a function of applied mass flow rate. As the fluid velocity w at the aperture is fixed for a given stagnation temperature T_0 a linear increase in mass flow results in a linear increase in the chamber pressure. **(b)** Flow regimes in the beam formation region, here for a cell with $d_{\mathrm{ap}} = 3\,\mathrm{mm}$ where $\mathcal{K}_n = \frac{\lambda}{d_{\mathrm{ap}}}$ as a function of flow rate. To calculate λ we calculate the density at the aperture with a hydrodynamic model. However, an effusive model differs only by a factor of 2. Most experiments work at flow rates $\mathcal{F}$ between 1-10 sccm in the intermediate to hydrodynamic regime.

source of ^{39}K the mean velocities always lie slightly higher than calculated here, even for the lowest mass flow rates (see section 7.2.3).

Typically the helium flow in the experiments is regulated by a mass flow controller. With the aforementioned equations and remembering the ideal gas law $pV = Nk_{\mathrm{B}}T$ we can deduce a formula for the pressure inside the buffer gas chamber depending on the mass flow if we assume that the properties inside the buffer gas chamber represent the stagnation conditions:

$$p_{\mathrm{ap}} = \frac{4k_{\mathrm{B}}T_{\mathrm{ap}}}{\pi d_{\mathrm{ap}}^2 w_{\mathrm{ap}}} \cdot \frac{\mathrm{d}N}{\mathrm{d}t} \tag{6.18}$$

$$p_{\mathrm{Cell}} \approx p_0 = \frac{1}{0.487} p_{\mathrm{ap}} \tag{6.19}$$

where $\frac{\mathrm{d}N}{\mathrm{d}t}$ is the number of atoms flowing through the aperture per second which is given by the mass flow rate typically measured in sccm, where $1\,\mathrm{sccm} \hat{=} 4\,5 \cdot 10^{17}\,\mathrm{atoms\,s^{-1}}$ for ^{4}He. Figure 6.4 **(a)** shows the pressure and number density inside a buffer gas chamber as a function of mass flow rate for three different aperture diameters.

Figure 6.4 **(b)** shows the Knudsen number $\mathcal{K}_n$ calculated for $d_{\mathrm{ap}} = 3\,\mathrm{mm}$. The distinction between the different flow regimes is not sharp but is often stated to be as indicated [18]. The flow rates $\mathcal{F}$ we apply to our cell are between $\mathcal{F} \approx 2 - 50\,\mathrm{sccm}$, here the Knudsen number lies mostly in the hydrodynamic regime.

The velocity of the fluid in the cell chamber w_{c} with cross-sectional area A_{c} can be calculated by using the conservation of flux

$$\rho_{\mathrm{c}} w_{\mathrm{c}} A_{\mathrm{c}} = \rho_{\mathrm{ap}} w_{\mathrm{ap}} A_{\mathrm{ap}} \tag{6.20}$$

$$\underbrace{\rightarrow}_{\rho_{\mathrm{c}} \approx \rho_0} w_{\mathrm{c}} = \frac{\rho_{\mathrm{ap}}}{\rho_0} \frac{w_{\mathrm{ap}} A_{\mathrm{ap}}}{A_{\mathrm{c}}}. \tag{6.21}$$

Here, the assumption $\rho_{\mathrm{c}} \approx \rho_0$ can be made due to the fact that the Mach number is well below 1 inside the cell volume. The factor $\frac{\rho_{\mathrm{ap}}}{\rho_0}$ can then be calculated using relation 6.17 and

setting $\mathcal{M}_a = 1$. $w_{\mathrm{ap}} \approx 102\,\mathrm{m\,s^{-1}}$ is known, such that w_{c} becomes a function of only $\frac{A_{\mathrm{ap}}}{A_{\mathrm{c}}}$. Note that therefore the velocity inside the cell w_{c} is to first order independent of the mass flow rate $\mathcal{F}$.

6.3. OpenFOAM-Simulations

The previous section employed the frictionless one-dimensional fluid flow model and gave a first insight into the properties of the flow field. In fact, the flow field will not be constant over every cross section perpendicular to the flow velocity due to the viscosity of ^{4}He and the friction to the cell walls. To account for this effect the following section is about the simulations I implemented using the open-source computational fluid dynamics program OpenFOAM. Here I simulate the three-dimensional ^{4}He flow field in our actual cell geometry taking viscosity into account.

One consequence of friction and viscosity is the emergence of vortices in the flow field. In previous experiments it has already been seen that these can obstruct extraction, as particles are trapped inside the vortices and are not entrained towards the aperture [95]. The purpose of this section is to understand under which conditions vortices appear for the parameters present in our experiment and how they can be circumvented.

6.3.1. Simulation of the ^{4}He Flow

The ^{4}He flow field is calculated by using the compressible fluid flow solver rhoCentralFOAM. The solver is capable of solving flow phenomena which incorporate compressible behavior, supersonic flow ($\mathcal{M}_a > 1$), viscous effects and turbulence. All simulations shown here were carried out in three dimensions.

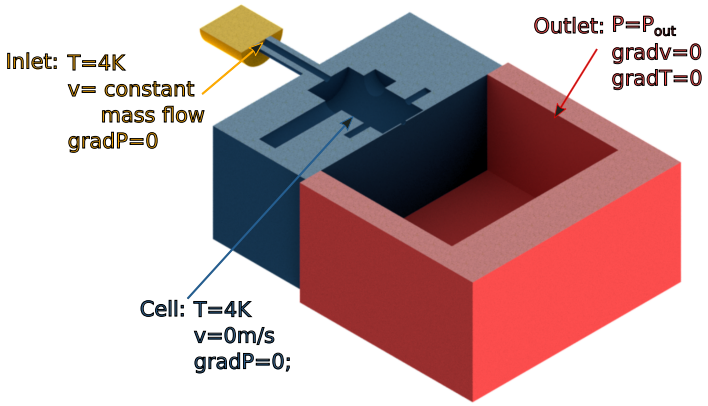

Figure 6.5.: CAD-Model which is used to define the different patches and generate the mesh together with the boundary conditions used in the OpenFOAM simulation. The condition fixedValue assigns a value to the boundary and keeps it fixed throughout the simulation. With zeroGradient the value can alter throughout the simulation and is assigned from the value of the neighboring inner cells onto the boundary.

Figure 6.5 shows the configuration in space and the boundary conditions we feed in our simulation. Table 6.1 shows the OpenFOAM solvers, mesh generation algorithm and physical models used and in table 6.2 the given parameters[2] can be seen.

[2]The parameters used are from reference [96]. The viscosity is fitted to the equation given in [97] by the Sutherland transport model implemented in OpenFOAM.

Simulation Software	OpenFOAM v. 2.3.0
Solver	rhoCentralFoam
Mesh Generation	snappyHexMesh
Transport model	sutherlandTransport
Turbulence model	laminar

Table 6.1.: Solvers used in the simulation of the ^{4}He-flow field

Equation of state	$pV = Nk_\mathrm{B}T$	perfect gas
Molar mass	M	$0.004\,\frac{\mathrm{kg}}{\mathrm{mol}}$
Specific heat	c_P	$5193\,\frac{\mathrm{J}}{\mathrm{kg\cdot K}}$
Prandtl	$\mathcal{P}_r$	0.66
Viscosity	$\mu(T) = \frac{A_\mathrm{s}\sqrt{T}}{1+T_\mathrm{s}/T}$	$A_\mathrm{s} = 1.098 \cdot 10^{-6}$ $T_\mathrm{s} = 4.995$ $\mu(4\,\mathrm{K}) = 9.7 \cdot 10^{-7}\,\frac{\mathrm{kg}}{\mathrm{ms}}$

Table 6.2.: Parameters used in the simulation of the ^{4}He flow field.

A typical result of our simulations is presented in Fig. 6.6, here the color coding follows the Mach number. The fluid shows increased Mach numbers, and therefore compressible behavior, at the inlet where the cross-sectional area changes drastically and at the aperture region. At the location of the aperture $\mathcal{M}_a = 1$ is reached, in agreement with the one-dimensional fluid flow model of the previous section. After the aperture the gas accelerates further and the pressure drops under the finite background pressure p_bg which we use in the simulation (typically $p_\mathrm{bg} = 0.01\,\mathrm{Pa}$).

Even further downstream of the aperture the hydrodynamic simulation gives nonphysical results showing the expected behavior of a supersonic expansion into a volume with finite background pressure [18]. Here the gas slows down due to the deceleration from the finite background pressure. This hydrodynamic effect will not be present for an expansion into a vacuum where collisions with the background gas can be neglected and the free molecular flow regime will manifest itself. Therefore we will ignore the simulated results far downstream and will only consider the behaviour in the vicinity of the aperture and upstream of it. Note that the exact value of the background pressure is of no importance for the results given by the simulation inside the buffer gas cell volume as no pressure information outside of the buffer gas cell can travel inside due to the supersonic flow at the aperture[3].

6.3.2. Turbulence inside the Flow Field

The Reynolds number defined as $\mathcal{R}_e = \frac{wL}{\nu}$ can be used to describe the influence of turbulence on the flow field. Here L is a characteristic linear dimension of the flow field and ν is the kinematic viscosity. By describing if either viscous or inertial forces are dominant in the fluid flow, the Reynolds number can be used to describe whether a flow field will exhibit laminar or turbulent behavior. Another helpful relation to calculate the Reynolds number is the von Kármán relation $\mathcal{R}_e = \frac{\mathcal{M}_a}{\mathcal{K}_n}$.

Inside the cell volume the Mach number is $\mathcal{M}_a < 1$ at every point. The Knudsen number in the flow field inside the cell with a typical length scale of $L = 25\,\mathrm{mm}$ lies at $\mathcal{K}_n \approx 0.023$ for

[3] the interested reader may read further under the keyword "choked flow".

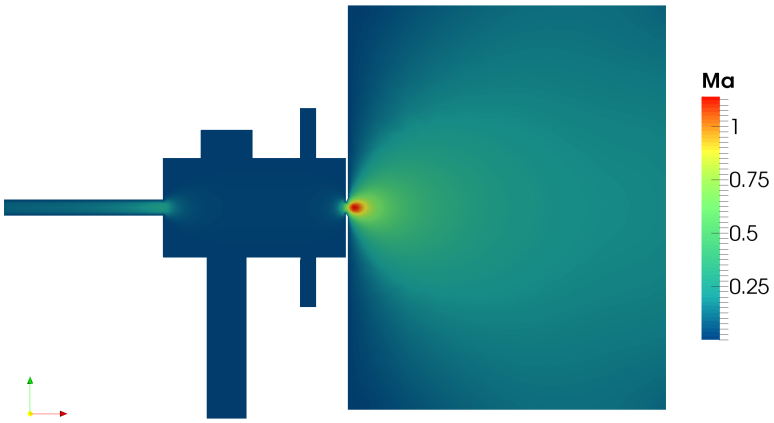

Figure 6.6.: Typical result out of the finite element computation software OpenFOAM with finite background pressure at the outlet. Here simulated for a mass flow rate of 10 sccm and a background pressure of 0.001 Pa. The picture shows a slice through the middle of the chamber. Inside the aperture $\mathcal{M}_a = 1$ is reached. The quitting surface lies here at distance of about one aperture diameter from the exit of the cell. All properties outside of the quitting surface will be ignored as we do not expect hydrodynamic behavior downstream but free molecular behavior instead.

a cell with a 3 mm aperture and $\mathcal{F} = 10\,\text{sccm}$. We estimate an upper bound for the Reynolds number $\mathcal{R}_e = \frac{\mathcal{M}_a}{\mathcal{K}_n} \leq \frac{1}{0.023} \approx 43$.

For a flow inside a tube the characteristic Reynolds number for the onset of turbulence is $\mathcal{R}_e \approx 2600$. Our upper bound is still well below this typical Reynolds number indicating that turbulence should not play a role for the ^{4}He flow field inside of the cell volume. This is in agreement with the treatment of other groups [95]. Note that the flow exiting a buffer gas cell is also often referred to as low Reynolds number flow [17]. The simulations were first conducted with the $k\epsilon$ turbulence model implemented in OpenFOAM but no difference in the results were seen as compared to the results obtained from a laminar model. Due to the faster computation time for laminar flow, we decided to neglect turbulence in the ongoing simulations.

6.3.3. Different Flow Rates

Figure 6.7 shows the simulation results for the CBGB with $d_{\text{ap}} = 3\,\text{mm}$. We simulate four different flow rates $\mathcal{F}$ while keeping all other boundary conditions in the simulation constant. It can be seen that the helium enters the cell volume with subsonic velocities and decelerates due to the sudden change in cross-sectional area. Shortly before the aperture the gas is accelerated again to $\mathcal{M}_a = 1$ and leaves the cell. The velocity at which the gas enters the cell volume differs with flow rate. At the point of the gas inlet where the cross-sectional area changes abruptly vortices build up and increase in size with increasing flow rate. This behavior is similar to the well studied fluid flow case of a backward step. The gas that enters the cell volume has a high directivity flowing through the fill line tube. It then shoots ballistically into the cell volume and acts as a locomotive force on the vortices to its side. These vortices could possibly trap ablated molecules where they then would diffuse and most probably stick to a nearby cell wall and would not leave the cell volume through the aperture.

A second region where vortices can build up is directly upstream of the aperture, where the cross-sectional area again changes drastically. This situation would be similar to the

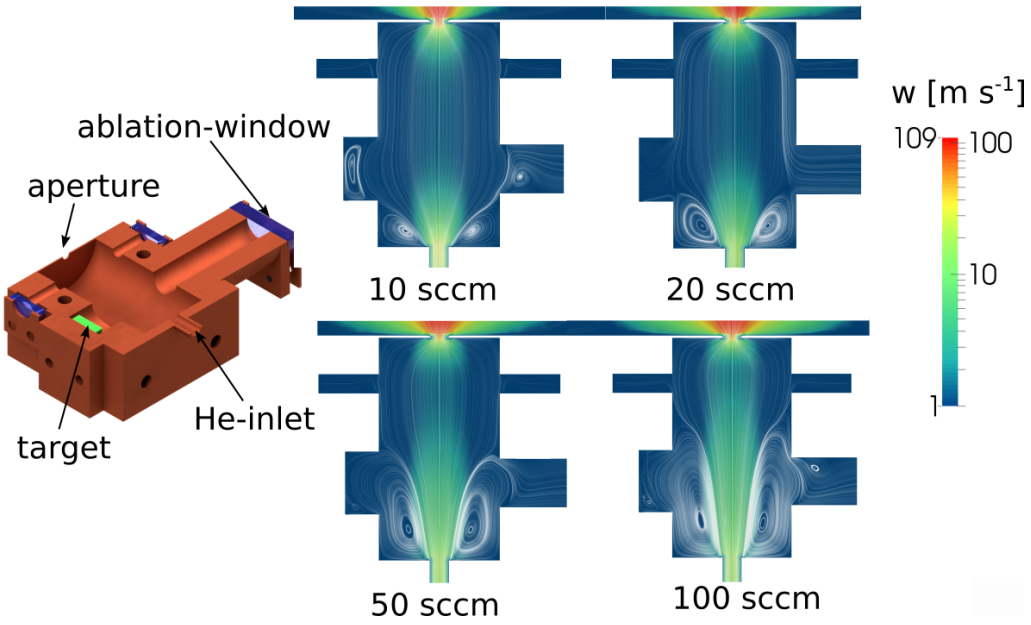

Figure 6.7.: Flow field simulated at different flow rates *mathcalF*. The color coding represents the velocity of ^{4}He gas at the respective point, while the white streamlines represent the movement of the ^{4}He gas flow. As the flow rate gets higher the flow velocity on the center line is increasing, but the column width of the directed flow is decreasing due to vortices which build up on the side of the cell.

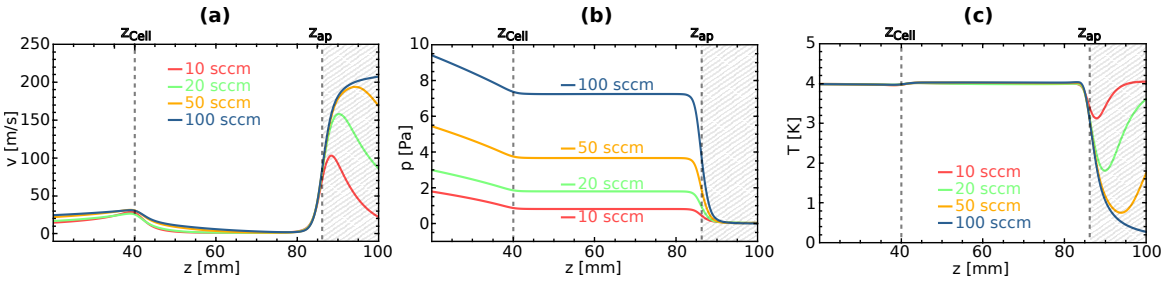

Figure 6.8.: Center line values for the simulations shown in Fig. 6.7. In **(a)** it can be seen that the final velocity inside the cell volume is $z_{\mathrm{Cell}} < z < z_{\mathrm{ap}}$ is approximately constant for all flow rates, but the velocity at which the gas enters the cell near z_{Cell} increases for increasing flow rate. **(b)** and **(c)** show the corresponding graphs for pressure and temperature respectively. Results at $z > z_{\mathrm{ap}}$ are not considered as the validity of the hydrodynamic simulation is not given here (grey shaded area).

fluid dynamic case of a forward step. However, with the flow rates applied we do not see any vortices building up here. Due to the thin aperture plate the directivity of the fluid flow directly upstream and downstream of the aperture is less directed and therefore the vortex building is significantly reduced as compared to the situation near the fill line.

Fig. 6.8**(a)** shows the velocity plotted along the center line. Again it can be seen that for higher flow rates the fluid velocity downstream of the inlet increases, whereas the final velocity further downstream inside the cell is roughly the same for all flow rates. Figure 6.8**(b)** and **(c)** show the center line values of pressure p and temperature T. The pressure rises linearly with flow rate as it is expected and the temperature is nearly constant throughout the cell volume. At the aperture where the velocity rises the temperature starts to decrease as expected in an isentropic expansion where thermal energy is converted into kinetic energy.

6.3.4. Different Aperture Diameters

Figure 6.9 shows simulation results obtained when the flow rate is kept constant and the aperture diameter is varied. The pressure inside the cell drops for a larger apertures due to the fixed flow velocity $w = 102\,\mathrm{m\,s^{-1}}$ inside the aperture and the constant mass flow rate. The average velocity inside the flow volume rises accordingly but especially the distance to reach the final value of velocity increases with increasing aperture size, such that the gas shoots ballistically further inside the cell volume and therefore vortices near the gas inlet increase in size for increasing aperture diameter (see Fig. 6.9).

The gas inlet has an inner diameter of $d_{\mathrm{in}} = 4\,\mathrm{mm}$ such that the one-dimensional fluid flow model would suggest that for apertures where $d_{\mathrm{ap}} > d_{\mathrm{in}}$ the sonic velocity would already be reached near the inlet of the gas. Due to friction to the cell walls, this is still not the case for $d_{\mathrm{ap}} = 5\,\mathrm{mm}$ here, but for even larger aperture sizes this has to be considered.

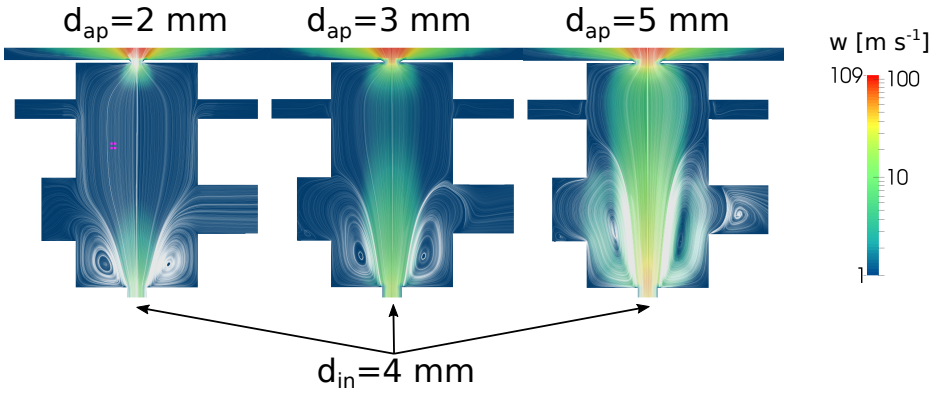

Figure 6.9.: Different aperture sizes at a flow rate of $\mathcal{F} = 50\,\mathrm{sccm}$. For larger apertures the flow velocity at the inlet increases, leading to vortices in the flow field near the inlet.

6.3.5. Placement of a Diffuser

The previous simulations have shown, that for the simple cell design up to now, vortices appear near the inlet of the ^{4}He gas for increasing flow rates and for increasing aperture diameters.

This can be circumvented by the placement of a diffuser directly behind the inlet which forbids the ^{4}He gas to shoot ballistically into the cell volume [87, 98]. The left side of Fig. 6.10 shows the design of the diffuser and how it is integrated into the buffer gas assembly. The right side of Fig. 6.10 shows the effect on the ^{4}He flow field if such a diffuser is used. It can be seen that vortices are efficiently circumvented and a smooth flow field results.

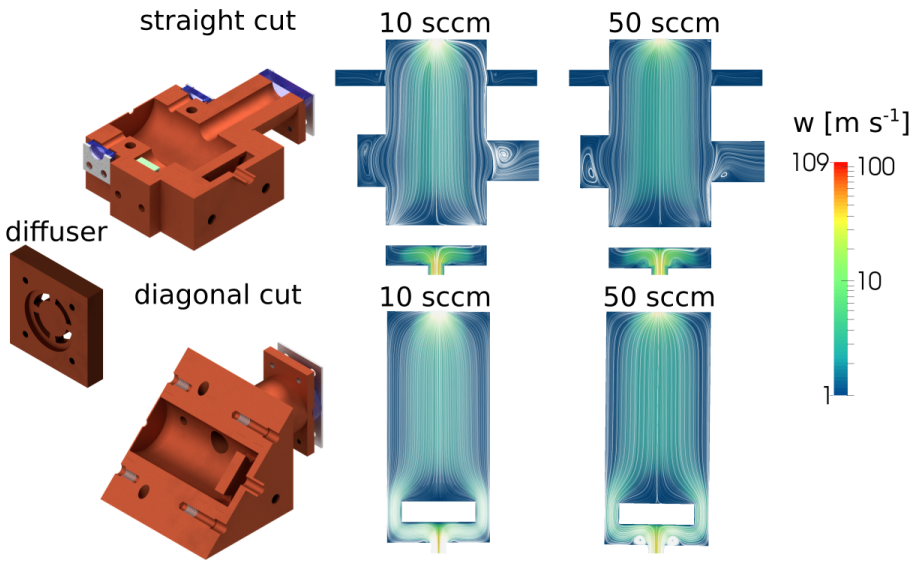

Figure 6.10.: The upper row shows a horizontal cut through the CBGB with the corresponding flow simulations. In this plane the flow is blocked by the diffuser plate shown on the left. The lower row shows a diagonal cut where the ^{4}He can flow through the diffuser. The placement of the diffuser plate right behind the inlet can circumvent the build up of vortices inside the Cell and a uniform flow field results even up to mass flow rates as large as 50 sccm. It can also be seen that the fluid moves faster on the center line than on the edges due to viscosity and friction to the walls. The distribution of flow velocities perpendicular to the flow direction obeys the Hagen-Poiseuille equation.

The design is similar to the one used in [87], where such a diffuser was experimentally installed and differences in the longitudinal velocity distributions have been observed.

6.3.6. Conclusion

We have seen that fairly small changes to the cell geometry have impact on the overall flow field of the ^{4}He gas. A higher flow rate not only increases the density inside the cell volume but also impacts the velocity field. This is not expected from the one-dimensional fluid flow model, where an increase in mass flow rate simply leads to an increase in density, but is a consequence of the finite viscosity of the gas.

Turbulence should not play a role for all flow rates applied here ($\mathcal{F} < 100$ sccm).

For the viscosity used in the simulations macroscopic vortices build up at flow rates higher than $\mathcal{F} > 10$ sccm. Another circumstance which can cause vortices is the ratio of d_{in} to d_{ap}. As long as $\frac{d_{\text{in}}}{d_{\text{ap}}} \gg 1$ the ballistic shooting into the cell volume is relatively weak becoming stronger with increasing d_{ap}. This effect has to be considered when different aperture sizes are experimentally investigated to optimize the cell performance. The implementation of a diffuser plate behind the gas inlet circumvents vortices for all flow rates applied here.

The ballistic shooting into the cell volume might be guided and used to get a fast extraction of molecules, which to our understanding is to some extent the principle of the source used in [40].

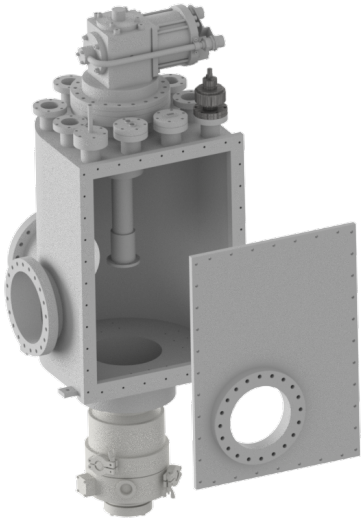

Figure 6.11: Vacuum chamber for the cryogenic apparatus. A viton sealed door allows quick access to the cryogenic assembly. On the top several CF40 flanges allow additional feedthroughs to be installed. The d-shape base sectional area allows for thinner steel walls as a corresponding cubic chamber. The cryogenic head is installed on the top via a CF160 flange. At the bottom of the chamber a turbopump is directly attached through a CF160 flange.

6.4. Experimental Apparatus

The experimental apparatus designed and implemented in the laboratory during this thesis has the purpose to serve as a high flux beam source of cold and slow molecules.

6.4.1. Vacuum System

The main vacuum parts are shown in Fig. 6.11. We use a two stage cryogenic head[4] attached to a custom built vacuum chamber[5]. The chamber has a d-shape base cross-sectional area, which gives us the possibility to have a viton sealed door on its flat side for quick access. Due to the cylinder like shape on the other side, the chamber can be built lighter than a chamber with a square base cross-sectional area. Apart from the viton sealed door all connections are conflat flanges[6].

On the bottom of the chamber a turbopump[7] is attached directly to a CF160 flange to have a large pumping cross section. The turbopump is backed by a dry scroll pump[8]. On the top of the chamber an ion gauge[9] is installed to observe the pressure during operation.

Down the molecular beam line a quadrupole mass spectrometer[10] is installed, which may be used as a detection device for ablated molecules in addition to optical detection. Although we believe the mass spectrometer to have a higher detection threshold than resonant optical detection it has the big advantage of being molecule independent. Mass spectrometers measuring the current of the ionized particles, have typical reaction times $t_{\text{react}} > 1\,\text{ms}$ to changing signals, too slow to resolve molecular beam pulses out of buffer gas cells with typical pulse widths ranging from several 100 µs to several 10 ms. Therefore, the mass spectrometer has a pulse ion counting output which we read out with a multi channel scaler[11] with an adjustable bin width from 200 ns upwards[12].

[4] Sumitomo RDK 415E
[5] VAb Vakuum-Anlagenbau GmbH
[6] the decision in favor of conflat flanges was due to compatibility reasons with other experiments in our institute
[7] Leybold Turbovac 360
[8] Agilent IDP-15
[9] Pfeiffer full range gauge
[10] Hiden Analytical RC PIC QMS, 200 amu, cross beam ion source
[11] FastComtec P7882
[12] the same Multi-Channel-Scaler might be used later to read out optical signals from a photo multiplier tube

6.4.2. Radiation Shields

The second stage of the cryogenic head is able to reach a base temperature of 4 K when the heat load is reduced to 1.5 W. After evacuating the chamber the biggest contribution to the heat load is the black-body radiation emitted by the surrounding vacuum chamber lying at room temperature of about 295 K. To reduce this we implemented a radiation shield on the first stage of the cryostat. The heat load on the second stage is thereby reduced to a value that allows us to cool the second stage down to 3.5 K. To this second stage the CBGB is attached. All materials if not otherwise noted are made out of oxygen free copper[13], to ensure a good thermal conductivity at cryogenic temperatures [99]. All connections of the assembly are first cleaned with isopropanol and acetone and are afterwards covered with a thin layer of cryogenic grease[14] to enhance the heat conductivity. To protect the assembly from getting loose due to thermal contraction during cool down we use flexible steel Belleville washers[99] which keep the connections tight. Additionally the threads of all screws assembled in blind holes are smoothed on one side in such a way that no virtual leaks result.

Furthermore we attach a second shield around the CBGB anchored at the 4 K-stage. The inner surface of this second shield is coated with coconut charcoal[15] glued to the copper with cryogenic glue[16], which at cryogenic temperatures acts as a cryopump for the ^{4}He flowing in our chamber. The cryopumping is crucial for the experiment, the background pressure rises by more than $\Delta p \approx 1 \cdot 10^{-5}\,\mathrm{mbar\,sccm^{-1}}$ without it, consistent with the pumping speed of our turbopump of $380\,\mathrm{l\,s^{-1}}$ for ^{4}He. With the implementation of the cryopump this increase in pressure went down by two orders of magnitude. For the flow rates applied the background pressure rises about $1 \cdot 10^{-7}\,\mathrm{mbar\,sccm^{-1}}$, which is low enough for the molecular beam source.

Care was taken that no parts of the assembly come near to the aperture of the CBGB and are all at least 4 cm away since all ^{4}He scattered at surfaces near the aperture might attenuate the particle beam. The front plate of the 4 K shield has a hole of 1 cm diameter. We additionally prepared a front plate where a skimmer can be mounted, which also has an open aperture of 1 cm. Skimmers are typically used in molecular beam experiments to reduce beam attenuation due to back-scattered atoms.

Both radiation shields have slotted holes to give optical access for the ablation laser $\mathcal{L}_{ab}$ and several detection lasers $\mathcal{L}_{\perp}$ for a transverse detection (see also Fig. 6.14). The optical access given by the windows allows for a characterization of the beam properties from directly behind the aperture at $z_0 = 0\,\mathrm{mm}$ up to $z = 44\,\mathrm{mm}$ down the beam path. The windows are made out of uncoated NBK-7 and block black-body radiation with $\lambda > 2\,\mu\mathrm{m}$ efficiently.

6.4.3. Buffer Gas Fill Line

The buffer gas is supplied through a ^{4}He gas bottle, and a pressure regulator[17] reduces the pressure from $p_{\mathrm{bottle}} \leq 200\,\mathrm{bar}$ to $p_{\mathrm{supply}} \approx 2\,\mathrm{bar}$. The whole fill line consists of electropolished stainless steel tubing[18] connected with standard Swagelok fittings[19] and several low pressure valves[20] are implemented. A digital flowmeter[21] is installed in the gas fill line regulating the ^{4}He gas flow between $2 - 100\,\mathrm{sccm}$. Behind the flow meter a Pirani gauge[22] is attached to monitor the gas pressure in the fill line. The last connection to the vacuum chamber is done

[13] the cell itself is built out of a ofc cylinder with CW009a, whereas the base plates and the radiation-shields are ofc copper CW008a
[14] Apiezon N
[15] Aquacarb 207C
[16] Stycast 2850 with 24LV catalyst
[17] Swagelok Stainless Steel PR-regulator
[18] Swagelok 6L-T6M-S-1.0M-6M-E2, O.D. 6 mm, I.D. 4 mm
[19] SS-6M0-6
[20] Swagelok 6LVV-DP56M
[21] Bronckhorst F-201CV-100-AAD-33-V
[22] Pfeiffer TPR270

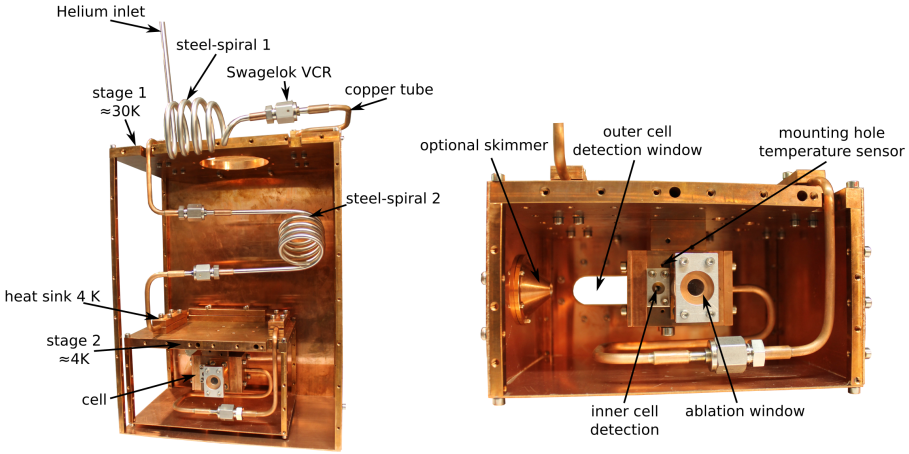

Figure 6.12.: Pictures of the cryogenic assembly before being implemented in the vacuum chamber. The cell shown is the version with optional extension and diffuser. The charcoal on the inner side of the 4 K-shield was later applied. Here the front plate with the skimmer is shown.

with an all metal flexible tubing[23].

The buffer gas enters the vacuum chamber through a liquid feedthrough[24] which is attached to a stainless steel tube spiral[25] which acts as a thermal insulation due to its length and the low heat conductivity of steel [99]. The spiral is attached to a copper tube[26] which is thermally anchored on the 40 K base plate on the other side. After entering the 40 K radiation shield the fill line is thermally decoupled with a steel spiral again before it is thermally anchored on the base plate of the 4 K stage. Ultimately the fill line is attached to the buffer gas cell.

6.4.4. Buffer Gas Cell

Our first cell geometry is based on the one described in [87] from which the geometry was already used to simulate the ^{4}He flow field in 6.3. The main body is a cuboid with a square base area of 50 mm · 50 mm. A 25 mm diameter bore acts as the inner area of the buffer gas cell. The ^{4}He enters through the backface of the cell through an inlet with 4 mm inner diameter and can exit the cell through an aperture on the opposite site.

We prepared apertures with inner diameters of 1,2,3 and 5 mm for later experimental optimization. Perpendicular to the main beam line a hole is drilled to give optical access for the ablation laser and on the opposite side a molecular precursor target can be mounted. Cryogenic glue[27] is used to mount the target on the target holder made out of oxygen free copper which is then inserted and sealed to the main cell body. An additional through bore gives optical access for an inner cell detection of the ablated material. The windows[28] are clamped down with thin aluminum plates, ensuring that during the cool down the windows do not crack due to different expansion coefficients of the different materials, instead just the aluminum will bend [88]. An extension is used to mount the ablation window farther from the ablation target, which has been seen to coat the windows, reducing the transmission

[23] Swagelok 321-4-X-12-B2, care has to be taken since some parts are only available with 1/4" fittings and the correct reducer fittings have to be used

[24] VAB CF40VCR1/4-1L-I

[25] all inner vacuum connections of the buffer gas fill line are Swagelok VCR, since due to informations from [100, 101, 102] these are the most reliable to stay leak free despite thermal cycling between room temperature and cryogenic temperature

[26] Oxygen free copper CW009a, O.D. 6 mm, I.D. 4 mm

[27] Stycast2850

[28] Thorlabs WG41050 and WG40530

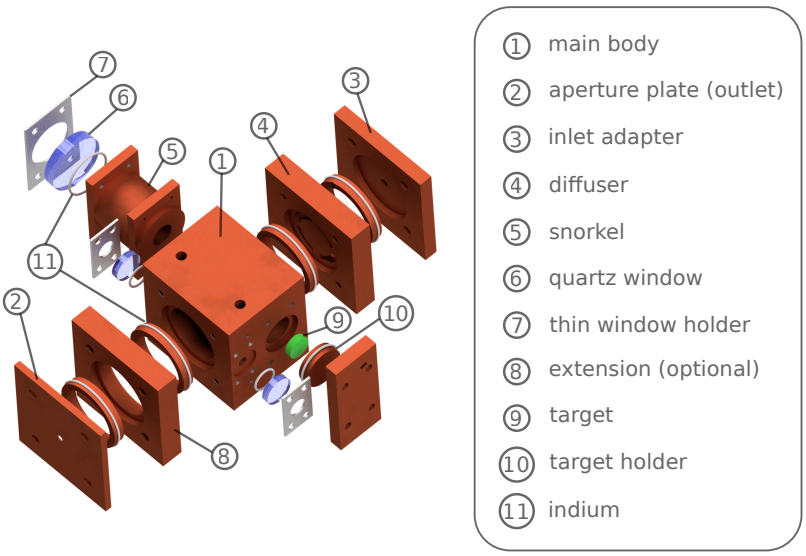

Figure 6.13.: Explosion image of the buffer gas cell. The parts are sealed to each other with an indium sealing, as it is explained in [99].

of the ablation light. Optional the cell can be extended by 10 mm and can be equipped with a diffuser plate. There are several threaded holes in the chambers main body where a temperature sensor can be mounted. To be sure that our cell stays ^{4}He-tight in such a way that the sum of all leaks out of the cell are in total much smaller than the aperture diameter, we seal our chamber via indium. As far as we know, this is typically not done for buffer gas cells and is maybe unnecessary, but as it is easily implemented and fast to realize we decided in favor of an indium seal. Figure 6.13 shows an explosion image of our CBGB and the indium seal are also indicated. The relatively soft indium protects the window additionally. For sealing two copper parts to each other the indium is wrapped around an O-ring holder with 25 mm inner diameter, which is afterwards placed between two copper parts with the corresponding depression[99].

6.4.5. Temperature Measurement and Regulation

There are several temperature sensors[29] which can be installed on the cell main body, the base plates or at the shieldings of the apparatus. We monitor two temperature sensors at a time, one on the buffer gas cell and one on the 40 K radiation shield via a temperature controller[30]. All temperature sensors are in the CU-package allowing for easy installation and are read out using a four-lead measurement scheme.

Two cartridge heaters[31] are inserted into two bores in the base plate of the 4 K stage. These can be used to heat the 4 K radiation shield to temperatures $T > 10\,\mathrm{K}$ to release absorbed ^{4}He from the activated charcoal. Later these heaters could also be used to run the second stage at higher temperatures for example at $T = 15\,\mathrm{K}$ to use ^{20}Ne as a buffer gas. As electrical UHV multipin feedthroughs we use a c-type[32] for the temperature sensors and D-type[33] suitable for up to 3 a per pin for the cartridge heaters.

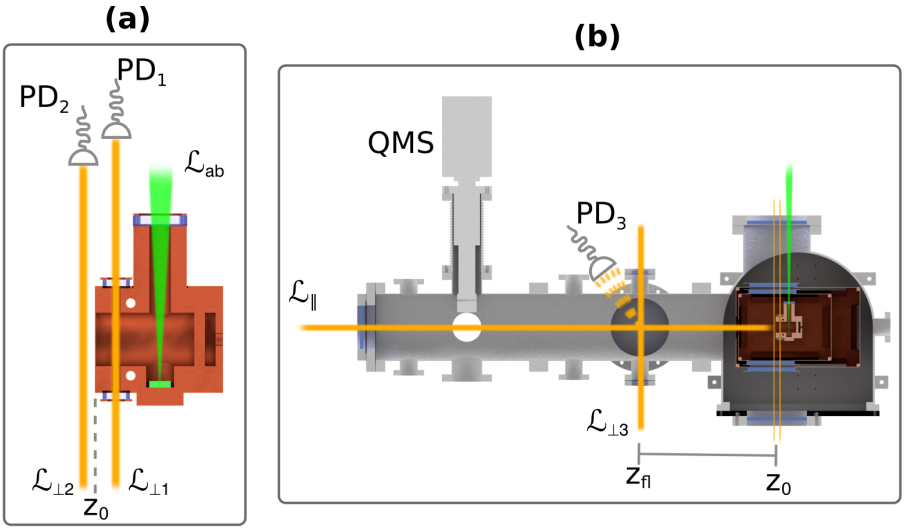

Figure 6.14.: Assembly used for the first measurements characterizing the ablation loaded CBGB. **(a)** Two absorption signals perpendicular to the molecular beam are recorded, one inside $\mathcal{L}_{\perp 1}$ and one directly behind the cell $\mathcal{L}_{\perp 2}$. **(b)** A third optical signal is recorded in fluorescence about $z_{\mathrm{fl}} = 40\,\mathrm{cm}$ behind the cell exit where the fluorescence of a perpendicular beam $\mathcal{L}_{\perp 3}$ and a parallel beam $\mathcal{L}_{\parallel}$ can be recorded. A quadrupole mass spectrometer can be moved into the beam path with a bellow and a compound table[34] further down the molecular beam path.

6.4.6. Apparatus for First Characterizations

Figure 6.14 shows the experimental apparatus used for first characterization measurements. We attach a CF160 tube to the main vacuum chamber described in the previous section. The CF160 tubes have several CF connectors to its side and are suitable for the characterization purposes here. We use three optical detection regions in the apparatus. Laser $\mathcal{L}_{\perp 1}$ measures the absorption inside the CBGB on photodiode PD_1. The signal on PD_2 measures the absorption of $\mathcal{L}_{\perp 2}$ directly downstream of the aperture. The signals here are high enough such that no differential measurement is needed. The aperture at z_0 defines the starting point of the beam path and at $z_{\mathrm{fl}} = 32\,\mathrm{cm}$ we use a fluorescence detection on PD_3 to measure the longitudinal velocity profile through the induced fluorescence of $\mathcal{L}_{\parallel}$. Similar to the detection scheme used in chapter 5 we use a laser $\mathcal{L}_{\perp 3}$ to pump the atoms into the detection state.

[29] silicone diode temperature sensor from Cryo Con S950-BB
[30] Cryo-Con Model 22C
[31] Cryo-Con 25 Ω and 25 W
[32] C-type subminiature feedthrough two-9-pins on DN40CF
[33] SubD-9 on CF40 flange
[34] Proxxon KT150

7

Performance of the Buffer Gas Cell

This section shows first measurements characterizing the CBGB. In particular, a KCl target was used to produce ^{39}K by ablation and, which has been subsequently detected as described in 6.14. The characterizations are not finalized yet and a thorough investigation of different geometries will be part of Paul Kaebert's PhD thesis.

In the following section, I will first describe the transverse absorption signals near the buffer gas cell. I will then characterize the influence of the flow rate and reproduce the measurements with cfd simulations to gain insight into the physical processes apparent in the buffer gas beam source.

Afterwards I focus on the measured longitudinal velocity distributions and describe them as a result of a hydrodynamic beam formation process.

7.1. Measured Extraction Characteristics

First we investigate the extraction characteristics of the buffer gas cell. The measurements shown here are a buffer gas cell with an exit aperture of $d_{\mathrm{ap}} = 3\,\mathrm{mm}$ and the diffuser plate installed. For all measurements shown here, the ablation laser is a Nd:YAG with a wavelength of $\lambda = 1064\,\mathrm{nm}$ and a pulse duration of approximately 6 ns. We ablate at a frequency of $f_{\mathrm{ab}} = 1$ Hz with an energy per pulse of 12.6 mJ.

Figure 7.1 **(a)** shows the absorption signals as measured directly behind the CBGB on PD_2 for several flow rates $\mathcal{F}$. The pulses have widths of several ms and have an asymmetric shape typical for ablation loaded buffer gas beam sources [95, 103, 104, 44]. For increasing flow rate $\mathcal{F}$ the peaks appear at later times and the following decay gets slower for increasing $\mathcal{F}$. This qualitative behavior we see for all versions of our CBGB's. As it was delineated in section 6.1.3, there are two processes leading to extraction of the cell, namely diffusion and advection. For increasing $\mathcal{F}$ the density inside the buffer gas cell rises accordingly and thereby the diffusion decreases leading to later arrival times of ^{39}K in the detection region.

The decay of the signals at times t long after the peak timing $t > 2t_{\mathrm{p}}$ is well described by a single exponential decay. For increasing $\mathcal{F}$ the decay time increases which further supports the interpretation of slower diffusion due to a higher density inside the cell. The good agreement of a single exponential decay suggests that no vortices built up inside the cell at the shown flow rates. As vortices were seen in [104] to lead to a decay which needs to be described by a double exponential decay model[1]. We speculate that the diffuser plate

[1] In the double exponential model one decay describes the washout of ablated material in parts of the flow field which is directed to the outlet, whereas the other decay describes particles trapped in vortices which slowly diffuse into regions with the flow directed to the aperture [104].

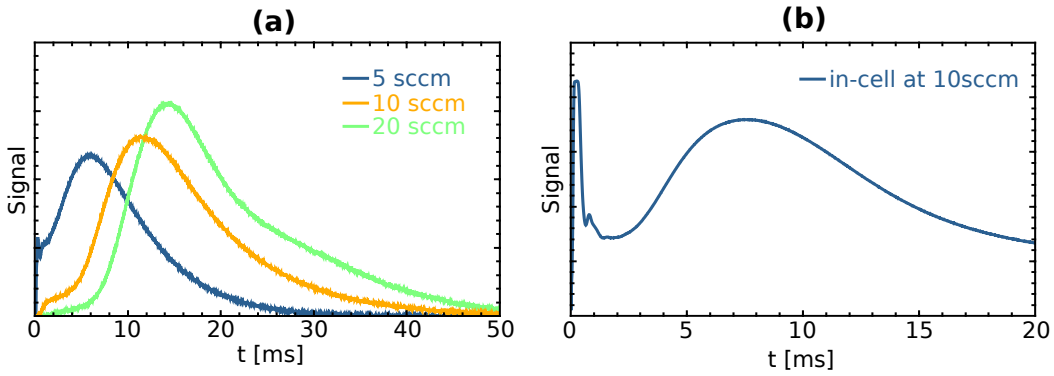

Figure 7.1.: **(a)**Absorption signal measured directly downstream of the aperture on PD_2 for several flow rates. **(b)** Absorption signal upstream of the aperture on PD_1 for $\mathcal{F} = 10$sccm.

prevents vortices from building up inside the cell.

The signal on PD_1, which measures absorption inside the cell typically saturates for our ablation conditions. A signal with a rather low ablation yield and no saturation of the photodiode is shown in Fig. 7.1 **(b)**. Here, the signal shows a large shot to shot fluctuation and most of the time shows multiple narrow peaks at very short times after the ablation complicating the analysis of the signal. However, qualitatively the signal shows the same behavior for increasing $\mathcal{F}$. Still due to the saturation and the large shot to shot fluctuation we typically use the absorption outside of the cell on PD_1 to normalize the fluorescence signals further downstream, where we measure the longitudinal velocity distribution, on the number of ^{39}K atoms which left the cell.

7.1.1. Diffusion-Advection Model (Scalar Transport)

Here we simulate the extraction of ^{39}K from the buffer gas cell with the CFD software OpenFOAM. The approach is similar to the one used in [104, 89]. We take the ^{4}He velocity flow field calculated as described in 6.3 for the respective cell geometry and assume that the ablation does not alter the flow field. We model the evolution of ^{39}K concentration c inside the ^{4}He flow field with the scalar transport quotation

$$\frac{\partial c}{\partial t} = \vec{\nabla}^2(D_m c) - \vec{\nabla}(\vec{v}c). \tag{7.1}$$

Here D_m is the diffusion coefficient given by [105]

$$D_m = \frac{3}{8}\left(\frac{N}{\pi}\frac{m_{\mathrm{He}} + m_{\mathrm{K}}}{2 m_{\mathrm{He}} m_{\mathrm{K}}}\right)^{1/2} \frac{(k_{\mathrm{B}}T)^{3/2}}{p\sigma_{\text{K-He}}\Omega_{\text{K-He}}}, \tag{7.2}$$

where $\sigma_{\text{K-He}}$ is the thermally averaged diffusion cross section and $\Omega_{\text{K-He}}$ is the collision integral which is typically of order 1 [105]. Inside our cell the pressure p and temperature T are nearly constant so that the equation can be simplified to

$$\frac{\partial c}{\partial t} = \underbrace{D_m \vec{\nabla}^2 c}_{\text{diffusion}} - \underbrace{\vec{v}\vec{\nabla}c}_{\text{advection}} . \tag{7.3}$$

We use the OpenFOAM solver *scalartransportFoam*. As fitting parameters we use the diffusion coefficient D_m and the size and location of the ^{39}K plume after the ablation for a certain flow rate.

Simulation Software	OpenFOAM v. 2.3.0
Solver	scalarTransportFoam
Initialisation of molecular distribution	funkySetFields

Table 7.1.: Software used for simulating the molecule evolution in the ^{4}He-flow field

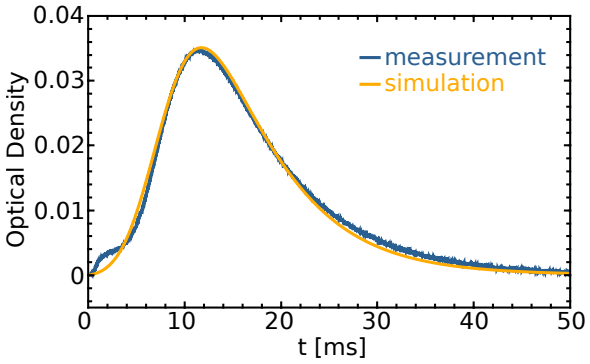

Figure 7.2.: Measred and simulated evolution of ^{39}K for 10 sccm and a 3 mm aperture.

7.1.2. Results of the Scalar Transport Model

Figure 7.2 shows the measured absorption signal directly behind the buffer gas cell (signal on PD_2) together with a simulation. The simulation agrees very well with the measurement showing the correct peak time t_p and has the same timescale τ during the decay of the signal. For this result we assume the initial condition to be centered at $r_0 = 4$ mm above the target and to have a spatial distribution following equation

$$c(r) = \exp(-\frac{(r-r_0)^2}{\sigma^2}) \tag{7.4}$$

with $\sigma = 9$ mm.[2] The diffusion coefficient D_m used in the simulation is $D_m = 4.8 \cdot 10^{-4}\,\mathrm{m^2\,s}$ from which we can calculate a cross section of $\sigma_{\text{K-He}} = 2.35 \cdot 10^{-14}\,\mathrm{cm^2}$ for $\Omega_{\text{K-He}} = 1$. The value obtained is in good agreement with values for collision cross sections have been reported in the literature to be to be on the order of $10^{-14}\,\mathrm{cm^2}$ [17, 104, 44, 103].

To check if the simulations have good agreement with the measurements at other flow rates, we tried to predict the transverse signal for a measurement where we did not change the ablation point and only altered the flow rates $\mathcal{F}$. We then took the parameters used for our best simulation for a flow rate of $\mathcal{F} = 10$ sccm and scaled the diffusion coefficient D_m inversely proportional with the calculated density and shrunk σ of the initial distribution by the same factor.

Figure 7.3**(a)** shows the obtained results. The simulation has qualitatively the same trend as the measurement in the sense that the peaks arrive later in the detection region for higher flow rates. The right flank of the potassium signal is governed by the process of diffusion and extraction after thermalization and is to first order independent of the initial ^{39}K distribution in the cell. Here the simulations give good agreement between simulation and experiment. Figure 7.3**(b)** shows the measured and simulated decay times of the signals fitted by a simple exponential decay model

[2] These starting conditions are on the same order as a Monte-Carlo toy model predicted as a length the particles travel before thermalized with the cold ^{4}He (see A.3)

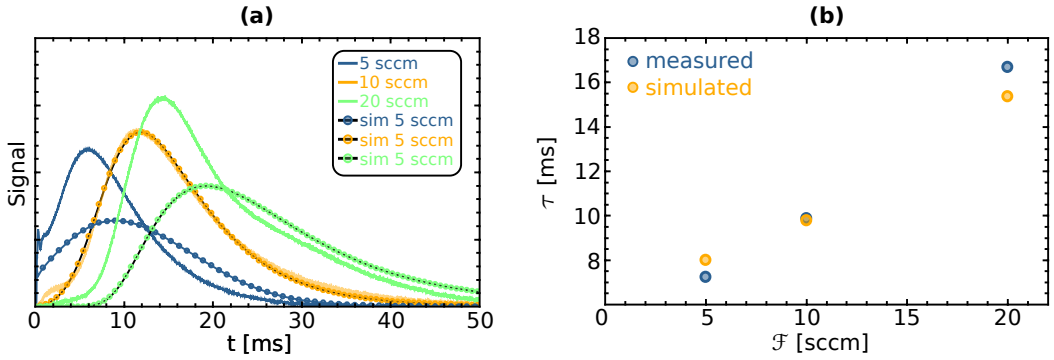

Figure 7.3.: **(a)** Simulations of the extraction of the cell for different flow rates $\mathcal{F}$ together with the measured signals. For the simulations the diffusion D_m and the size of the initial distribution σ are scaled with a $\mathcal{F}^{-1}$ dependence. The qualitative behavior is similar for measurement and simulation. Increasing $\mathcal{F}$ leads to later arrival times of the peak signal t_p. Quantitatively t_p is only poorly reproduced. **(b)** Measured and simulated decay times τ at long timescales $t > 2t_\mathrm{p}$ showing good quantitative agreement suggesting that the model fits well at long timescales.

$$c(r) = A \cdot \exp(-\frac{t}{\tau}) \tag{7.5}$$

where A is a scalar fitting factor and τ is the decay time. When the signal is characterized by a peak time t_p we fitted the exponential decay for $t > 2t_\mathrm{p}$.

Extraction Efficiency

A figure of merit in the experiment is the number of molecules washed out of the cell. We take the integral of our measured absorption data as a measurement for the number N of ^{39}K atoms leaving the cell. This number saturates at $\mathcal{F} = 20\,\mathrm{sccm}$ in our experiment. We can not compare this number to the total number of ^{39}K atoms produced during the ablation N_tot as we can not measure this quantity. In the simulations on the other hand we know the initial amount of ^{39}K inside the cell volume and can therefore calculate an extraction efficiency $\mathcal{E}$. Figure 7.4 shows the result of our simulations together with the measured integrals scaled by a constant scalar. The simulations confirm the qualitative expectations that for higher flow rates a higher fraction of ^{39}K atoms $\mathcal{E}$ is washed out of the cell. Whereas the simulation already seem to saturate at a flow of $\mathcal{F} = 10\,\mathrm{sccm}$. Note that simulations and fitting to experimental data is still ongoing work, and more quantitative conclusions are only expected when comparing more data with the corresponding simulations. Up to now our best estimate for a maximum extraction efficiency is $\mathcal{E}_\mathrm{max} \approx 25\,\%$ for a flow rate of $\mathcal{F} = 20\,\mathrm{sccm}$.

7.1.3. Summary and Limits of the Scalar Transport Model

While the calculated collision cross section $\sigma_\mathrm{K\text{-}He}$ are in good agreement with values of other experiments and the simulations reproduce the temporal shape of the ^{39}K at long timescales $t > 2t_\mathrm{p}$, the exact arrival time of the peak signal t_p is only poorly reproduced, presumably due to the simplification of a constant diffusion parameter D_m in the simulation. D_m is principally dependent on the temperature T inside the buffer gas cell, therefore the simulation assumes that the temperature of the buffer gas is constant between the ablation and the extraction of the molecular pulse. In previous experiments it has been measured that the time molecules need to thermalize in a buffer gas cell is on the ms-timescale and

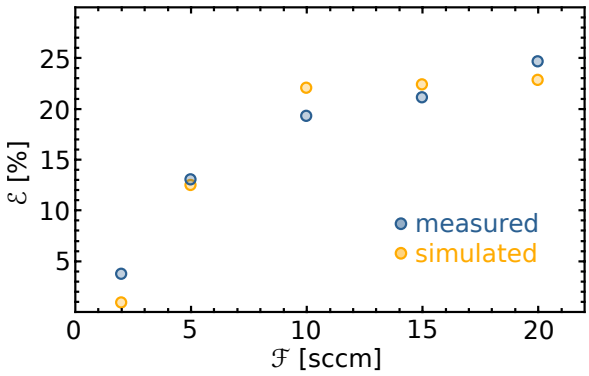

Figure 7.4.: Simulated extraction efficiencies $\mathcal{E}$ in orange. The measured signals have been integrated and the obtained values have been fitted to the simulated values, giving our best estimate for the extraction efficiency of our cell in blue.

dependent on the ^{4}He density and therefore the flow rate [104, 106]. Therefore the diffusion coefficient should be larger during the first ms after the ablation in the buffer gas heated by the ablation pulse and then decays to its value at $T = 4\,\mathrm{K}$ with a timescale proportional to the ^{4}He density in the cell. With such an improvement it might be possible to reproduce the measured signals to a higher degree.

The simple $\mathcal{F}^{-1}$ scaling of the size of the initial ^{39}K distribution is an additional simplification which presumably does not capture all physical processes. For example the hydrodynamic expansion of the hot ^{39}K from the ablation spot into the buffer gas which will be discussed in 7.1.4.

Summing up the simulations using a scalar transport equation show good agreement with the experiment concerning the decay times τ of the signal at times well behind the peak of the signal scaling with density in agreement to the scalar transport model. A collision cross section $\sigma_{\text{K-He}} = 2.35 \cdot 10^{-14}\,\mathrm{cm}^{-2}$ has been calculated well in the range of typical cross sections measured in other buffer gas beam sources [17, 104, 44, 103]. Also the scaling of the extraction efficiency with flow rates seems to be reproduced by the simulations, but further measurements with changing cell geometries are necessary for verification.

A simulation predicting the extraction efficiency with a high reliability would be very helpful as then the cell geometry can be optimized efficiently before implementing it in the experiment. With the scalar transport model and presumably a non constant diffusion parameter this goal should be in reach.

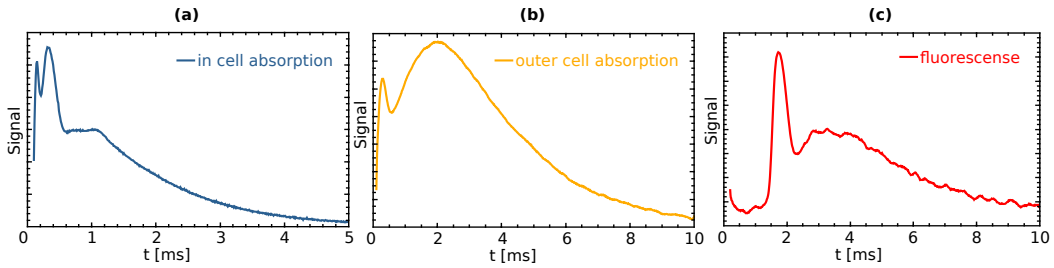

Figure 7.5.: Typical absorption signals on **(a)** PD_1, **(b)** PD_2 and **(b)** fluorescence signal on PD_3 obtained when the measured signals are maximized by changing the position of $\mathcal{L}_{ab}$ on the ablation target. There are narrow peak structures at early arrival times, which are not captured by the simple advection-diffusion description.

7.1.4. Multi-Peak Structure

Figure 7.5 **(a)** shows the transverse absorption signals inside the cell and **(b)** behind the aperture . Whereas in **(c)** a Doppler sensitive fluorescence signal resonant with a longitudinal velocity class of $v_{\parallel} = 216\,\mathrm{m\,s^{-1}}$ at $z_{fl} = 0.32\,\mathrm{m}$ is shown. These signals typically result when the ablation laser is readjusted on the target on a new ablation spot to maximize the ablation yield. Additionally to the diffusive atomic signal which we modeled in the previous section 7.1.1 there are additional peaks appearing at very short times after the ablation. These structures have also been seen before by other groups [103, 89, 107] and up to now we are not aware of an explanation of this feature in previous works.

The peaks at short times are changing in height from ablation shot to ablation shot but the time they appear is reproducible. Most of the times we observe one additional peak but as shown in Fig. 7.5**(a)** with a high ablation yield we see up to two peaks, appearing at reproducible times after the ablation. We also measure this feature in the longitudinal fluorescence signal where it is typically highest at longitudinal velocities of about $200 - 250\,\mathrm{m\,s^{-1}}$ indicating that the atoms thrown out of the buffer gas cell at early times seem to be relatively thermalized to the buffer gas.

These structures are not captured by the simple advection-diffusion model in 7.1.1 where it has been assumed that the ablation process does not alter the ^{4}He flow field. Here we propose an explanation for this feature as a result of the ablation process altering the ^{4}He flow field at short times after the ablation.

The ablation leads to a hot vapor at the target surface. The pressure inside this vapor should be several times higher than the surrounding pressure of the ^{4}He buffer gas. We tried to simulate the impact of a high temperature and pressure region near the target surface on our flow field. Unfortunately we were unable to do a full two species calculation up to now. Still we can draw a lot of information from a one species calculation where such an ablation bomb is introduced into the flow field. Therefore we use the same solver as was used to calculate the ^{4}He flow field *rhoCentralFoam* which is a transient solver. It calculates for every time step the whole Navier-Stokes equations and therefore can be used to model the given starting conditions. We take the converged flow field which was also presented in 6.3 as a starting field. We then initialize a small region on the surface of the target with a peak temperature of 100 K and a peak pressure of 100 Pa and simulate the effect on the flow field. The values for pressure and temperature are both well above the temperature and pressure of the surrounding gas in the buffer gas cell, but the exact values are somehow arbitrary, as here only the qualitative behavior will be simulated. The temperature and pressure in this region are defined by a three dimensional Gaussian with a standard deviation of 5 mm.

The results of the simulation are shown in Fig. 7.6. In the first row a pressure wave emitted from the target surface can be seen which travels at sonic velocity through the cell. This pressure wave carries temperature away from the ablation region, as can be seen in the

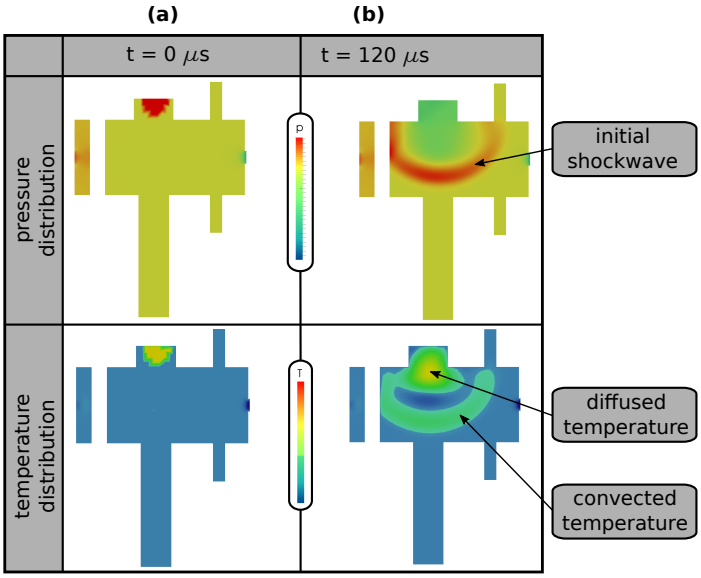

Figure 7.6.: **(a)** Initial starting conditions at $t = 0\,\mu s$ of the simulation. The upper row shows the initial pressure distribution. The lower row shows the initial temperature field. Apart from the region near the target surface pressure and temperature are nearly constant over the whole cell volume. **(b)** Result of the simulation at $t = 120\,\mu s$. The upper row shows a high pressure shock wave traveling nearly spherically away from the target surface. In the lower row it can be seen that two region of increased temperature arise. One is located quite near to the target surface and diffuses further. The other region is a result of the shock wave which convects temperature away from the diffusive part located near the target.

second row. Therefore two regions of increased temperature arise: One those transport is governed by diffusion in the first ms near the target surface and one region whose motion is governed by convection with the emitted pressure wave.

Finally we are interested in the evolution of ^{39}K in the non steady flow field simulated here. But note that the transport of temperature T follows the same equations as the transport of mass concentration c in 7.1.1. This is because temperature follows the same mechanism of diffusion and the transport due to bulk motion, which is called convection rather than advection for temperature. The transport equation for temperature is given by

$$\frac{\partial T}{\partial t} = \underbrace{D_T \vec{\nabla}^2 T}_{\text{diffusion}} - \underbrace{\vec{v}\vec{\nabla} T}_{\text{convection}} \quad , \tag{7.6}$$

which is the same as the equation for the transport of mass 7.1. The only difference is the diffusion coefficient D_T, which is typically higher for temperature than for mass diffusion, whereas the effective transport through advection/convection for mass and temperature are the same. Therefore if we track temperature in our simulations we can get the correct advective behavior of ^{39}K whereas the diffusive behaviour will be different due to $D_T \neq D_m$.

We therefore argue that ^{39}K produced through the ablation behaves similar to the temperature tracked in the shown simulation due to the same physical processes responsible for mass transport as for temperature transport. The result would be two regions of increased ^{39}K concentration in the buffer gas cell. A diffusive part which is later washed out by the helium through bulk motion like simulated in 7.1.1 and one region of high ^{39}K concentration which is advected by the pressure wave.

Additionally, note that at the region near the ablation spot in Fig. 7.6**(b)** the pressure

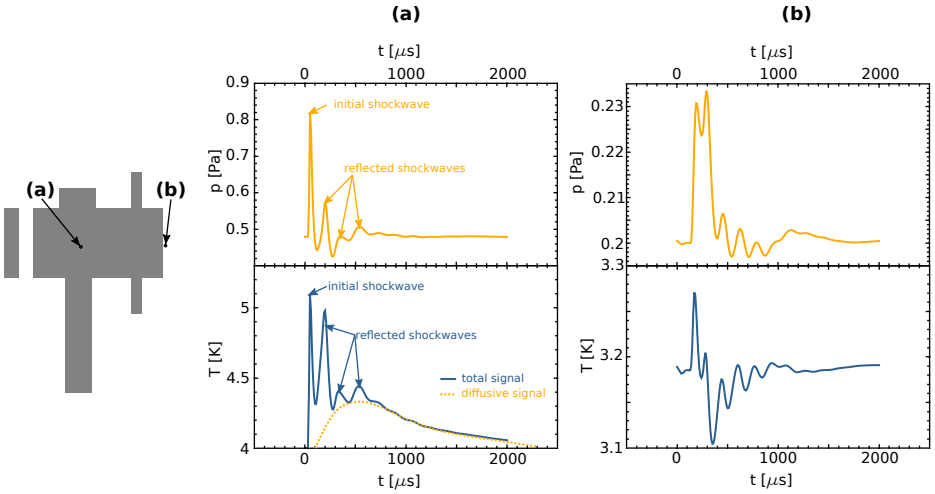

Figure 7.7.: In **(a)** time traces of pressure and temperature at the point indicated on the left over the target are shown. There are several shock waves apparent in the signal. The first peak is the initial shock wave which is then reflected a few times leading to an pressure oscillation of the buffer gas cell. The lower graph shows the temperature trace at the same point. The temperature has several peaks due to the convected part which is reflected back and forth through the cell and a slow diffusive underground. In **(b)** the corresponding graphs behind the aperture are shown. They show the same behavior of initial and reflected shock waves and the corresponding pressure and temperature oscillations. The diffusive part of the temperature is not seen in the signal as it diffuses too fast to be convected by the bulk motion to the aperture.

falls under the surrounding pressure and the temperature is increased in this region. Both circumstances would lead to a higher diffusion in the first few ms for ^{39}K due to the temperature and pressure dependence of D_m which after total thermalization reaches the value as simulated in 7.1.1. This supports the conclusion drawn in the previous section 7.1.1 that a changing diffusion parameter in the scalar transport model would be valid and would improve the simulations.

Figure 7.7 shows the time dependence of pressure and temperature at the shown points after the ablation. At the point situated over the target several pressure peaks can be seen which result from the initial shock wave as well as several reflections of it. In the temperature trace the advected heat appears together with the pressure wave. Here, the diffusive background can additionally be seen. The graphs on the right side show the corresponding graphs behind the aperture and show the same behavior. Here the diffusive part in the temperature is not apparent since the temperature diffusion is too fast such that it does not reach the aperture. The points in time where the pressure wave and the corresponding convected temperature travels through the observation region are the points where we do expect the ^{39}K peaks in our measurements. The first two peaks in temperature appear at $t_1 = 180\,\mu s$ and $t_2 = 280\,\mu s$ in the simulation. The measured peak shown in 7.5 lies at $t_{meas} \approx 300\,\mu s$ showing that the physical picture and the done simulation agree very well on the timescale. Therefore we think that this advective transport of a pressure wave after the ablation is the reason for the often seen multiple peak structure in laser ablation loaded buffer gas beam sources. The exact timing of the emitted pulses of ^{39}K will vary from ablation spot to ablation spot, due to the changing distance between ablation point and nozzle. And maybe even more due to the surface structure of the target. Depending on the roughness and the angle of the surface the initial direction and amplitude of the pressure wave may be heavily altered. Still the time between the ablation pulse and the initial peak and the subsequent times to the reflected peaks will always be on the order of

$$t_{\mathrm{sw}} \approx \frac{L_{\mathrm{Cell}}}{c(T)} \tag{7.7}$$

where L_{Cell} is a typical length of the buffer gas cell and $c(T)$ is the sonic velocity in the buffer gas at temperature T. For a cell with $L_{\mathrm{Cell}} \approx 2.5\,\mathrm{cm}$ and a temperature of $T \approx 4\,\mathrm{K}$ the sonic velocity is $c(4\,\mathrm{K}) \approx 114\,\mathrm{m\,s^{-1}}$ and therefore the typical peak time is $t_{\mathrm{sw}} \approx 220\,\mu\mathrm{s}$, giving good agreement to our measurements. Depending on the heat introduced into the buffer gas cell the sonic velocity may alter leading to deviations of t_{sw}.

We think that a full two species calculation might give further insight. We would expect, that the reflection at the cell walls is different for temperature and ^{39}K, as the ^{39}K atoms will most probably condense at the surface and will not appear in the reflected wave. This might be a reason why we see more temperature peaks in this qualitative simulation than we observe ^{39}K peaks in our measurements.

Figure 7.8.: ^{39}K^{37}Cl ablation target after several 1000 ablation shots showing the disrupted surface structure. The target is mounted with cryogenic glue (black) on the targetholder made of oxygen free copper.

7.1.5. Shot to Shot Variation of the Emitted ^{39}K Pulse

The emitted pulse of ^{39}K has a large shot to shot variation of up to 50 % in the amount of ^{39}K leaving the cell. Additionally we see that the temporal shape changes when the ablation laser is moved across the target. Moving the ablation spot several mm can lead to differences in the peak time t_{p} of several ms, seen in the experiment and in the simulations using the scalar transport model. Even when the ablation spot is not moved, the peak time changes slowly, most times to later times after a few absorptions. We attribute this behavior to changes in the surface structure of the ablation point, the Nd:YAG laser has a non Gaussian spatial beam profile and it is known from material processing that the ablation using these ns-Nd:YAG lasers leads to rather ugly ablation spots [108, 109]. Because of the different surface structure the power density on the surface changes for subsequent ablation shots, therefore ablating different amounts of material each time. Also the hydrodynamic expansion of the initially hot potassium plume near the target surface will probably change from shot to shot due to the changing surface structure leading to different spatial distributions of the ^{39}K after thermalization. Figure 7.8 shows a ^{39}K^{37}Cl ablation target after several 1000 ablation shots, it illustrates that the surface structure undergoes massive changes due to the ablation. Many of these effects might be circumvented by using beam homogenization of the ablation laser, for example with microlens arrays. This approach is used in material processing and mass spectrometry [110, 111], the ablated area should change significantly less from shot to shot and the signals might get more consistent.

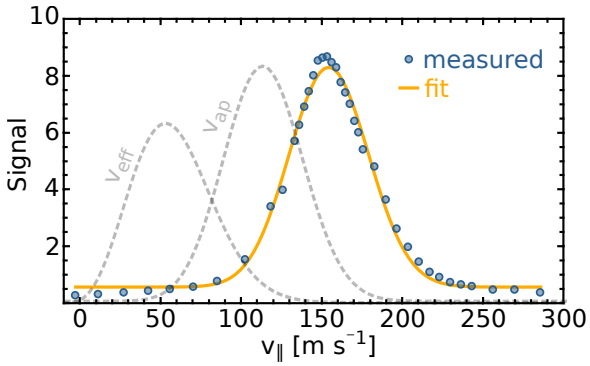

Figure 7.9.: Longitudinal velocity distribution measured in our experiment. For a flow of $\mathcal{F} = 9\,\mathrm{sccm}$ and a nozzle diameter of $d_{\mathrm{ap}} = 5\,\mathrm{mm}$. The data is well described by a drifted Maxwell-Boltzmann distribution (6.8). Here with $T = 3.05\,\mathrm{K}$ and $w = 141.7\,\mathrm{m\,s^{-1}}$ leading to a peak velocity of $v_{\mathrm{p}} = 155\,\mathrm{m\,s^{-1}}$. In gray a effusive distribution v_{eff} for ^{39}K is shown together with the hydrodynamic distribution calculated at the aperture v_{ap}. Indicating that further acceleration behind the aperture takes place.

7.2. Molecular Beam Formation

In the following I present measurements of the longitudinal velocity distribution of ^{39}K measured in our experiment. Afterwards an introduction to the sudden freeze model normally used to describe the final longitudinal velocity distribution of nozzle beams is introduced and it is argued why it has to be extended for the relatively low pressure expansion behind a buffer gas beam source to give results compatible with the observations.

7.2.1. Measured Longitudinal Velocity Distribution

We measure the longitudinal velocity distribution with the apparatus shown in Fig. 6.14. We detune $\mathcal{L}_{\parallel}$ to be resonant with a certain longitudinal velocity class on the $4^2S_{1/2}, (F = 2) \rightarrow 4^2P_{3/2}$ transition and measure the induced fluorescence on a photodiode PD_3. Additionally we repump the atoms into the detection state with a non Doppler sensitive laser $\mathcal{L}_{\perp 3}$ driving the $4^2S_{1/2}, (F = 1) \rightarrow 4^2P_{3/2}$ transition. The scheme is therefore similar to the one used in the foregoing chapter 5. For each detuning we average the signal on PD_3 for 16 ablation shots and normalize the signal to the observed ablation yield which leaves the cell measured in absorption on PD_2. The inner cell absorption on PD_1 showed a larger shot to shot noise and normalization to this signal did not correlate as well, whereas the normalization to the outer cell absorption on PD_2 gives highly reproducible results.

Figure 7.9 shows the measured longitudinal velocity distribution for a flow rate of $\mathcal{F} = 9\,\mathrm{sccm}$ together with a fit of a drifted Maxwell Boltzmann distribution. The distribution peaks at $v_{\mathrm{p}} = 155\,\mathrm{m\,s^{-1}}$, well above the most probable velocity of effusive ^{39}K at $T \approx 4\,\mathrm{K}$ ($v_{\mathrm{eff}} = 50\,\mathrm{m\,s^{-1}}$) and even above the hydrodynamic distribution at the aperture. Which we expect when ^{39}K is fully entrained inside the ^{4}He flow field up to the aperture (($w_{\mathrm{K}} = w_{\mathrm{K}} \approx 102\,\mathrm{m\,s^{-1}}$ and $T_{\mathrm{K}} = T_{\mathrm{He}} \approx 3\,\mathrm{K}$)) and then directly leaves the cell without further acceleration. For all flow rates measured $\mathcal{F} = 2 - 25\,\mathrm{sccm}$ the peak velocity in our experiment lies higher than predicted by the aforementioned models, indicating that further acceleration takes place during the expansion.

In the following I will describe this additional acceleration of ^{39}K by first describing the ^{4}He flow during the expansion with the sudden freeze model in 7.2.2. I will then explain the partial entrainment of ^{39}K in the expanding ^{4}He flow field leading to a temperature and velocity slip in 7.2.3.

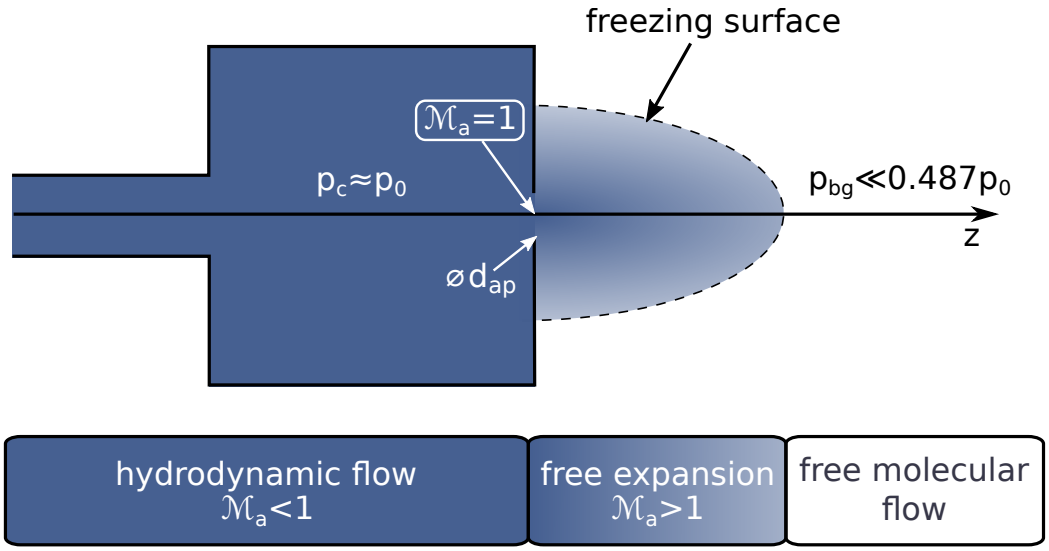

Figure 7.10.: Different flow regimes for the helium flow in a buffer gas beam source when the flow rate applied leads to a hydrodynamic behavior inside of the cell. Downstream of the aperture the density rapidly decreases and hydrodynamic effects will seize. The sudden freeze model assumes that a hydrodynamic description up until the freezing surface is valid where a sudden transition to free molecular flow takes place.

7.2.2. End of the Hydrodynamic Regime and Transition to Free Molecular Flow

The sudden freeze model [18] assumes that up to a certain distance behind the buffer gas cell the system is described by hydrodynamic equations and then makes a sudden transition to free molecular flow, see Fig. 7.10. At the location of the freezing surface the properties of the gas freeze out and then stay constant downstream the beam path. This is the case for longitudinal velocity and temperature. Whereas the density falls during the following geometric expansion. As long as the density is high enough the system can be described hydrodynamically and it can be shown [18], that for an axisymmetric free jet expansion the Mach-number $\mathcal{M}_a$ follows the equation:

$$\mathcal{M}_a[\epsilon] = \epsilon^{\kappa-1}(3\ 232 - 0\ 7563 \cdot \epsilon^{-1} + 0\ 3937 \cdot \epsilon^{-2} - 0\ 0729 \cdot \epsilon^{-3}) \tag{7.8}$$

where $\epsilon = \frac{z}{d_{\mathrm{ap}}}$ is the reduced distance with the aperture diameter d_{ap} and the symmetry axis z. Note that this implies that the temperature T_{He} and the forward flow velocity w_{He} of can be calculated for every point along z 6.2.1. And with this the longitudinal velocity $v_{\parallel}$ as a drifting Maxwell Boltzmann distribution can be given.

It can be shown that the mean number of collisions a particle will still experience downstream of its position ϵ during the expansion assuming a hard-sphere collision model is given by [18]

$$Z_2(\epsilon) = \sqrt{\frac{8}{\pi}} \sigma n_0 d F_{\mathrm{hs}}(\epsilon, \kappa, \delta) \tag{7.9}$$

where

$$F_{\mathrm{hs}}(\epsilon, \kappa, \delta) = \frac{1}{\kappa} \int_{\epsilon}^{\infty} \frac{1}{\mathcal{M}_a(\chi, \delta)} (1 + \frac{\kappa - 1}{2} \mathcal{M}_a(\chi, \delta))^{-1/(\kappa-1)} d\epsilon \tag{7.10}$$

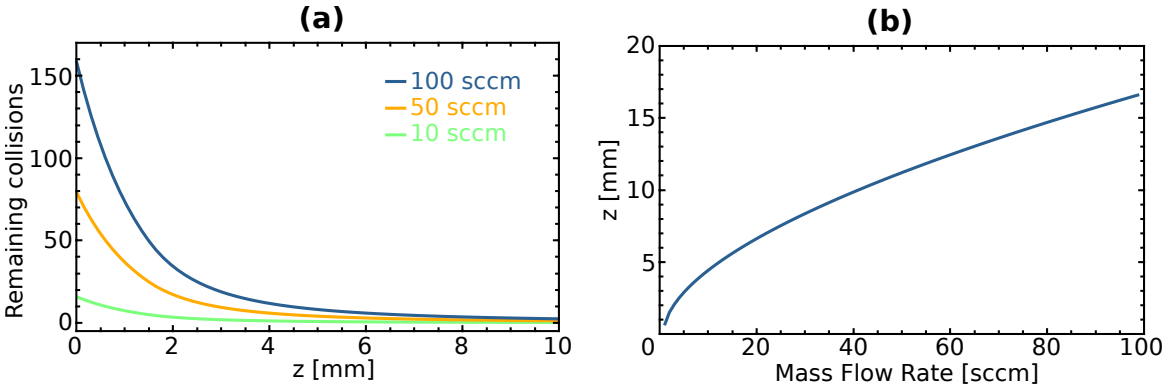

Figure 7.11.: **(a)**Remaining collisions for a molecule entrained inside the ^{4}He flow at 4K stagnation temperature and with $d_{\mathrm{ap}} = 3\,\mathrm{mm}$. For different flow rates as a function of distance from the cell exit. **(b)** Location of the quitting surface for $d_{\mathrm{ap}} = 3\,\mathrm{mm}$. For different flow rates.

The location ϵ_{qs} behind the aperture for which the number of remaining collisions $Z_2(\epsilon_{qs}) = 1$ is the location of the quitting surface, where the gas undergoes the transition to the free molecular flow regime. Figure 7.11 **(a)** shows the remaining collisions during the expansion assuming $d_{\mathrm{ap}} = 3\,\mathrm{mm}$ and a constant collision cross section of $1.6 \cdot 10^{-14}\,\mathrm{cm}^{-2}$. Here one can see that most of the collisions happen in the first few mm behind the cell exit, and that the collision rate rapidly falls with increasing distance.

Figure 7.11 **(b)** shows the location of the quitting surface following this simple model for the same parameters. Behind the quitting surface we do not expect the molecules entrained inside the helium flow to experience further cooling or acceleration (longitudinal or transverse) during the expansion. The results agree reasonably well with the measurements done in [103], where hydrodynamic effects like rotational cooling and transverse acceleration were measured to be present in the expansion of ^{88}Sr^{19}F up to 15 mm behind a $d_{\mathrm{ap}} = 3\,\mathrm{mm}$ aperture of a buffer gas cell.

At the location of the quitting surface the Mach number $\mathcal{M}_a$ can be calculated and gives the final velocity distribution of ^{4}He[3].

7.2.3. Velocity Slip

Finally we are interested in the velocity of the molecules which are entrained in the buffer gas flow. If we follow the quitting surface model from the foregoing paragraph and assume that ^{39}K is fully entrained and thermalized ($w_{\mathrm{K}} = w_{\mathrm{He}}$ and $T_{\mathrm{K}} = T_{\mathrm{He}}$) with the buffer gas, we can calculate the final velocity distribution given at the freezing surface of ^{39}K too.

Figure 7.12 shows the dependence of the peak velocity of ^{39}K following that model in red together with the measurements we took. The graph shows qualitative agreement with the measurements in the sense that there is an increase in velocity for higher flow rates and that the effect of acceleration saturates for high flow rates, in agreement to previous measurements from other experiments [44, 104, 17]. Still the absolute values obtained from this model predict a much higher acceleration than it is observed in the experiment.

The location of the freezing surface and therefore the final velocity distribution is dependent on the collisional cross section $\sigma_{\text{K-He}}$ which it is not well known. It is possible to fit certain regions of the flow rate with $\sigma_{\text{K-He}}$ as a free parameter, but we were unable to fit the model to the whole data. Additionally the diffusion inside the buffer gas cell do not agree with

[3]The sudden freeze model is known to give inexact results for the expansion of ^{4}He as quantum dynamical effects alter the ^{4}He-^{4}He cross section $\sigma_{\text{He-He}}$ shifting the freezing surface further away from the aperture leading to even colder beams when expected from this model [18, 112]. Still we are interested in the entrainment of ^{39}K and due to the heavier mass, and therefore the shorter de Broglie wavelength of ^{39}K we do not expect these effect to be that pronounced for the $\sigma_{\text{K-He}}$ cross section.

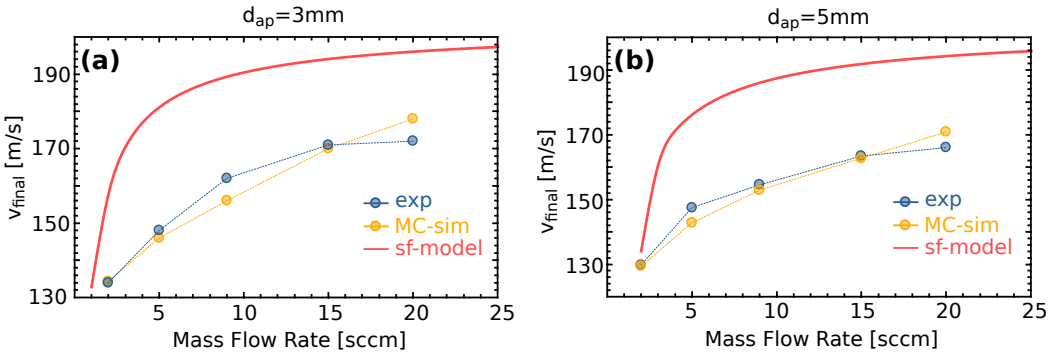

Figure 7.12.: Most probable velocity measured in the experiment (blue circles) for **(a)** an aperture with 3 mm diameter and **(b)** with 5 mm. The red line shows the calculated velocity after the sudden freeze model if full entrainment and thermalization is assumed. The orange circles show the most probable velocity obtained by a Monte Carlo simulation of ^{39}K in the calculated ^{4}He flow field leading to a velocity slip due to the higher mass of ^{39}K and the relatively low number of collisions in the expansion.

the collisional cross sections obtained from such fits. Another drawback of this model is that the predicted translational temperatures are much lower than the ones observed in the experiment.

In hindsight this is not as surprising since the number of collisions in the expansion is quite low. For a flow rate of $\mathcal{F} = 9\,\text{sccm}$ the model predicts that the remaining number of collisions behind the aperture is $N = 14$. Remember that for thermalization of ^{39}K with ^{4}He a characteristic number of $\kappa_\text{K} \approx 6$ is needed due to the higher mass of ^{39}K. Additionally the low number of collisions is not enough to accelerate the ^{39}K leaving the cell at around $v_p = 118\,\text{m}\,\text{s}^{-1}$ to the values obtained from the freezing surface model ($v_p = 189\,\text{m}\,\text{s}^{-1}$).

The result of this should be a velocity and a temperature slip, known from the expansion of binary gas mixtures [18] at room temperature, where ^{39}K is not in thermal equilibrium with its surrounding buffer gas when the transition to free molecular flow takes place.

7.2.4. Toy Model for the Entrainment Process

The low number of collisions gives us the opportunity to build a simple toy model to predict the velocity distribution of ^{39}K by a Monte Carlo simulation. In Figure 7.12 the results of a simplified two dimensional hard disk model are shown in orange. It is assumed that the molecular species at the aperture follows the longitudinal velocity distribution given by the drifted Maxwell Boltzmann distribution with $w_{\text{ap}\parallel} = 102\,\text{m}\,\text{s}^{-1}$ and $T_{\text{ap}\parallel} = 3\,\text{K}$ and a transverse distribution with $w_{\text{ap}\perp} = 0\,\text{m}\,\text{s}^{-1}$ and $T_{\text{ap}\perp} = 3\,\text{K}$. We then let the ^{39}K collide with ^{4}He atoms randomly chosen from the corresponding ^{4}He velocity distribution at distance ϵ behind the aperture. Slower moving potassium atoms need longer to move the same distance as faster moving ^{39}K atoms and therefore collide more often with the ^{4}He buffer gas, which we take into account in the simulation. The simulation is done for 2000 ^{39}K atoms and a histogram of the final distribution is plotted as shown in figure 7.13. Here the simulation shows good agreement with the measured distributions. Showing that the physical interpretation of a hydrodynamic free jet expansion of ^{4}He described by the sudden freeze model and a velocity slip due to the low number of collisions and the higher mass of ^{39}K seem to be a valid picture for the expansion process of a buffer gas beam source. We think the velocity slip model to be physical and that it gives the correct picture of the entrainment process of a heavier species in the expanding ^{4}He. Unfortunately we were unable to measure the beam properties at flow rates $\mathcal{F} > 20\,\text{sccm}$ up to now due to massive beam attenuation for higher flow rates. The reason for this is probably back-scattered ^{4}He from the 4 K stage or background ^{4}He gas which builds up in our chamber at higher flow rates.

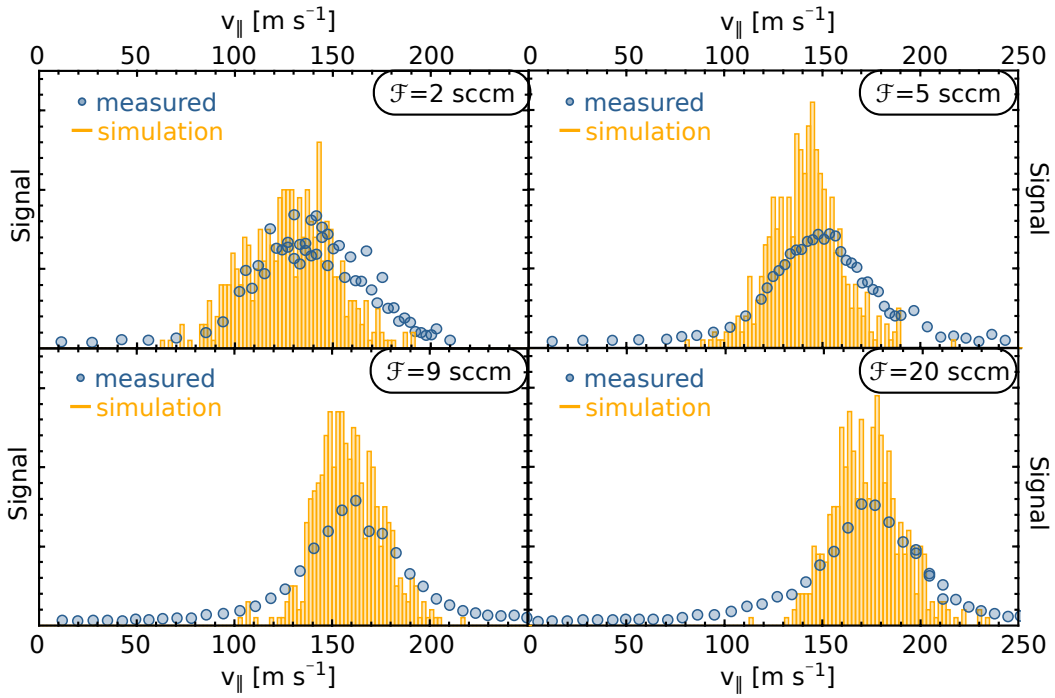

Figure 7.13.: Measured velocity distributions for different flow rates $\mathcal{F}$ (blue circles). In orange a histogram of the simulated distribution is shown. The areas under all curves have been normed, so that the difference in extraction efficiency is not depicted here.

Further improvement of the simulation might be accomplished by doing a full three-dimensional Monte Carlo simulation and the implementation of the temperature dependence of $\sigma_{\text{K-He}}$. Still at least the ^{4}He-^{4}He cross section is known to differ a lot from classical calculations due to quantum mechanical effects [112]. And as we did not find any literature about the temperature dependence of the ^{39}K-^{4}He cross section, we decided to not further pursue the path of even more careful implementation of the Monte Carlo simulation.

7.3. Conclusion

An experimental apparatus has been set up from scratch reaching a base temperature of $T = 3.2\,\text{K}$. Due to the implementation of charcoal cryopumps the apparatus holds a background pressure during operation which rises only by $10^{-7}\,\text{mbar}\,\text{sccm}^{-1}$ fulfilling the requirements for upcoming experiments. The apparatus provides enough optical access for a thorough beam characterization and can readily be equipped with other precursor targets for the production of cold and slow molecular beams.

We used CFD simulations for the ^{4}He flow to understand the appearance of vortices in the used cell geometry and verified that the placement of a diffuser effectively reduces vortices in the simulations. Indeed our measurements show no sign of vortices as the decays of the ^{39}K signals behind the buffer gas cell can be described by a single exponential decay [104].

We measured the extraction characteristics and found that a simple scalar transport model gives good agreement in terms of extraction characteristics and the decay of the pulsed ^{39}K signals. We found a ^{39}K-^{4}He scattering cross section of $2.35 \cdot 10^{-14}\,\text{cm}^{-2}$ with this model. We could not predict the temporal shape of the molecular pulses by this simple model as the initial heating associated with the ablation pulse is not taken into account. Therefore we argue that a better simulation could possibly be implemented by taking into account the temperature dependence of the diffusion coefficient leading to higher diffusion in the

first few ms after the ablation. We qualitatively simulated the effect of the ablation pulse on the ^{4}He flow field by initializing a small region with high pressure and temperature at the target surface and simulated the effects on the flow field. Thereby we could give a reasonable description of the often apparent multiple peak structures in buffer gas cells, which we described by the advection of ablated material in the pressure wave released from the ablation process.

The molecular beam formation process has been described by a combination of the sudden freeze model for the ^{4}He flow and a velocity slip model. Two dimensional Monte Carlo simulations of a hard disk gas have been found to give good agreement of the entrainment of ^{39}K inside the ^{4}He flow field after the nozzle. The model already gave good results for two different nozzle diameters without an adjustment of the ^{39}K-^{4}He scattering cross section.

7.3.1. Subsequent Source Improvement

During the writing of this thesis three versions of the buffer gas cell have already been tested. Here we only want to quickly mention the first observations. The three cell geometries used up to now are summarized in table 7.2.

Using extracted atom number N as a benchmark, we can summarize $N_{\text{Version a}} < N_{\text{Version b}} < N_{\text{Version c}}$. And for the time τ which passes until all extracted particles leave the cell $\tau_{\text{Version a}} > \tau_{\text{Version b}} > \tau_{\text{Version c}}$. The velocity distributions measured are similar showing the same boost in velocity and all show full thermalization of the ^{39}K extracted, $T_{\parallel} \approx 3\,\text{K}$. The best cell for our experiment aiming for a high intensity beam is therefore version c up to now. We therefore deduce that a smaller cell geometry with an even faster extraction would lead to an even higher signals. We already built a second version of the buffer gas cell briefly described in the following section. From the transverse absorption data we estimate the number of molecules extracted from the buffer gas cell (Version c) traveling at transverse velocities near $v_{\perp} = 0\,\text{m}\,\text{s}^{-1}$, such that they absorb light from the detection laser, to be $N \approx 1.5 - 3 \cdot 10^{11}\text{pulse}^{-1}$.

	d_{ap}	Extension	Diffuser
Version a	3 mm	✓	✓
Version b	3 mm	×	✓
Version c	5 mm	×	✓

Table 7.2.: Different versions of the buffer gas cell implemented in the laboratory up to now.

7.3.2. Second Version of the CBGB

We designed a second version of the geometry of our buffer gas beam source shown in Fig. 7.14. The cell is smaller in its inner volume having a main bore of 16 mm in diameter, therefore it should lead to faster extraction of the molecules, minimizing the loss inside the cell.

We additionally put some thought into the guiding of the ^{4}He flow. A diffuser is placed such that the flow field is smooth over the entire cell volume. The cell has a cone shaped nozzle guiding more particles through the aperture. Such a shape was seen in [113] to increase the flow of cold molecules in a capillary loaded buffer gas beam source, but the same arguments drawn there should be applicable for a laser ablation loaded source.

Another effect we want to investigate is the positioning of the target inside the cell. Therefore the cell has two mounts for the precursor target. One at the side as before and one

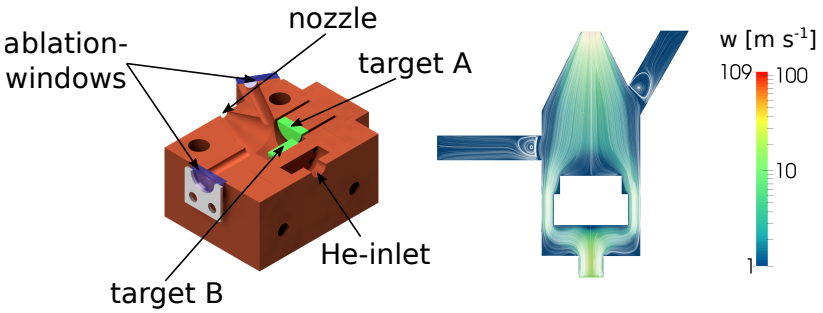

Figure 7.14.: Second version of the buffer gas beam source together with the corresponding flow simulation. The cell comprises two target mounts to investigate the effect on the extraction signal of the ablation point and the initial momentum of the ablated material, which for mount A is perpendicular and for B into the direction of the ^{4}He flow.

placed on the diffuser itself. Regarding the flow lines of the initial helium flow the mounting on the diffuser should be beneficial as an expanding helium plume from the surface of the target would be transversely constraint by the ^{4}He flow which has velocity components aiming at the center line of the buffer gas cell. A similar geometry was used in [114] where the particles of interest were introduced in the center of an expanding carrier gas and an increase in intensity on the center beam line was observed.

Another effect which could be beneficial is that the main momentum of the expanding ablation plume is perpendicular to the target surface. When the ablation takes place on the target placed on the side the particles have to be "carried around a corner" by the buffer gas, whereas the ablation plume of the target on the diffuser mount already has the "correct" direction. The cell provides optical access for both ablation points.

After leaving the cell the molecules are not only accelerated in the longitudinal direction but the expansion does also lead to an increased transverse velocity spread as the pressure directly behind the nozzle is larger than the background pressure. The nozzle is then said to be underexpanded. The increase of transverse velocity during the first few cm behind the cell has already been measured in [44] to lead to transverse velocity distributions characterized by full width at half maximum of $\Delta v_\perp \approx 75 - 120\,\mathrm{m\,s^{-1}}$ and decreases the achieved beam brightness. When the expansion is guided in a diverging nozzle up until the point of the freezing surface we expect no further transverse expansion. Then the transverse velocity distribution would be limited by the temperature T_{ex} reached during the expansion which should lie between the temperature of the cell body of $T_{\mathrm{Cell}} \approx 4\,\mathrm{K}$ and the temperature the sudden freeze model predicts at the freezing surface $T_{\mathrm{SF}} \approx 1\,\mathrm{K}$ leading to transverse velocity spreads between $\Delta v_\perp \approx 28 - 56\,\mathrm{m\,s^{-1}}$.

Therefore a 12° half cone nozzle has been built, which can be optionally used to give the cell a converging-diverging nozzle shape similar to a de Laval nozzle. It is expected that this nozzle shape leads to a more collimated molecular beam at the cost of an increased longitudinal velocity. Such nozzles have already been used to increase the beam brightness of beams produced in supersonic expansion sources and rocket engine nozzles. We want to investigate the impact and possible benefits on a cryogenic buffer gas beam source.

Depending on our findings with this cell we want to decide on a final geometry for a chemical source for CaF. Here solid Ca is ablated and a small amount of SF_6 is applied through a tube to the cell. This kind of source is seen to give more constant pulses with less ablation energy and easier maintenance [115].

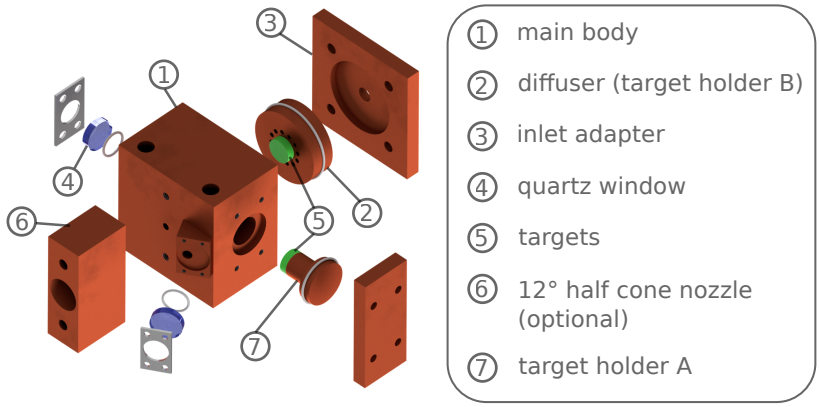

Figure 7.15.: Explosion view of the second version of the buffer gas beam source. We prepared an additional 12° half cone nozzle which can be optionally attached to the buffer gas cell leading to a converging-diverging nozzle shape similar to a de Laval nozzle and might help to collimate the molecular beam.

8

Outlook

During this thesis a type-II Zeeman slowing scheme for the purpose of molecular beam slowing has been developed. Simulations of the slowing process for the example molecules $^{40}Ca^{19}F$ and $^{88}Sr^{19}F$ show efficient deceleration and compression of the one dimensional velocity distribution into a narrow final velocity peak at slow velocities.

An atomic test experiment has been set up, realizing type-II Zeeman slowing on the D_1-line of ^{39}K. The obtained results are comparable to a traditional type-I Zeeman slower implemented in the same setup and the new scheme outperforms white-light slowing by a factor of 20 in our setup. The differences in the slowing result have been described and complemented with Monte Carlo simulations of the slowing processes.

A cryogenic buffer gas beam apparatus has been designed and implemented in the laboratory. The longitudinal velocity distributions have been measured showing a translational temperature of $T_{\parallel} \approx 3\,\mathrm{K}$ at longitudinal velocities centered at $v_{\parallel} \approx 150\,\mathrm{m\,s^{-1}}$.

We used CFD-simulations to understand the appearance of vortices in the buffer gas flow field and how they can be circumvented. A scalar transport model has been used to describe the extraction characteristics showing good agreement with the long term decay of the measured ^{39}K signals. An explanation for multi-peak structures in the molecular pulses has been proposed describing the structures as a result from the hydrodynamic expansion of the ablated material and the resulting disturbance in the buffer gas flow field. Good agreement for the measured velocity distributions has been found by a hydrodynamic description of the beam formation process in the binary gas mixture by the sudden freeze model with an additional velocity slip.

8.1. Towards Zeeman Slowing of $^{40}Ca^{19}F$

The cryogenic buffer gas beam source built during this thesis can readily be used to produce cold beams of $^{40}Ca^{19}F$ by only changing the molecular precursor target to $^{40}Ca^{19}F_2$.

The coil used for Zeeman slowing is currently constructed and has the same design as the one used in chapter 5. The length of the coil is planned to be $l \approx 0.6\,\mathrm{m}$. The magnetic offset field is designed to be around $B_0 = 300 - 400\,\mathrm{G}$, whereas the increasing Zeeman field has an amplitude of $\Delta B = 100 - 200\,\mathrm{G}$. Behind the slowing region we plan to use a two color magneto-optical trap [54] to capture the molecules. After a subsequent sub-Doppler cooling stage the molecules could then be loaded into an optical dipole trap to study either sympathetic cooling by adding an atomic species or to investigate evaporative cooling using the schemes proposed in [62, 29, 30].

We use several diode laser systems at 995 nm, 1057 nm and 1056 nm amplified by tapered

amplifier systems to 3 W, 2 W and 2 W respectively. Then we want to use sum frequency generation (SFG) with light at 1550 nm provided by a commercial fiber laser system[1] ($P_{1550} = 15\,\mathrm{W}$) to produce the necessary light at $\mathcal{L}_{00} = 606\,\mathrm{nm}$, $\mathcal{L}_{01} = 628.5\,\mathrm{nm}$ and $\mathcal{L}_{12} = 628\,\mathrm{nm}$ respectively. Splitting the 1550 nm light with a ratio of $7:7:1$ to the respective SFG and taking into account to loose 50 % of the light from the tapered amplifiers through fiber coupling and the expected conversion efficiencies of the crystals, we estimate to produce $P_{00} \approx 1-1.5\,\mathrm{W}$, $P_{01} \approx 0.7-1\,\mathrm{W}$ and $P_{12} \approx 120\,\mathrm{mW}$ at the desired wavelengths. To frequency lock the lasers we stabilize a scanning cavity by a software lock to the D_1-line of ^{39}K. We then want to use the cavity to transfer the stability of the ^{39}K laser system onto the lasers $\mathcal{L}_{00}, \mathcal{L}_{01}$ and $\mathcal{L}_{12}$.

As soon as we have stable production of light at $\mathcal{L}_{00} = 606\,\mathrm{nm}$ we will change the molecular precursor target of the CBGB to $^{40}Ca^{19}F_2$ and start first spectroscopic measurements.

8.2. Dreams for the Future

A Chemical Beam Source of $^{40}Ca^{19}F$

Since type-II Zeeman slowing is dissipative and allows a continuous loading of a subsequent trap, further improvements are expected by continuous buffer gas beam sources. In the short to medium term we want to change the molecule production from ablation of CaF to an ablation of Ca while a small amount of SF_6 is added to the CBGB through a second fill line [115]. This kind of molecule production is known to have less shot to shot noise from the ablation process.

This could be a first step towards a quasi continuous source of cold $^{40}Ca^{19}F$. It might be possible to focus a continuous wave (cw) laser onto the Ca-rod inside the buffer gas cell to vaporize Ca, instead of a short ablation pulse. In [116] a quasi continuous neon buffer gas source of cold ThO was implemented using the chemical reaction $ThO_2 + Th \rightarrow 2ThO$ in a vaporization induced by a cw-laser. The source produced molecular pulses with pulse widths up to 100 ms and an increase of the molecule number per pulse of one order of magnitude in comparison to a laser ablation loaded source was observed. The power of the vaporization laser is limited by the heat load the cryogenic head tolerates while holding its base temperature. The usage of neon at $T \approx 18\,\mathrm{K}$ as a buffer gas is favorable here, our cryogenic head can hold this base temperature up to heat loads of $\approx 20\,\mathrm{W}$.

The reaction $Ca + SF_6 \rightarrow CaF + SF_5$ is endoergic [117] but the chemical reaction cross section with SF_6 of Ca in a metastable state (^{3}P) can be much larger than for Ca in the ground state (^{1}S) [118, 119, 120]. Therefore it might be favorable to optically pump Ca for an efficient molecule production.

Magnetic Guiding

The biggest loss during radiative slowing is transverse spreading due to initial transverse velocity components and the transverse heating during the slowing process. Molecules slowed below $10\,\mathrm{m\,s^{-1}}$ reaching the trapping region are simulated to have only transverse velocity components below $v_\perp < 0.4\,\mathrm{m\,s^{-1}}$ for type-II Zeeman slowing. As the transverse losses scale quadratically with $v_\perp$ even transverse guiding schemes with potential depths in the $\mathrm{m\,s^{-1}}$ range have the potential to increase the flux at the trapping region considerably.

The principle of type-II Zeeman slowing with an increasing magnetic field ensures that most particles are rapidly pumped into low field seeking states $m_J = +1/2$ in a magnetic field $\mathcal{L}_{\mathrm{rep}}$ and stay there until they are shifted into resonance with $\mathcal{L}_{\mathrm{sl}}$. This gives the possibility to magnetically guide the particles to the trapping region to minimize transverse losses. For

[1] Koheras BOOSTIK

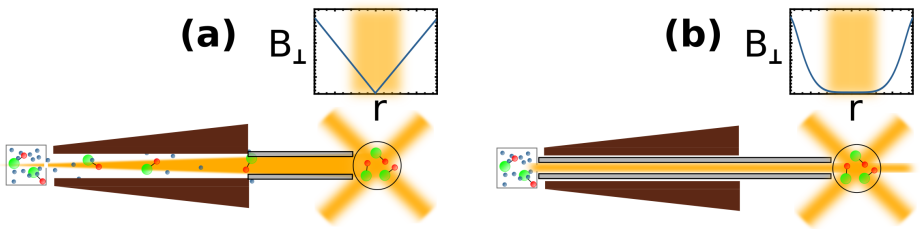

Figure 8.1.: Possible magnetic guiding configurations which are under investigation for implementation in the experiment. In **(a)** the molecules are guided after the slowing, minimizing the loss after the slowing process due to transverse spreading. In **(b)** the molecules are guided along the whole slowing path, here it has to be taken care that the transverse magnetic guiding field does not disturb the longitudinal Zeeman field. This may be possible by using a higher order multipole guide, for example a dodecapole which has vanishing magnetic field values near the center line where the slowing lasers are present as it is shown in the inset.

transverse magnetic guiding schemes it has to be ensured that the guiding fields do not shift the molecules into resonance with the slowing lasers $\mathcal{L}_{\mathrm{sl}}$, as this can lead to unwanted further deceleration or even deceleration to a standstill. Behind the solenoid a guide with depth of $2\,\mathrm{m\,s^{-1}}$ corresponding to $B_{\perp} \approx 200\,\mathrm{G}$ can be implemented straightforward as $\mathcal{L}_{\mathrm{sl}}$ is only resonant for slowed molecules for magnetic fields $B > 500\,\mathrm{G}$. Inside the solenoid the situation is different as the longitudinal field shifts $\mathcal{L}_{\mathrm{sl}}$ nearer to resonance for all velocity classes such that already small transverse guiding fields would disturb the slowing process. This problem could potentially be circumvented by using a high order multipole guide, for example a dodecapole as it is shown in the inset of 8.1**(b)**. This has vanishing field values near to its center line where $\mathcal{L}_{\mathrm{sl}}$ provides strong deceleration forces. As soon as a molecule leaves the region of high intensity of $\mathcal{L}_{\mathrm{sl}}$ it feels a strong transverse magnetic field gradient and is pushed back to the center line.

Bibliography

[1] Lincoln D. Carr, David DeMille, Roman V. Krems, and Jun Ye. Cold and ultracold molecules: science, technology and applications. *New Journal of Physics*, 11(5):055049, 2009.

[2] M. A. Baranov, M. Dalmonte, G. Pupillo, and P. Zoller. Condensed Matter Theory of Dipolar Quantum Gases. *Chemical Reviews*, 112(9):5012–5061, 2012.

[3] John L. Bohn, Ana Maria Rey, and Jun Ye. Cold molecules: Progress in quantum engineering of chemistry and quantum matter. *Science*, 357(6355):1002–1010, 2017.

[4] N. Balakrishnan. Perspective : Ultracold molecules and the dawn of cold controlled chemistry. *The Journal of Chemical Physics*, 145(15):150901, 2016.

[5] S. Ospelkaus, K.-K. Ni, D. Wang, M. H. G. de Miranda, B. Neyenhuis, G. Quemener, P. S. Julienne, J. L. Bohn, D. S. Jin, and J. Ye. Quantum-State Controlled Chemical Reactions of Ultracold Potassium-Rubidium Molecules. *Science*, 327(5967):853–857, 2010.

[6] D. DeMille. Quantum Computation with Trapped Polar Molecules. *Phys. Rev. Lett.*, 88(6):067901, January 2002.

[7] J. Baron, W. C. Campbell, D. DeMille, J. M. Doyle, G. Gabrielse, Y. V. Gurevich, P. W. Hess, N. R. Hutzler, E. Kirilov, I. Kozyryev, B. R. O Leary, C. D. Panda, M. F. Parsons, E. S. Petrik, B. Spaun, A. C. Vutha, and A. D. West. Order of Magnitude Smaller Limit on the Electric Dipole Moment of the Electron. *Science*, 343(6168):269–272, 2014.

[8] William B. Cairncross, Daniel N. Gresh, Matt Grau, Kevin C. Cossel, Tanya S. Roussy, Yiqi Ni, Yan Zhou, Jun Ye, and Eric A. Cornell. Precision Measurement of the Electron's Electric Dipole Moment Using Trapped Molecular Ions. *Phys. Rev. Lett.*, 119(15):153001, October 2017.

[9] J. J. Hudson, D. M. Kara, I. J. Smallman, B. E. Sauer, M. R. Tarbutt, and E. A. Hinds. Improved measurement of the shape of the electron. *Nature*, 473:493, May 2011.

[10] J.S.M. Ginges and V.V. Flambaum. Violations of fundamental symmetries in atoms and tests of unification theories of elementary particles. *Physics Reports*, 397(2):63–154, July 2004.

[11] P. G. H. Sandars. Measurability of the Proton Electric Dipole Moment. *Phys. Rev. Lett.*, 19(24):1396–1398, December 1967.

[12] Emine Altuntas, Jeffrey Ammon, Sidney B. Cahn, and David DeMille. Demonstration of a Sensitive Method to Measure Nuclear-Spin-Dependent Parity Violation. *Phys. Rev. Lett.*, 120(14):142501, April 2018.

[13] Emine Altuntas, Jeffrey Ammon, Sidney B. Cahn, and David DeMille. Measuring nuclear-spin-dependent parity violation with molecules: Experimental methods and analysis of systematic errors. *Phys. Rev. A*, 97(4):042101, April 2018.

[14] S. Ospelkaus, A. Peer, K.-K. Ni, J. J. Zirbel, B. Neyenhuis, S. Kotochigova, P. S. Julienne, J. Ye, and D. S. Jin. Efficient state transfer in an ultracold dense gas of heteronuclear molecules. *Nature Physics*, 4:622, June 2008.

[15] K.-K. Ni, S. Ospelkaus, D. J. Nesbitt, J. Ye, and D. S. Jin. A dipolar gas of ultracold molecules. *Phys. Chem. Chem. Phys.*, 11(42):9626–9639, 2009.

[16] Wesley C. Campbell, Edem Tsikata, Hsin-I Lu, Laurens D. van Buuren, and John M. Doyle. Magnetic Trapping and Zeeman Relaxation of NH ($X\text ^3\ensuremath\Sigma^\ensuremath-$). *Phys. Rev. Lett.*, 98(21):213001, May 2007.

[17] Nicholas R. Hutzler, Hsin-I Lu, and John M. Doyle. The Buffer Gas Beam: An Intense, Cold, and Slow Source for Atoms and Molecules. *Chemical Reviews*, 112(9):4803–4827, 2012.

[18] H. Pauly. *Atom, Molecule, and Cluster Beams I.* Springer.

[19] Hendrick L. Bethlem and Gerard Meijer. Production and application of translationally cold molecules. *International Reviews in Physical Chemistry*, 22(1):73–128, January 2003.

[20] Edvardas Narevicius, Adam Libson, Christian G. Parthey, Isaac Chavez, Julia Narevicius, Uzi Even, and Mark G. Raizen. Stopping Supersonic Beams with a Series of Pulsed Electromagnetic Coils: An Atomic Coilgun. *Phys. Rev. Lett.*, 100(9):093003, March 2008.

[21] N J Fitch and M R Tarbutt. Principles and Design of a Zeeman Sisyphus Decelerator for Molecular Beams. *Chemphyschem*, 17(22):3609–3623, November 2016.

[22] Eric R. Hudson. Deceleration of continuous molecular beams. *Phys. Rev. A*, 79(6):061407, June 2009.

[23] S. Chervenkov, X. Wu, J. Bayerl, A. Rohlfes, T. Gantner, M. Zeppenfeld, and G. Rempe. Continuous Centrifuge Decelerator for Polar Molecules. *Phys. Rev. Lett.*, 112(1):013001, January 2014.

[24] J.E. van den Berg, S.C. Mathavan, C. Meinema, J. Nauta, T.H. Nijbroek, K. Jungmann, H.L. Bethlem, and S. Hoekstra. Traveling wave deceleration of SrF molecules. *Spectroscopic Tests of Fundamental Physics*, 300:22–25, June 2014.

[25] Sreekanth C. Mathavan, Artem Zapara, Quinten Esajas, and Steven Hoekstra. Deceleration of a Supersonic Beam of SrF Molecules to. *ChemPhysChem*, 17(22):3709–3713, October 2016.

[26] M. Zeppenfeld, M. Motsch, P. W. H. Pinkse, and G. Rempe. Optoelectrical cooling of polar molecules. *Phys. Rev. A*, 80(4):041401, October 2009.

[27] Alexander Prehn, Martin Ibruegger, Rosa Gloeckner, Gerhard Rempe, and Martin Zeppenfeld. Optoelectrical Cooling of Polar Molecules to Submillikelvin Temperatures. *Phys. Rev. Lett.*, 116(6):063005, February 2016.

[28] Lawrence W. Cheuk, LoÃ¯c Anderegg, Benjamin L. Augenbraun, Yicheng Bao, Sean Burchesky, Wolfgang Ketterle, and John M. Doyle. Lambda-Enhanced Imaging of Molecules in an Optical Trap. *Phys. Rev. Lett.*, 121(8):083201, August 2018.

[29] Goulven Quemener and John L. Bohn. Shielding 2sigma ultracold dipolar molecular collisions with electric fields. *Phys. Rev. A*, 93(1):012704, January 2016.

[30] L. Lassabliere and G. Quemener. Controlling the scattering length of ultracold dipolar molecules. *ArXiv e-prints*, June 2018.

[31] Ian C. Lane. Production of ultracold hydrogen and deuterium via Doppler-cooled Feshbach molecules. *Phys. Rev. A*, 92(2):022511, August 2015.

[32] Ian C. Lane. Ultracold fluorine production via Doppler cooled BeF. *Phys. Chem. Chem. Phys.*, 14(43):15078–15087, 2012.

[33] M.D. Di Rosa. Laser cooling molecules - Concept, candidates, and supporting hyperfine-resolved measurements of rotational lines in the A-X band of CaH. *Eur. Phys. J. D*, 31(2):395–402, 2004.

[34] Ivan Kozyryev, Louis Baum, Kyle Matsuda, Benjamin L. Augenbraun, Loic Anderegg, Alexander P. Sedlack, and John M. Doyle. Sisyphus Laser Cooling of a Polyatomic Molecule. *Phys. Rev. Lett.*, 118(17):173201, April 2017.

[35] Kozyryev Ivan, Baum Louis, Matsuda Kyle, and Doyle John M. Proposal for Laser Cooling of Complex Polyatomic Molecules. *ChemPhysChem*, 17(22):3641–3648.

[36] Benjamin K. Stuhl, Brian C. Sawyer, Dajun Wang, and Jun Ye. Magneto-optical Trap for Polar Molecules. *Phys. Rev. Lett.*, 101(24):243002, December 2008.

[37] Gerhard Herzberg. *Molecular Spactra and Molecular Structure I. Spectra of Diatomic Molecules*. D. Van Nostrand Company, Inc., Princeton, New Jersey, second edition, eigth printing edition, 1939.

[38] D. J. Berkeland and M. G. Boshier. Destabilization of dark states and optical spectroscopy in Zeeman-degenerate atomic systems. *Phys. Rev. A*, 65(3):033413, February 2002.

[39] J. F. Barry, E. S. Shuman, E. B. Norrgard, and D. DeMille. Laser Radiation Pressure Slowing of a Molecular Beam. *Phys. Rev. Lett.*, 108(10):103002, March 2012.

[40] S. Truppe, H. J. Williams, N. J. Fitch, M. Hambach, T. E. Wall, E. A. Hinds, B. E. Sauer, and M. R. Tarbutt. An intense, cold, velocity-controlled molecular beam by frequency-chirped laser slowing. *New Journal of Physics*, 19(2):022001, 2017.

[41] S. Truppe, H. J. Williams, M. Hambach, L. Caldwell, N. J. Fitch, E. A. Hinds, B. E. Sauer, and M. R. Tarbutt. Molecules cooled below the Doppler limit. *arXiv preprint arXiv:1703.00580*, 2017.

[42] Loic Anderegg and et. al. Radio Frequency Magneto-Optical Trapping of CaF with High Density. *arXiv preprint arXiv:1705.10288*, 2017.

[43] Loic Anderegg, Benjamin L. Augenbraun, Yicheng Bao, Sean Burchesky, Lawrence W. Cheuk, Wolfgang Ketterle, and John M. Doyle. Laser cooling of optically trapped molecules. *Nature Physics*, June 2018.

[44] J. F. Barry, E. S. Shuman, and D. DeMille. A bright, slow cryogenic molecular beam source for free radicals. *Physical Chemistry Chemical Physics*, 13(42):18936–18947, 2011.

[45] Mark Yeo, Matthew T. Hummon, Alejandra L. Collopy, Bo Yan, Boerge Hemmerling, Eunmi Chae, John M. Doyle, and Jun Ye. Rotational State Microwave Mixing for Laser Cooling of Complex Diatomic Molecules. *Phys. Rev. Lett.*, 114(22):223003, June 2015.

[46] Boerge Hemmerling, Eunmi Chae, Aakash Ravi, Loic Anderegg, Garrett K. Drayna, Nicholas R. Hutzler, Alejandra L. Collopy, Jun Ye, Wolfgang Ketterle, and John M. Doyle. Laser slowing of CaF molecules to near the capture velocity of a molecular MOT. *Journal of Physics B: Atomic, Molecular and Optical Physics*, 49(17):174001, 2016.

[47] J. F. Barry, D. J. McCarron, E. B. Norrgard, M. H. Steinecker, and D. DeMille. Magneto-optical trapping of a diatomic molecule. *Nature*, 512(7514):286–289, August 2014.

[48] Jun Ye. Exploring a New Frontier of Molecular Structure and Interactions, March 2018.

[49] H. J. Williams, L. Caldwell, N. J. Fitch, S. Truppe, J. Rodewald, E. A. Hinds, B. E. Sauer, and M. R. Tarbutt. Magnetic Trapping and Coherent Control of Laser-Cooled Molecules. *Phys. Rev. Lett.*, 120(16):163201, April 2018.

[50] H. J. Williams, S. Truppe, M. Hambach, L. Caldwell, N. J. Fitch, E. A. Hinds, B. E. Sauer, and M. R. Tarbutt. Characteristics of a magneto-optical trap of molecules. *New Journal of Physics*, 19(11):113035, 2017.

[51] Steinecker Matthew H, McCarron Daniel J, Zhu Yuqi, and DeMille David. Improved Radio-Frequency Magneto-Optical Trap of SrF Molecules. *ChemPhysChem*, 17(22):3664–3669.

[52] J. A. Devlin and M. R. Tarbutt. Three-dimensional Doppler, polarization-gradient, and magneto-optical forces for atoms and molecules with dark states. *New Journal of Physics*, 18(12):123017, 2016.

[53] M. R. Tarbutt. Magneto-optical trapping forces for atoms and molecules with complex level structures. *New Journal of Physics*, 17(1):015007, 2015.

[54] M. R. Tarbutt and T. C. Steimle. Modeling magneto-optical trapping of CaF molecules. *Phys. Rev. A*, 92(5):053401, November 2015.

[55] Matthew T. Hummon, Mark Yeo, Benjamin K. Stuhl, Alejandra L. Collopy, Yong Xia, and Jun Ye. 2d Magneto-Optical Trapping of Diatomic Molecules. *Phys. Rev. Lett.*, 110(14):143001, April 2013.

[56] E. B. Norrgard, D. J. McCarron, M. H. Steinecker, M. R. Tarbutt, and D. DeMille. Submillikelvin Dipolar Molecules in a Radio-Frequency Magneto-Optical Trap. *Phys. Rev. Lett.*, 116(6):063004, February 2016.

[57] H. J. Williams, L. Caldwell, N. J. Fitch, S. Truppe, J. Rodewald, E. A. Hinds, B. E. Sauer, and M. R. Tarbutt. Magnetic trapping and coherent control of laser-cooled molecules. *ArXiv e-prints*, November 2017.

[58] D. J. McCarron, M. H. Steinecker, Y. Zhu, and D. DeMille. Magnetically-Trapped Molecules Efficiently Loaded from a Molecular MOT. *ArXiv e-prints*, December 2017.

[59] Matthias Gempel. *Towards Ultracold Polar NaK Molecules and the Investigation of Dipolar Quantum Gases*. PhD thesis, Leibniz Universitaet Hannover, 2016.

[60] Torben Schulze. *Quantum degenerate mixtures of 23Na - 39K and coherent transfer paths in NaK molecules*. PhD thesis, Leibniz Universitaet Hannover, 2018.

[61] Torben A. Schulze, Torsten Hartmann, Kai K. Voges, Matthias W. Gempel, Eberhard Tiemann, Alessandro Zenesini, and Silke Ospelkaus. Feshbach spectroscopy and dual-species Bose-Einstein condensation of $^23\mathrmNa\text\ensuremath-^39\mathrmK$ mixtures. *Phys. Rev. A*, 97(2):023623, February 2018.

[62] Maykel L. Gonzalez-Martinez, John L. Bohn, and Goulven Quemener. Adimensional theory of shielding in ultracold collisions of dipolar rotors. *Phys. Rev. A*, 96(3):032718, September 2017.

[63] M. Petzold, P. Kaebert, P. Gersema, M. Siercke, and S. Ospelkaus. A Zeeman slower for diatomic molecules. *New Journal of Physics*, 20(4):042001, 2018.

[64] Maurice Petzold, Paul Kaebert, P. Gersema, Timo Poll, Niklas Reinhardt, M. Siercke, and S. Ospelkaus. Type-II Zeeman slowing: Characterization and comparison to conventional radiative beam slowing schemes. *submitted to PRA*, 2018.

[65] Hsin-I Lu, Julia Rasmussen, Matthew J. Wright, Dave Patterson, and John M. Doyle. A cold and slow molecular beam. *Phys. Chem. Chem. Phys.*, 13(42):18986–18990, 2011.

[66] Sebastiaan Y. T. van de Meerakker, Nicolas Vanhaecke, and Gerard Meijer. Stark Deceleration and Trapping of OH Radicals. *Annual Review of Physical Chemistry*, 57(1):159–190, 2006.

[67] Hsin-I Lu, Ivan Kozyryev, Boerge Hemmerling, Julia Piskorski, and John M. Doyle. Magnetic Trapping of Molecules via Optical Loading and Magnetic Slowing. *Phys. Rev. Lett.*, 112(11):113006, March 2014.

[68] K. Esajas, P. Aggarwal, H.L. Bethlem, A. Borschevsky, P. Haase, Y. Hao, S. Hoekstra, K. Jungmann, and T. Meijknecht. Slow molecular beams of heavy diatomic polar molecules to probe T/CP violation, 2018.

[69] M. A. Chieda and E. E. Eyler. Prospects for rapid deceleration of small molecules by optical bichromatic forces. *Phys. Rev. A*, 84(6):063401, December 2011.

[70] A. M. Jayich, A. C. Vutha, M. T. Hummon, J. V. Porto, and W. C. Campbell. Continuous all-optical deceleration and single-photon cooling of molecular beams. *Phys. Rev. A*, 89(2):023425, February 2014.

[71] Ivan Kozyryev, Louis Baum, Leland Aldridge, Phelan Yu, Edward E. Eyler, and John M. Doyle. Coherent Bichromatic Force Deflection of Molecules. *Phys. Rev. Lett.*, 120(6):063205, February 2018.

[72] S. E. Galica, L. Aldridge, D. J. McCarron, E. E. Eyler, and P. L. Gould. Deflection of a molecular beam using the bichromatic stimulated force. *pra*, 98(2):023408, August 2018.

[73] William D. Phillips and Harold Metcalf. Laser Deceleration of an Atomic Beam. *Phys. Rev. Lett.*, 48(9):596–599, March 1982.

[74] Mirco Siercke. The code of the optical Bloch equations and its application to calculate the presented force profiles have been done by Mirco Siercke.

[75] T. E. Wall, J. F. Kanem, J. J. Hudson, B. E. Sauer, D. Cho, M. G. Boshier, E. A. Hinds, and M. R. Tarbutt. Lifetime of the A(v'=0) state and Franck-Condon factor of the A-X(0-0) transition of CaF measured by the saturation of laser-induced fluorescence. *Phys. Rev. A*, 78(6):062509, December 2008.

[76] M. R. Tarbutt, B. E. Sauer, J. J. Hudson, and E. A. Hinds. Design for a fountain of YbF molecules to measure the electron's electric dipole moment. *New Journal of Physics*, 15(5):053034, 2013.

[77] F. Lison, P. Schuh, D. Haubrich, and D. Meschede. High-brilliance Zeeman-slowed cesium atomic beam. *Phys. Rev. A*, 61(1):013405, December 1999.

[78] R. J. Napolitano, S. C. Zilio, and V. S. Bagnato. Adiabatic following conditions for the deceleration of atoms with the Zeeman tuning technique. *Optics Communications*, 80(2):110 – 114, 1990.

[79] Matthew H. Steinecker, Daniel J. McCarron, Yuqi Zhu, and David DeMille. Improved Radio-Frequency Magneto-Optical Trap of SrF Molecules. *ChemPhysChem*, 17(22):3664–3669.

[80] Matthias Gempel. *A Laser system for Cooling and Trapping of K*. Diploma Thesis, TUM, Max Planck Institut fuer Quantenoptik, 2010.

[81] Alexander Franzen. Component Library.

[82] P. Gersema. Ein Kuehllasersystem zum Zeeman-Abbremsen von K-Atomen auf der D1-Linie und erste Kuehlexperimente. Master's thesis, Leibniz Universitaet Hannover, Hannover, 2017.

[83] Paul Kaebert. Frequenzverbreitertes Diodenlasersystem zum Laserkuehlen diatomarer Molekuele. Master's thesis, Leibniz Universitaet Hannover, Hannover, 2016.

[84] P. A. Molenaar, P. van der Straten, H. G. M. Heideman, and H. Metcalf. Diagnostic technique for Zeeman-compensated atomic beam slowing: Technique and results. *Phys. Rev. A*, 55(1):605–614, January 1997.

[85] S. A. Hopkins, K. Butler, A. Guttridge, S. Kemp, R. Freytag, E. A. Hinds, M. R. Tarbutt, and S. L. Cornish. A versatile dual-species Zeeman slower for caesium and ytterbium. *Review of Scientific Instruments*, 87(4):043109, 2016.

[86] E Wille. *Preparation of an optically trapped Fermi-Fermi mixture of 6Li and 40K atoms and characterization of the interspecies interactions by Feshbach spectroscopy*. PhD thesis, Universitaet Innsbruck, 2009.

[87] Eunmi Chae. *Laser Slowing of CaF Molecules and Progress towards a Dual-MOT for Li and CaF*. PhD thesis, Harvard University, Cambridge, Massachusetts, 2015.

[88] David Patterson. *Buffer Gas Cooled Beams and Cold Molecular Collisions*. PhD thesis, Harvard University, 2010.

[89] Sarah Margaretha Skoff. *Buffer gas cooling of YbF molecules*. PhD thesis, Imperial College London, 2011.

[90] Christian Sommer, Laurens D. van Buuren, Michael Motsch, Sebastian Pohle, Josef Bayerl, Pepijn W. H. Pinkse, and Gerhard Rempe. Continuous guided beams of slow and internally cold polar molecules. *Faraday Discuss.*, 142(0):203–220, 2009.

[91] Christian Sommer. *Construction and Operation of a Cryogenic Source for Cold Polar Molecules*. PhD thesis, Max-Planck-Institut fuer Quantenoptik, April 2011.

[92] The OpenFOAM Foundation. OpenFOAM v5 User Guide.

[93] R. deCarvalho, J.M. Doyle, B. Friedrich, T. Guillet, J. Kim, D. Patterson, and J.D. Weinstein. Buffer-gas loaded magnetic traps for atoms and molecules: A primer. *The European Physical Journal D - Atomic, Molecular, Optical and Plasma Physics*, 7(3):289–309, October 1999.

[94] Leonard Benedict Loeb. *The kinetic theory of gases*, volume second edition. McGraw-Hill Book Company.

[95] Nicholas Edward Bulleid. *Slow, cold beams of polar molecules for precision measurements*. PhD thesis, Imperial College London, 2013.

[96] P.J. Linstrom and W.G. Mallard. *NIST Chemistry WebBook, NIST Standard Reference Database Number 69*. Gaithersburg MD.

[97] P. J. Nacher. Viscosity of gaseous 3he and 4he at low temperatures. *The Journal of Chemical Physics*, 101(7):6367–6368, 1994.

[98] Alejandra L. Collopy. *A Three-Dimensional MOT of YO Towards Narrow-Line Cooling*. PhD thesis, University of Colorado, Boulder, 2018.

[99] Jack W. Ekin. *Experimental Techniques for Low-Temperature Measurements*. Oxford University Press, 2006.

[100] M. R. Tarbutt. private communication.

[101] Stefan Truppe. private communication.

[102] Thomas Gantner. private communication.

[103] J. F. Barry. *Laser cooling and slowing of a diatomic molecule*. PhD thesis, Yale University, 2013.

[104] N. E. Bulleid, S. M. Skoff, R. J. Hendricks, B. E. Sauer, E. A. Hinds, and M. R. Tarbutt. Characterization of a cryogenic beam source for atoms and molecules. *Phys. Chem. Chem. Phys.*, 15(29):12299–12307, 2013.

[105] D. B. Spalding. The Molecular Theory of Gases and Liquids.J. O. Hirschfelder, C. F. Curtiss and R. B. Bird. John Wiley,New York. Chapman & Hall, London, 1954. 1,219 pp.Diagrams. 160s. *The Journal of the Royal Aeronautical Society*, 59(531):228–228, 1955.

[106] S. M. Skoff, R. J. Hendricks, C. D. J. Sinclair, J. J. Hudson, D. M. Segal, B. E. Sauer, E. A. Hinds, and M. R. Tarbutt. Diffusion, thermalization, and optical pumping of YbF molecules in a cold buffer-gas cell. *Phys. Rev. A*, 83(2):023418, February 2011.

[107] Nicholas R. Hutzler. *A New Limit on the Electron Electric Dipole Moment: Beam Production, Data Interpretation, and Systematics*. PhD thesis, Harvard University, 2014.

[108] V. N. Lednev, S. M. Pershin, and A. F. Bunkin. Laser Beam Profile Influence on LIBS Analytical Capabilities: Single vs. Multimode Beam. *ArXiv e-prints*, August 2013.

[109] Oleg V. Borisov, Xianglei Mao, and Richard E. Russo. Effects of crater development on fractionation and signal intensity during laser ablation inductively coupled plasma mass spectrometry. *Spectrochimica Acta Part B: Atomic Spectroscopy*, 55(11):1693 – 1704, 2000.

[110] Marcel Guillong, Ingo Horn, and Detlef GÃ¼nther. Capabilities of a homogenized 266Â nm Nd:YAG laser ablation system for LA-ICP-MS. *Journal of Analytical Atomic Spectrometry*, 17(1):8–14, 2002.

[111] Davide Bleiner. *Optimization of a Laser Ablation Inductively Coupled Plasma Mass Spectrometry System for the Detection of Short Transient Signals*. PhD thesis, Technische Hochschule Zuerich, 2002.

[112] J. Peter Toennies and Klaus Winkelmann. Theoretical studies of highly expanded free jets: Influence of quantum effects and a realistic intermolecular potential. *The Journal of Chemical Physics*, 66(9):3965–3979, 1977.

[113] Vijay Singh, Amit K. Samanta, Nils Roth, Daniel Gusa, Tim Ossenbrueggen, Igor Rubinsky, Daniel A. Horke, and Jochen Kuepper. Optimized cell geometry for buffer-gas-cooled molecular-beam sources. *Phys. Rev. A*, 97(3):032704, March 2018.

[114] Victor Varentsov, D.R. Hansevarov, and D.V. Varentsov. The generation of an internal molecular-beam target from expensive gaseous and nonvolatile substances for storage rings. *Nuclear Instruments and Methods in Physics Research Section A: Accelerators, Spectrometers, Detectors and Associated Equipment*, 352:542–547, 1995.

[115] S. Truppe, M. Hambach, S. M. Skoff, N. E. Bulleid, J. S. Bumby, R. J. Hendricks, E. A. Hinds, B. E. Sauer, and M. R. Tarbutt. A buffer gas beam source for short, intense and slow molecular pulses. *Journal of Modern Optics*, 65(5-6):648–656, 2018.

[116] Elizabeth Petrik West. *A Thermochemical Cryogenic Buffer Gas Beam Source of ThO for Measuring the Electric Dipole Moment of the Electron.* PhD thesis, Harvard University, Cambridge, 2017.

[117] E. Verdasco, V. Saez Rabanos, and A. Gonzalez Urena. Reaction Dynamics of Translational and Electronic Excitation In Ca + SF6 Collisions. *Laser Chemistry*, 10(1):51–61, 1989.

[118] J.C. Whitehead. *Selectivity in Chemical Reactions.* Kluwer Academic Publishers, Dordrecht, Boston, London, 1988.

[119] J. M. Doyle. private communication.

[120] Benjamin L. Augenbraun. private communication.

[121] Timo Poll. *Design und Aufbau eines Fluoreszenzdetektionssystems fuer die D2-Linie von K.* Bachelor Thesis, Leibniz Universitaet Hannover, Hannover, 2018.

A

Appendix

A.1. Supplementary Material to the ^{39}K Type-II Zeeman Slowing Experiment

A.1.1. Monte Carlo Simulations

To understand our data we perform three-dimensional Monte Carlo simulations of the slowing process. To reproduce our data we must take into account several experimental parameters, which we found to be crucial to give a good simulation result. Important parameters are the finite beam size and the Gaussian beam profile of the slowing lasers, the power of the slowing lasers and heating due to the spontaneous photon emission. Additionally of importance are the fitted initial velocity distribution, which is given by a slightly boosted Maxwell-Boltzmann distribution. Another effect comes into play at very low velocities. Here, the photon recoil of $\mathcal{L}_{\text{det}}$ itself pushes the atoms out of resonance itself. Then the density measurement in the experiment becomes a flux measurement. We simulate this by assuming that after 750 photon cycles the atoms are accelerated by $750 \cdot v_{\text{rec}} = 10\,\text{m}\,\text{s}^{-1}$ and fall out of resonance with $\mathcal{L}_{\text{det}}$. Taking into account the beam size of $\mathcal{L}_{\text{det}}$ this is the case for atoms traveling with $v \leq \frac{d_{\text{beam}}}{750 \cdot \tau} \approx 150\,\text{m}\,\text{s}^{-1}$. The full geometrical constraints of the experimental apparatus especially the geometrical constraints of the detection region are equally important.

A.1.2. Laser Frequencies for Different Beam Slowing Methods

In Fig. A.1 the position in frequency of the slowing lasers used in the experiments in 5 are shown. In red the transition frequencies of an ^{39}K atom are depicted. The main transitions of ^{39}K leading to a trapping force in a magneto optical trap $4^2S_{1/2}, (F = 2) \rightarrow 4^2P_{3/2}$ are detuned from all slowing lasers by at least 400 MHz in type-II Zeeman slowing.

This is different for white-light slowing. When the atoms are decelerated the $4^2S_{1/2}, (F = 1)$ levels fall out of resonance first and the slowing force stops. This lead to the effect that $\mathcal{L}_{\text{sl}}$ is fully resonant with the $4^2S_{1/2}, (F = 2)$ states. Therefore the trapping forces should be lessened. This is also the reason why we had to use a fluorescence detection scheme for the White-Light slowing measurement, as $\mathcal{L}_{\text{sl}}$ pumps the atoms out of the detection state.

A.1.3. Fluorescence Detection System

The fluorescence detection system used for the white-light slowing measurement was built during a bachelor thesis [121] and is depicted in Fig. A.2 . To measure the low density beam

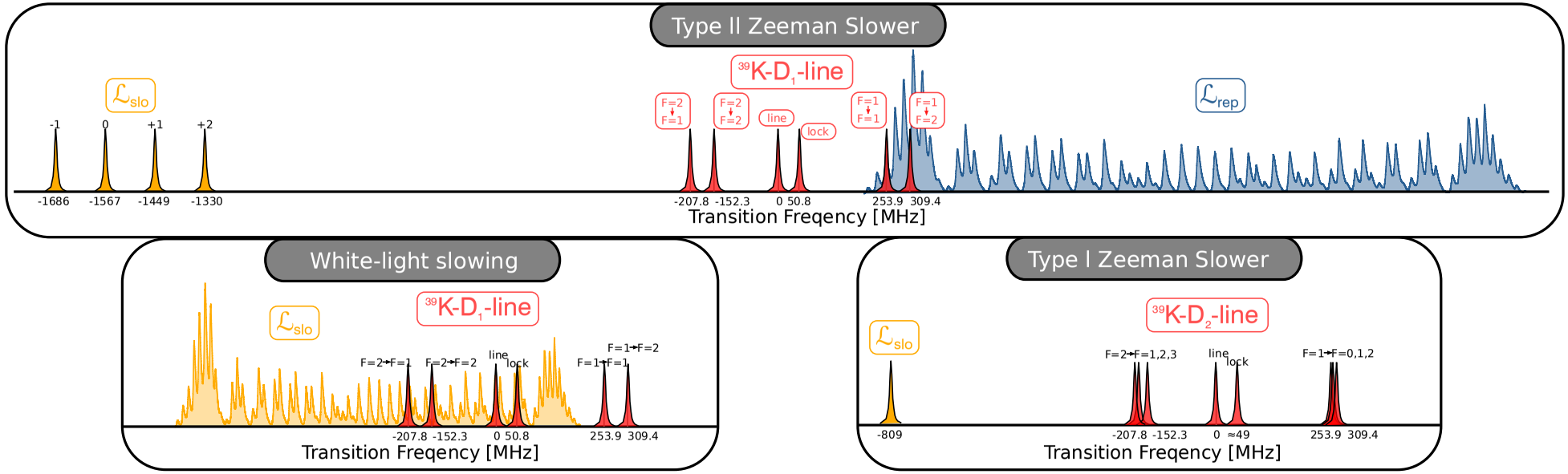

Figure A.1.: Laser frequencies of the different slowing methods together with transition frequencies of ^{39}K atoms at $v = 0\,\mathrm{m\,s^{-1}}$. A velocity component of the atoms counter-propagating to the slowing lasers shifts the transition frequencies to the left in this diagram. Here many circumstances of the slowing and detection process can be seen. For Type II Zeeman slowing the lasers are far detuned from the main transitions driven in a magneto-optical trap. A larger magnetic offset field would shift the frequency components of $\mathcal{L}_{\mathrm{rep}}$ and $\mathcal{L}_{\mathrm{sl}}$ further apart from each other. $\mathcal{L}_{\mathrm{rep}}$ pumps atoms at slow velocities into the $4^2S_{1/2}, F = 2$ state. This is different for white-light slowing as slow atoms are pumped into the $4^2S_{1/2}, F = 1$ state, this is one of the reasons we installed the fluorescence detection for the white-light slowing measurement.

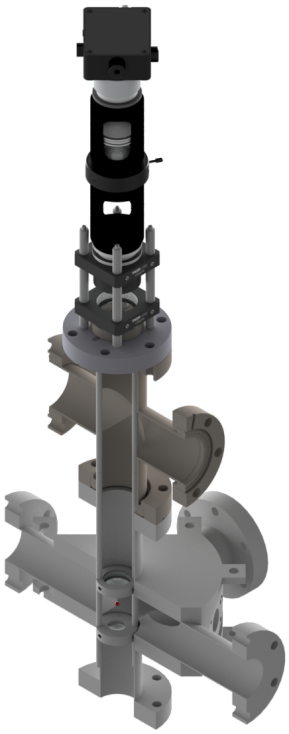

Figure A.2: Fluorescence optics used for the white-light slowing measurement. Inner vacuum optics ensure that a large solid angle of the fluorescent light is captured.

we had to use inner vacuum optics to maximize the solid angle of the fluorescence optics. The light emitted from central point of the vacuum chamber is collimated through a lens, a spherical mirror on the opposite side focuses light emitted in that direction back into the center point so that it is additionally collimated by the lens. Outside of the vacuum chamber is imaged onto a large area photodiode.

A.2. Dipole Forces during the Slowing Process

Here we want to estimate if the optical dipole force is of importance in the radiation pressure beam slowing methods.

The dipole interaction of the particle with the slowing light leads to an AC-Stark shift of the ground and excited states which is intensity dependent. Therefore the transverse intensity distribution of a Gaussian beam profile leads to a dipole potential for the particles in the ground state given by:

$$U_{\mathrm{dip}}(r) = \frac{3\pi c}{2\omega^3} \cdot \frac{\Gamma}{\delta} \cdot I(r) \tag{A.1}$$

where c is the speed of light, ω is the angular frequency of the electronic transition, Γ is the decay rate of the excited state, δ is the detuning from resonance of the applied laser field. Here $I(r)$ is the intensity profile in the transverse direction given by:

$$I(r) = \frac{2P}{\pi w^2} \cdot \exp(\frac{-2r^2}{w^2}) \tag{A.2}$$

where P is the total power of the laser, w is the Gaussian beam waist and r is the distance to the center line of the laser beam. Depending on the sign of the detuning δ the atoms are therefore either pushed to the center line if they see the slowing laser red detuned from their transition frequency $\delta < 0$ or they are pushed away from the center line for blue detunings $\delta > 0$.

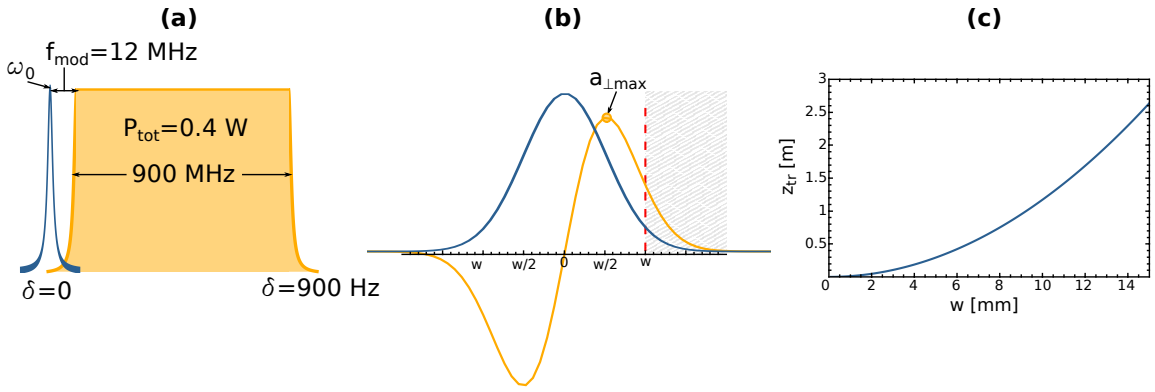

Figure A.3.: **(a)** The dipole force scales with δ^{-1} we therefore define the worst case as shown here where a high power laser is just slightly blue detuned to the transition frequency. **(b)** In blue the dipole potential is shown schematically for a Gaussian beam profile. In orange the corresponding acceleration is shown schematically. **(c)** Distance ^{39}K traveled in this worst case scenario when the longitudinal velocity is $150\,\mathrm{m\,s^{-1}}$.

Typically dipole forces are applied in optical traps with high power focused laser beams far detuned from resonance. While the power of the slowing laser here are typically much lower and they are relatively broad in terms of their Gaussian beam waist. But note that the detuning for radiative beam slowing is $\delta < 1\,\mathrm{GHz}$ whereas the detuning used in optical dipole traps is typically $\delta > 100\,\mathrm{THz}$. This can make the effect sizable again.

Considering type-I Zeeman slowing and chirped light slowing the laser $\mathcal{L}_{sl}$ is always seen slightly red detuned for all velocity classes. Therefore the potential the particles experience results in a force driving the particles to the center line.

This is different for White-light slowing or Type II Zeeman slowing. In white light slowing for example all particles traveling at the capture velocity of the slowing light see the whole frequency spectrum slightly blue detuned. After being slowed it is the other way around and they see most frequency components of the slowing light slightly red detuned.

In Type II Zeeman slowing the situation is even more complicated. When an increasing field configuration is chosen as it is here. Particles see $\mathcal{L}_{\mathrm{rep}}$ blue detuned over the whole slowing path and $\mathcal{L}_{\mathrm{sl}}$ red detuned. Depending on the power and the exact detunings the potential is then either attractive to the center line or repulsive and is additionally dependent on the magnetic field and the velocity of the particle.

To estimate if we have to consider the effect in our experiments we want to give an upper bound for the deflection from the center line when a particle traveling through the light field sees parts of the light blue detuned to its optical transition.

Figure A.3**(a)** shows the situation in frequency space which we defined as the worst case scenario. We assume a two level atom and that a laser broadened to 900 MHz with a modulation frequency of 12 MHz and a total power of $P_{tot} = 0.4\,\mathrm{W}$ lies slightly blue to the resonance frequency. This is the situation found in white light slowing for atoms traveling near the capture velocity which we chose here as $v_{\mathrm{cap}} = 150\,\mathrm{m\,s^{-1}}$. The highest transverse acceleration due to dipolar forces $a_{\perp\mathrm{max}}$ is given at the inflection point of the Gaussian beam profile lying at $w/2$ shown in Fig. A.3**(b)**. As a an upper bound for the deflection we assume the particles feels a constant acceleration of $a_{\perp\mathrm{max}}$ and define the particles lost for the radiative beam slowing process when they are deflected by $w/2$.

Figure A.3**(c)** shows the distance a particle at v=150m/s can travel before being deflected by the aforementioned amount. In our experiment we worked with $w = 10\,\mathrm{mm}$, $P_{\mathrm{tot}} = 0\,4W$. This shows that even in this worst case scenario the effect of a dipolar deflection is still negligible. But note that already beam sizes w of several mm or slowing lasers with several W of power really can have effects and it is therefore worth it to look at the specific system if dipolar effects are still negligible.

A.3. Plume Size Estimation

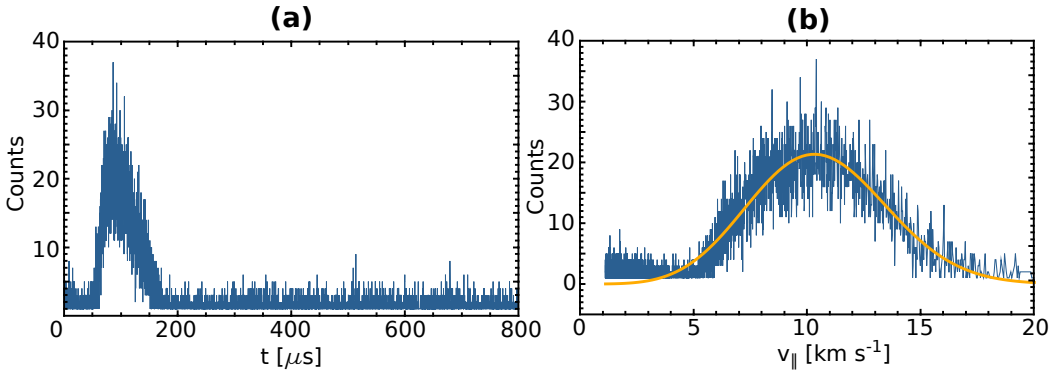

Figure A.4.: a ^{39}K-atom time signal measured with the QGA when ablating a $^{39}K^{35}Cl$ pressed powder ablation target.**b** Calculated velocity profile in blue together with a shifted Maxwell Boltzmann distribution fit. The distance d between the target and the QGA ionization region is $d \approx 0.9\,\mathrm{m}$ the atoms then have an velocity distribution peaking at around $v \approx 10000\,\mathrm{m\,s^{-1}}$. The fitted temperature is $T \approx 5.9 * 10^4\,\mathrm{K}$.

To give a reasonable starting condition for our simulation we first estimate the size of the ^{39}K plume injected into the buffer gas cell. We therefore took a measurement of the ablation itself to get a rough estimate on the temperature the ^{39}K has which is injected into the cell. Fig. A.4 shows the time signal of the ablated ^{39}K which is measured with our QGA. At time $t = 0\,\mu\mathrm{s}$ the ablation laser is fired. The ionization volume of the QGA is at $z_{\mathrm{qga}} = 0.9\,\mathrm{m}$ away from the ablation point. By assuming that the atomic pulse ejected from the target is short compared to the pulse width that we measured at z_{qga} away we can calculate the associated velocity distribution shown in Fig. A.4. In orange a fit is shown assuming a drifting Maxwell Boltzmann distribution for a flux measurement 6.8. Here T is the associated temperature of the pulse whereas w boosts the whole distribution to higher velocities. This boost is due to the hydrodynamic expansion of the high density ^{39}K plume near the target surface directly after the ablation. Through our fit we estimate $w \approx 6650\mathrm{m\,s^{-1}}$ and $T \approx 59000\,\mathrm{K}$.

We can use this knowledge to implement a toy model Monte Carlo simulation. We use a two dimensional model of hard disks and inject 100 molecules following the measured longitudinal velocity distribution and a transverse distribution only given by the temperature T and with no velocity boost. We then let each ^{39}K atom collide with a ^{4}He atom randomly chosen following a $4\,K$ Maxwell-Boltzmann distribution. The mean free path is calculated after each collision following formula 6.2 and the path of the ^{39}K atoms is tracked. Since each ^{4}He atom is chosen from a thermalized Maxwell Boltzmann distribution the simulation still has the simplification that the ablation does not alter the ^{4}He distribution. We stop the simulation for each ^{39}K atom if its velocity v_K is smaller than the average velocity of thermalized ^{39}K at 4 K.

Figure A.5 shows the two dimensional spatial distribution obtained from this simulation for our cell with $d_{\mathrm{ap}} = 3\,\mathrm{mm}$ and $\mathcal{F} = 10\,\mathrm{sccm}$. The distribution has an umbrella like shape and a size of approximately 10 mm in the y-direction and of about 5 mm in the x-direction. The whole distribution is shifted from the injection point in positive x-direction due to the boosted velocity in this direction from the ablation.

Summing up this toy model gives us an estimate of the size of the initial distribution of cold ^{39}K in our cell for the later simulation. Since the mean free path is proportional to ρ^{-1} we would expect that the size and distance from the ablation point of the initial thermalized distribution scales accordingly.

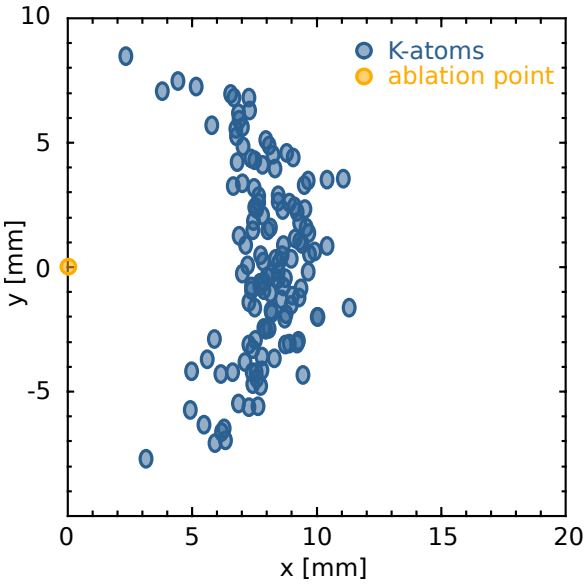

Figure A.5.: Simulated spatial distribution of ^{39}K atoms after thermalization when injected at the origin with the measured velocity distribution of A.4 into a thermalized cloud of ^{4}He at 4 K.

A.4. Picture of the Cell in the vacuum chamber

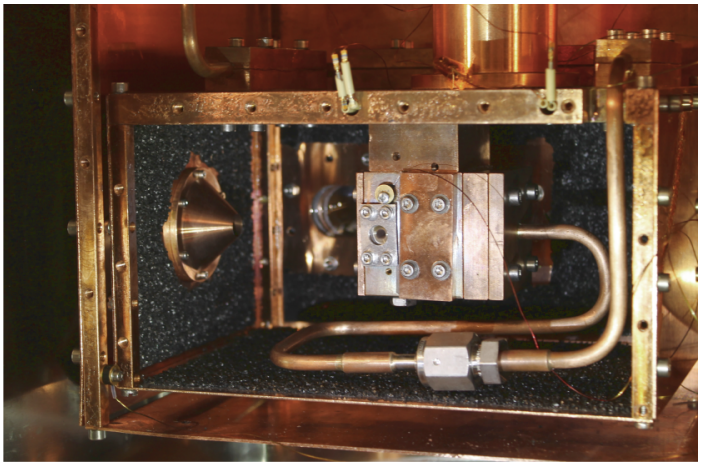

Figure A.6.: Picture of the cryogenic buffer gas beam source assembled in the vacuum chamber. Here the charcoal can be seen which acts as a cryopump for ^{4}He at temperatures $T < 10$ K.

Acknowledgements

Here I want to thank certain people who contributed either directly or indirectly to the work presented in this thesis. I hereby deeply apologize if I forgot someone. I try to keep it short.

First I want to thank Silke for the oppurtunity to write my thesis in her group and that she put that many trust into me. For being always there and that I always felt welcome when walking in her office. I also thank for the oppurtunities to visit international conferences and for putting the trust in me that I could present the work.

Second I want to thank my additional thesis surveyors Carsten Klempt and Boerge Hemmerling for reading this thesis and for being available at short notice.

I want to thank Mirco Siercke for explaining a lot of physics to me and that you put the faith back into me, that it is possible to understand this stuff. And for always having an ear for any kind of problem and a lot of other things.

Paul Kaebert for being a good labmate and always being available for anything reading a lot of the things i wrote and for listening to the stuff I always want to say. And for being someone who drinks beer.

Philipp Gersema for being a great master student and in a good mood while nothing worked as it should. Mariia for entering the group and for leading the experiments from success to success in the future. Timo for the interest, good questions and good work. Nicklas for not talking about elves, Androsch's children or other dragonslayer stuff. Thorben for building a lot of electronics.

I thank the basement for a lot of useful equipment. I thank Miss Hünitzsch for being patient and doing all the paperwork and explaining me a thousand times how I have to fill out certain papers. I thank the POMOS for a lot of things and here is not enough space to list them. Especially Matthias, Torsten, Kai and Torben from whom I learned a lot and who have always been there for questions. I thank Kai for reading and finding a lot of small little errors. I want to thank Alex for building all the things coming out of my head and turning them into reality.

I thank the RTG1729 for great lectures, a ton of good talks and the workshops. I thank the whole cold molecules community for being an open minded science community where new ideas are always welcome. From the first months of my official thesis I want to thank Mark Yeo, Matt Hummon, David Reens, Alejandra Collopy, Hao Wu and Jun Ye for a great time in Boulder where I learned a lot! My flatmates for a nice time in the flat. My family for being always there for me.

أود أن أشكر بشكل خَاص ليَالي للّوقت الذي أَمضينَاه معَاً للّدعم الذي قدمتيه و بَالأَخص الحمّص
الذي قدمتيه لي أَثنَاء كتَابتي لرسَالة الدكتورَا . أَحبك

I thank Yara and her parents for translating the sentence above into arabic.